PE&RS

March 2020 Volume 86, Number 3

PHOTOGRAMMETRIC ENGINEERING & REMOTE SENSING

The official journal for imaging and geospatial information science and technology

NOW AVAILABLE!

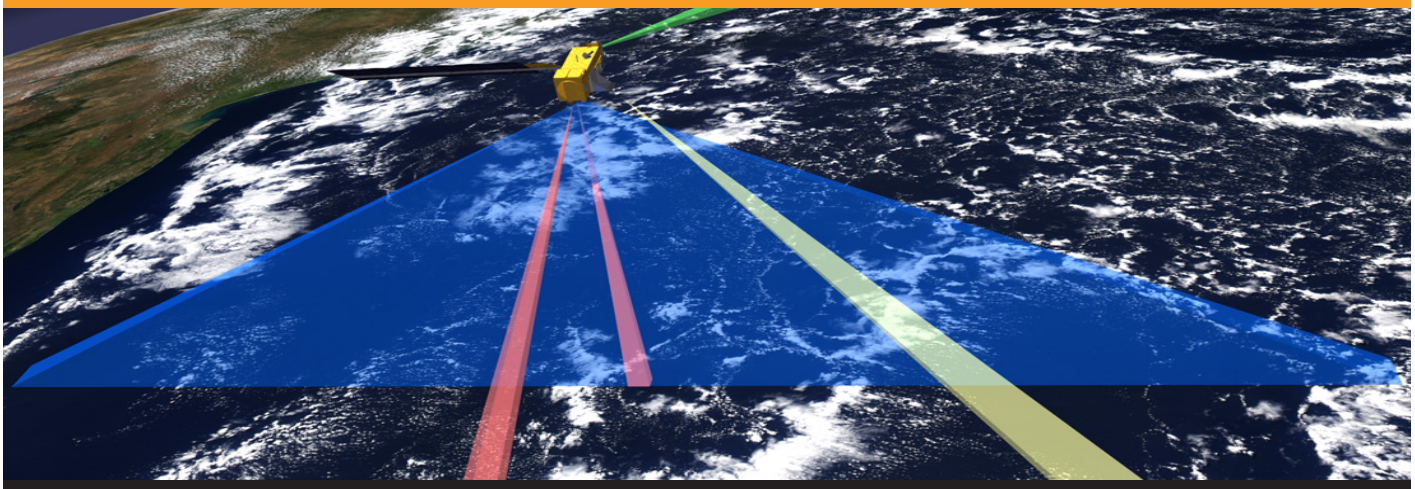

MANUAL OF REMOTE SENSING

Fourth Edition

ASPRS Announces the 4th Edition of the *Manual of Remote Sensing!*

The *Manual of Remote Sensing, 4th Ed.* (MRS-4) is an "enhanced" electronic publication available online from ASPRS. This edition expands its scope from previous editions, focusing on new and updated material since the turn of the 21st Century. Stanley Morain (Editor-in-Chief), and co-editors Michael Renslow and Amelia Budge have compiled material provided by numerous contributors who are experts in various aspects of remote sensing technologies, data preservation practices, data access mechanisms, data processing and modeling techniques, societal benefits, and legal aspects such as space policies and space law. These topics are organized into nine chapters. MRS4 is unique from previous editions in that it is a "living" document that can be updated easily in years to come as new technologies and practices evolve. It also is designed to include animated illustrations and videos to further enhance the reader's experience.

MRS-4 is available to ASPRS Members as a member benefit or can be purchased by non-members. To access MRS-4, visit https://my.asprs.org/mrs4.

edited by: Stanley A. Morain,
Michael S. Renslow and Amelia M. Budge

The goal of the Manual of Remote Sensing-4 was to create a more effective, affordable, and durable Manual, and to broaden its scope to include economic and societal benefits. Effective in the sense that MRS-4's content could be found online as an enhanced e-book; affordable in the sense that content could be retrieved by everyone on an annual subscription basis; and durable in the sense that it could be easily updated as a "living" manual through fresh, contributor-driven and vetted material as technologies advance. It does not reprise the extensive mathematical basis for remote sensing given in MRS-2, but instead focuses on system designs; data processing, storage, and retrieval; and on societal applications. A key feature of this concept is to facilitate timely updates of cutting edge or new developments from a wide spectrum of sophisticated contributors facile collectively with the technological, mathematical, and utilitarian aspects of Earth and space sciences.

Table of Contents

MRS-4 is available to ASPRS Members as a member benefit or can be purchased by non-members. To access MRS-4, visit https://my.asprs.org/mrs4.

INDUSTRYNEWS

To have your press release published in *PE&RS*, contact Rae Kelley, rkelley@asprs.org.

ANNOUNCECMENTS

Phase One Industrial, a world-leading provider of medium format metric cameras and imaging solutions for aerial applications, today announced that it has signed an agreement with AI-Survey GmbH, a developer of UAS survey package, services and tailor-made solutions. Together, these companies' products are opening up new opportunities in drone-based high-accuracy mapping and inspection markets.

Under this agreement, AI-Survey will support Phase One Industrial's iXM range of cameras in the UAV market for high-accuracy mapping and inspection. AI-Survey offers fast and efficient, simple and reliable UAS solutions tailored for geodesists with millimetre imaging results.

For more information about AI-Survey or Phase One Industrial, please go to: https://ai-survey.com/startseite-en and http://industrial.phaseone.com.

Operating out of their United States headquarters in Huntsville, Alabama, GeoCue Group will further promote RIEGL unmanned LiDAR innovations through the introduction of their True View® 615 and 620 LiDAR/imagery fusion systems, integrated with the newly introduced RIEGL miniVUX-2UAV miniaturized unmanned LiDAR scanner, an upgrade from the previously planned TrueView 610 with the miniVUX-1UAV with 100kHz pulse repetition rate (PRR) to 200 kHz.

This solution offers surveyors an innovative LiDAR and dual oblique mapping camera configuration integrated in a single lightweight payload for use on commercial drone platforms. True View allows for fast, easy automated generation of true 3D colorized point clouds, oblique imagery and orthophotos from a single flight.

RIEGL is extremely excited to announce our partnership with GeoCue, along with their recent purchase of multiple miniVUX-2UAV scanners, and we look forward to a rewarding and successful relationship!

PROJECTS

It's been over three decades since reactor Number 4 at the Chernobyl Nuclear Power Plant in the Ukraine melted down, leading to the world's worst civilian nuclear disaster in history. Now, a team of multidisciplinary researchers have used Routescene's UAV LiDAR technology to map radioactive hotspots in greater detail than ever before.

Professor Tom Scott, from the School of Physics at the University of Bristol, UK, led a group of researchers from the UK's National Centre for Nuclear Robotics (NCNR) to conduct surveys on multiple sites of interest within the Exclusion Zone which surrounds the damaged reactor. The surveyed sites included Buriakivka village, a settlement abandoned following contamination from the power plant accident, and the "Red Forest", a natural woodland area located the closest to the reactor, hence the most heavily contaminated.

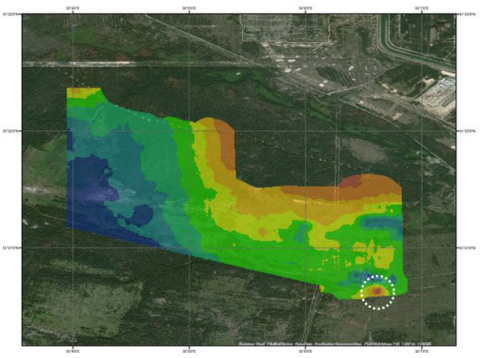

Working closely with local Ukrainian authorities, the team operated Unmanned Aerial Vehicles (UAVs) to perform a series of radiation mapping surveys. Routescene's lightweight LidarPod was flown on a DJI M600 hexacopter drone over the sites of interest. The point cloud data collected was processing using

Routescene's LidarViewer Pro software to generate a detailed Digital Terrain Model (DTM) and was overlaid with the results from a gamma spectrometer survey, undertaken to measure radiation intensity, to locate the exact sites of the radiation hotspots.

Routescene's LidarPod includes a carefully selected array of sensors delivering survey-grade high resolution results. Up to 1.4 million data points per second are collected from 32 different lasers angled in a 40-degree field of view. Crucially, the Routescene solution enabled the researchers to conduct operations and complete real-time QA monitoring at a safe distance from the radioactive sites, keeping them from harm.

For more information about the Routescene UAV LiDAR system including the LidarViewer Pro software andnew Bare Earth tool, please visit www.routescene.com

EVENT

Introductory Webinar: Using the UN Biodiversity Lab to Support National Conservation and Sustainable Development Goals:

- March 24, 2020: Introduction to Spatial Data and Policies for Biodiversity
- March 31, 2020: UN Biodiversity Lab: Introduction and Training
- April 7, 2020: How are Countries Using Spatial Data to Support Conservation of Nature?

Times:

- Session A (English): 9-10:30am ET
- Session B (French): 11am-12:30pm ET
- Session C (Spanish): 2-3:30pm ET

https://arset.gsfc.nasa.gov/land/webinars/un-biodiversity-2020.

continued on page 150

PE&RS
PHOTOGRAMMETRIC ENGINEERING & REMOTE SENSING
The official journal for imaging and geospatial information science and technology
March 2020 Volume 86 Number 3

FEATURES

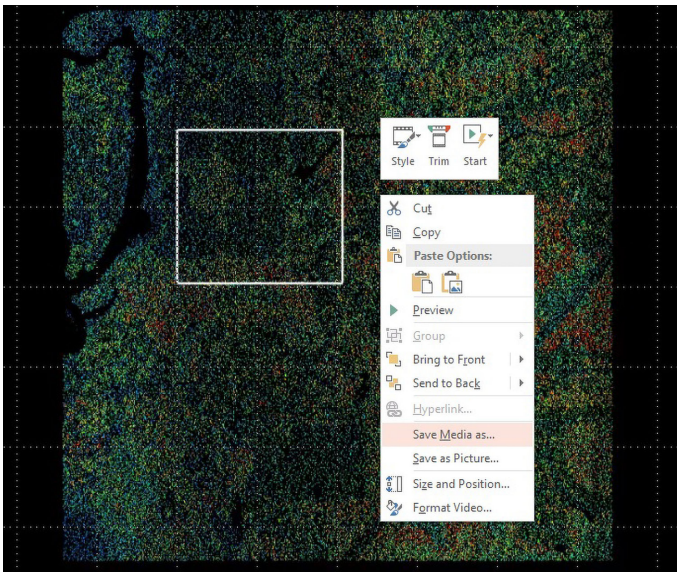

COLUMNS

ANNOUNCEMENTS

DEPARTMENTS

PEER-REVIEWED ARTICLES

See the Cover Description on Page 136

COVER DESCRIPTION

Fifty years ago, Cancún was virtually unknown to the world. With a population of roughly 100 people, the town was located in one of the poorest regions of Mexico. It had odd-shaped sand dunes and a coast occupied by marshes, mangroves, and a snake-infested jungle. Over the past five decades, though, Cancún has been transformed into one of Mexico's top tourist attractions. The growth didn't happen by chance.

In the late 1960s, the Mexican government took an interest in developing the country's tourism sector to boost the economy. To determine the perfect place, government officials analyzed statistics from several successful resort locations such as Miami Beach and Acapulco. They compiled information on the number of tourists, number of hotel rooms, average temperatures, average rainfall, and hurricane events and fed them into a computer program. The computer selected several candidates for a new resort town. Officials then visited each site along Mexico's approximately 10,000 kilometers (6,000 miles) of coastline to personally inspect the beaches, swimming, and living conditions.

In the end, they selected Cancún because it had good weather year-round, blue seas, and white sand beaches. It was also located near great archeological treasures, such as the Mayan ruins at Chichen Itza and Tulum. It also had a high level of poverty and no existing industry.

In January 1970, technicians arrived and began building the resort town. By September 1974, Cancún's first hotel opened its doors. Within a year, Cancún added more hotels and welcomed around 100,000 tourists. Today, Cancún accommodates around two million visitors annually and generates around one-fourth of the country's tourism revenue.

The image pair on the cover shows the growth of Cancún between March 28, 1985, and April 11, 2019. The images were acquired by the Thematic Mapper (TM) on Landsat 5 and the Operational Land Imager (OLI) on Landsat 8, respectively. In the late 1980s, Cancún's population registered around 120,000. A census report in 2015 conducted by the National Institute of Statistics and Geography (INEGI) reported around 740,000 people. Most of the hotels are located on a 27-kilometer (17-mile) stretch of beach known as the Hotel Zone.

While creating a large source of revenue, Cancún's tourism also has had major impacts on the environment. One of the biggest issues is water pollution due to sewage from hotels (about 95 percent of all sewage from the area)—significantly more than the local treatment plants can handle. Untreated sewage ends up in the sea and becomes a threat to aquatic ecosystems, sometimes introducing pathogens that affect coral growth. The resort has also significantly increased the amount of garbage produced, a share of which is sent to illegal garbage dumps. Hotel construction and human presence have also eroded beaches, threatening local reef and coral systems.

To view the full image, visit https://landsat.visibleearth.nasa.gov/view.php?id=146194.

NASA image by Allison Nussbaum, using Landsat data from the U.S. Geological Survey. Story by Kasha Patel.

asprs

THE IMAGING & GEOSPATIAL INFORMATION SOCIETY

PHOTOGRAMMETRIC ENGINEERING & REMOTE SENSING

JOURNAL STAFF

Publisher ASPRS
Editor-In-Chief Alper Yilmaz
Assistant Editor Jie Shan
Assistant Director — Publications Rae Kelley
Electronic Publications Manager/Graphic Artist
Matthew Austin

Photogrammetric Engineering & Remote Sensing is the official journal of the American Society for Photogrammetry and Remote Sensing. It is devoted to the exchange of ideas and information about the applications of photogrammetry, remote sensing, and geographic information systems. The technical activities of the Society are conducted through the following Technical Divisions: Geographic Information Systems, Photogrammetric Applications, Lidar, Primary Data Acquisition, Professional Practice, and Remote Sensing Applications. Additional information on the functioning of the Technical Divisions and the Society can be found in the Yearbook issue of *PE&RS*.

Correspondence relating to all business and editorial matters pertaining to this and other Society publications should be directed to the American Society for Photogrammetry and Remote Sensing, 425 Barlow Place, Suite 210, Bethesda, Maryland 20814-2144, including inquiries, memberships, subscriptions, changes in address, manuscripts for publication, advertising, back issues, and publications. The telephone number of the Society Headquarters is 301-493-0290; the fax number is 225-408-4422; web address is www.asprs.org.

PE&RS. *PE&RS* (ISSN0099-1112) is published monthly by the American Society for Photogrammetry and Remote Sensing, 425 Barlow Place, Suite 210, Bethesda, Maryland 20814-2144. Periodicals postage paid at Bethesda, Maryland and at additional mailing offices.

SUBSCRIPTION. For the 2020 subscription year, ASPRS is offering two options to our *PE&RS* subscribers — an e-Subscription and the print edition. E-subscribers can plus-up their subscriptions with printed copies for a small additional charge. Print and Electronic subscriptions are on a calendar-year basis that runs from January through December. We recommend that customers who choose both e-Subscription and print (e-Subscription + Print) renew on a calendar-year basis.

The rate of the e-Subscription (digital) Site License Only for USA and Non-USA is $1000.00 USD. e-Subscription (digital) Site License Only for Canada* is $1049.00 USD. e-Subscription (digital) Plus Print for USA is $1365.00 USD. e-Subscription (digital) Plus Print for Canada* is $1424.00 USD. e-Subscription (digital) Plus Print for Non-USA is $1395.00 USD. Printed-Subscription Only for USA is $1065.00 USD. Printed-Subscription Only for Canada* is $1124.00 USD. Printed-Subscription Only for Non-USA is $1195.00 USD. *Note: e-Subscription/Printed-Subscription Only/e-Subscription Plus Print for Canada include 5% of the total amount for Canada's Goods and Services Tax (GST #135123065). **PLEASE NOTE: All Subscription Agencies receive a 20.00 USD discount.**

POSTMASTER. Send address changes to *PE&RS*, ASPRS Headquarters, 425 Barlow Place, Suite 210, Bethesda, Maryland 20814-2144. CDN CPM #(40020812)

MEMBERSHIP. Membership is open to any person actively engaged in the practice of photogrammetry, photointerpretation, remote sensing and geographic information systems; or who by means of education or profession is interested in the application or development of these arts and sciences. Membership is for one year, with renewal based on the anniversary date of the month joined. Membership Dues include a 12-month electronic subscription to *PE&RS*. Or you can receive the print copy of *PE&RS* Journal which is available to all member types for an additional fee of $60.00 USD for shipping USA, $65.00 USD for Canada, or $75.00 USD for international shipping. Dues for ASPRS Members outside of the U.S. will now be the same as for members residing in the U.S. Annual dues for Regular members (Active Member) is $150.00 USD; for Student members $50.00 USD for USA and Canada $58.00 USD; $60.00 USD for Other Foreign members. A tax of 5% for Canada's Goods and Service Tax (GST #135123065) is applied to all members residing in Canada.

Speakers at Geo Week

Building a Geospatial Nervous System for the Planet

Jack Dangermond, Founder & President, *Esri*

Our world resembles a living organism. It's complex. It is interconnected as an ecosystem. It is self-healing and resilient, and always changing. As humans, we're fundamentally part of that ecosystem, and this evolution is at the same time rapidly changing our world. Today our human footprint is creating many challenges for all of us, as individuals and organizations, and the broader society. We're losing biodiversity at a rapid rate. We're facing challenges of water and food shortages, and unconstrained development, if we project it out, it is just not sustainable. These are our big challenges today. Our world needs something like our human nervous system, a kind of nervous system that's intelligent and responsive, that creates more understanding and collaboration; more systematic and collaborative action. And geography is essential to make that happen. Geography is the science of our world. It provides all the rich content; biological content, geologic content, sociological content, all the "ology's" content as well as a common reference system which is close to our human experience. It helps us see complexity in terms of relationships and patterns. And this science brings it all together in the most remarkable way. It helps us understand and respond intelligently. Your work is contributing, directly or indirectly, to a kind of global geospatial infrastructure, sharing apps, sharing your experience, sharing data, sharing your knowledge, linking your projects into infrastructure, using the infrastructure's resources and contributing to it, creating a system for understanding and collaborative action. It is creating a geospatial nervous system for the planet.

Combining Remote Sensing & Analytics Technologies: Emerging Environmental Applications

Tara O'Shea, *Planet*

The past decade has seen an explosion in the availability of remotely sensed data, due in part to technological advances that have reduced the size and increased the number of Earth observation satellites. Parallel advances in machine learning and cloud computing have also enabled more correlations between insights from these datasets. In this session, we'll hear from Tara O'Shea, Director of Forest Programs at Planet, about what this means for emerging environmental and climate applications. In particular, Tara will highlight applications that combine Planet's unique global dataset with lidar data to create breakthrough capabilities in monitoring forest carbon stocks and emissions, mapping wildfire risk, and more.

Combining Remote Sensing & Bringing Light (Detection and Ranging) into Shadow: The Role of Lidar in Exploring the Moon

Dr. Michael Zanetti, Planetary Scientist, *NASA*

With the Artemis program, NASA will land the first woman and next man on the Moon by 2024, and through collaboration with commercial and international partnerships will have sustainable lunar exploration by 2028 in preparation for future Mars missions. The target is the Moon's South Pole, an area of strategic importance that presents significant benefits and challenges, both related to persistent sun-light and shadows. In this presentation, Dr. Michael Zanetti, a lunar and planetary geologist will provide an introduction to the Artemis program, why the we are going the lunar South Pole, and the role for LiDAR in reconnaissance, landing hazard avoidance, and terrain navigation and mapping in aiding exploration of the Moon and Mars.

ASPRS Workshops

March 23, 2020

Streamlined Photorealistic Textured Mesh and True Orthophoto Generation from Aerial Imagery

Thomas Widmer, *Trimble* and Mohsen Miri, *Trimble*

Highly accurate 3D meshes provide virtual navigation of real-world environments in desktop and web platforms. These products are used in city modeling, construction and simulation purposes. Modeling of 3D surfaces with sharp edges and high quality textured meshes can be performed in a modern and precise methods. These meshes can be used to produce true orthophotos, simplifying planimetric mapping and the overlay of other GIS data, especially in urban mapping applications. This workshop will explore the methods used to create these products using Trimble INPHO MATCH-3DX software.

Digital Aerial Triangulation using Imagery from Multi-Head Systems

Mohsen Miri, *Trimble* and Thomas Widmer, *Trimble*

Current aerial mapping technologies lead to capturing a large number of images, not only at nadir but also in oblique viewing directions. The number and variety of multi-head oblique platforms available on the market is continuously growing. This workshop presents a stable and simplified workflow for the complex multi-head imagery for higher production efficiencies. This workshop will explore the workflow and the matching strategies for such systems using Trimble INPHO MATCH-AT software.

Best Practices for Managing, Editing, Visualizing, and Sharing Lidar in 2D and 3D

Nicholas Giner, *Esri* and Lindsay Weitz, *Esri*

Although lidar data has been collected and processed for over 20 years, the global lidar market continues to rapidly expand as demand for 3D imagery in consumer, commercial, and government applicatioincreases. Federal, state, and local government agencies are acquiring lidar data for use in applications such as floodplain mapping, urban planning and design, resource and environmental management, law enforcement, natural resource exploration, archeology, and emergency response. This session will teach best practices for working with Light Detection and Ranging (lidar) data . Attendees of this session will learn lidar basics and fundamentals, as well as the best practices for managing, editing, visualizing, and sharing it in 2D and 3D. Attendees will also learn several workflows for deriving useful information products from lidar data, as well as performing 2D and 3D analysis on lidar-derived products.

Using USGS/ASPRS Data Quality Measure (DM) Software for Validation of Airborne Lidar Point Clouds

Barry Miller, *USGS* and Ajit Sampath, *USGS*

This workshop provides an in-depth look at the USGS/ASPRS Data Quality Measure (DQM) software. DQM provides an ability to determine the relative accuracy, or geometric quality, of overlapping swaths of lidar point clouds using a point-to-plane measurement technique. DQM calculates vertical and horizontal differences between swaths in a point cloud tile, which allows better analysis of the quality of a lidar project. Attendees will see a demonstration on how to use the tool and interpret the results with several real-world examples. The workshop will also show how to obtain the software, which is a government-furnished freeware for public use.

UAS Lidar for Precision Mapping

Mohamed Mostafa, *Microdrones Canada Inc.*

Professional grade lidar systems are currently being used onboard unmanned aerial systems for high precision mapping applications. This workshop is intended for the unmanned airborne lidar user community including mapping professionals, land surveyors, managers, and decision makers to understand the underlying concepts of lidar from the technical and business perspective, in the form of theory and practice, using real data sets from around the world.

Fundamentals of Image Analysis in Google Earth Engine

Ge (Jeff) Pu, *SUNY-ESF*

Cloud-based image processing platforms like the Google Earth Engine (GEE) bring unprecedented possibilities for education, research, and outreach. This workshop will focus on an interactive exploration of GEE capabilities, the repository of all of publicly available aerial and satellite data, and user upload of imagery for analysis. The workshop will begin with a presentation of examples of GEE projects with a focus on education, undergraduate research, and outreach followed by hands-activities.

Preparation for ASPRS Certification – Lidar

Karen Schuckman, *Penn State University*

This workshop provides an in-depth review of content contained in the ASPRS Airborne Topographic Lidar Manual. It is valuable for those planning to take the examination for ASPRS Certified Mapping Scientist-Lidar, Certified Technologist-Lidar, or Intern. Workshop participants will answer practice questions and discuss answers in an interactive session. The workshop is also valuable for practitioners wishing to further their mastery of the theory and practice of topographic mapping with lidar.

REGISTER FOR WORKSHOPS ON THE CONFERENCE REGISTRATION SITE!

If you have already registered for the conference and wish to add a workshop, call 508-743-8501.

If you wish to register for a workshop without registering for the conference, call 508-743-8501.

For additional information, see http://conferences.asprs.org/geoweek-2020/ or contact programs@asprs.org

Practical Approach to Using the ASPRS Positional Accuracy Standards for Digital Geospatial Data

Qassim Abdullah, *Woolpert, Inc.* and
Claire Kiedrowski, *Cornerstone Energy Services, Inc.*

This workshop provides an in-depth look at the ASPRS Positional Accuracy Standards to categorize positional accuracy of products derived from digital aerial cameras, manned and unmanned aerial systems, and all types of lidar including terrestrial, mobile, and airborne. The workshop will explain the basis for each accuracy measure adopted in the standards. Instructors will demonstrate practical application of these standards. Attendees will apply these standards to real-world examples.

Based Image Analysis Made Easy and Flexible

Keith Peterson, *Trimble*, and
Jarlath O'Neil-Dunne, *University of Vermont*

This workshop will provide an informative introduction to the fundamental concepts and technologies in object-based image analysis and iats combination with computer vision methods, machine-learning and pixel-based operations. Attendees will use eCognition Developer to employ a comprehensive range of analysis tools utilizing diverse data sources, from medium to high resolution satellite data, very high- resolution aerial and UAV imagery, GIS, lidar, radar, and even hyperspectral data.

Combining Deep Learning with Object Based Image Analysis (OBIA)

Keith Peterson, *Trimble*, and Christian Weise, *Trimble*

Recently, deep learning (DL) has become the fastest growing trend in data analysis and has been widely and successfully applied to various feature extraction tasks. In the context of remote sensing the combination of DL with OBIA (object-based image analysis) offers the flexibility to select the optimal working method inside the complete feature extraction workflow. This workshop will explore the accelerated usage of deep learning with object-based image analysis using Trimble eCognition Developer software.

Spreadsheet Demonstration of Analytical Photogrammetry

Paul Pope, *Global Geoinformatics Inc.*

Photogrammetry is often explained by describing the collinearity condition and showing examples of final products. The intermediate steps are rarely illustrated in detail. This workshop aims to make analytical photogrammetry accessible to the layperson by using spreadsheet calculations to 1) solve for the exterior orientation parameters of a framing camera, and 2) determine the dimensions of an object using stereo imagery.

Generic Sensor Models for Photogrammetric Applications

Henry Theiss, *Integrity Applications Incorporated*

The workshop conveys the importance of rigorous sensor modeling, data adjustment, and covariance propagation in meeting the absolute geolocation, relative mensuration, and multi-sensor fusion objectives of the end-user. It proceeds with an overview of the Community Sensor Model (CSM) Application Programming Interface (API) which facilitates integration of multi-modality imagery and point-cloud products into geospatial exploitation tools. It provides an overview of generic sensor models for frame-sequences, linear-array scanners, SAR, and lidar."

Total Propagated Uncertainty (TPU) and Absolute Accuracy Assessment of 3D Lidar Point Cloud

Minsu Kim, *USGS*

Total Propagated Uncertainty (TPU) is the statistical estimate of lidar positional uncertainty for each lidar point. Theoretical details of the TPU and its application to the airborne lidar data will be presented. Assessment of the 3D absolute accuracy of the lidar point cloud is an important priority in USGS 3DEP program. TPU is an important factor that affects the absolute accuracy of the lidar point cloud data. Techniques for the 3D absolute accuracy assessment using various geometric features and its inherent relationship with TPU will be discussed in the workshop.

Machine and Deep Learning Image Classification

Amr Abd-Elrahman, *University of Florida*

This workshop teaches participants how to (1) conduct pixel- and object-based image classification using traditional (Support Vector Machine and Random Forests) machine learning algorithms; (2) build models for data preparation and experiment with different classification parameters; (3) use the deeplab deep learning architecture for image segmentation (classification). Participants will be briefly introduced to necessary theoretical background information as well as practical implementation using ArcGIS Pro. Real world examples of wetland land cover classification will be used in the demonstration.

Preparation for ASPRS Certification - General Knowledge

Robert Burtch, *Ferris State University*

This workshop covers the common knowledge areas comprising a large portion of exam content for ASPRS Certification. It is valuable preparation for those who have never taken an ASPRS exam, as well as for those who have expertise in a particular specialty, such as lidar or UAS, but feel less prepared for the general knowledge component of the exam. This workshop will also explain the certification application process and the importance of certification in career development.

Aerial Triangulation and Data Processing for the Unmanned Aerial System (UAS)

Qassim A Abdullah, *Woolpert, Inc.* and
Riadh Munjy, *CSU Fresno*

This workshop teaches participants to successfully design, plan and execute an aerial mission using unmanned aerial systems (UAS) and GPS-based aerial triangulation, including flight planning, ground control placement, camera calibration, and product generation. Participants will be introduced to mathematical basis of simultaneous bundle block adjustment. Practical examples will be presented.

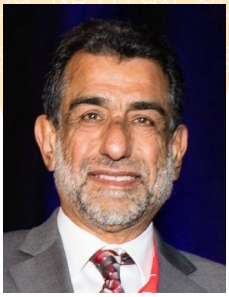

MAPPINGMATTERS

YOUR QUESTIONS ANSWERED

The layman's perspective on technical theory and practical applications of mapping and GIS

BY Qassim A. Abdullah, PH.D., PLS, CP**

QUESTION:

Question: Like everyone else around the world, we in St. Petersburg, Russia, are working with outdated manuals and standards for geospatial data production. There are tremendous difficulties in finding recommendations for acquiring and processing geospatial data when the only guidelines on photogrammetric processes in our country were published in 2002. It is extremely difficult to apply old specifications to products from today's digital sensors, especially when working with lidar and unmanned aircraft systems (UAS). I went on the internet looking for any appropriate documents on the subject and discovered the ASPRS Positional Accuracy Standards for Digital Geospatial Data of 2014. These are good standards for today's mapping operations. In the standards, I noticed there are requirements for the accuracy of aerial triangulation, number of checkpoints and examples of how to assess your data accuracy. However, most accuracy examples seem to be applicable to products from large- and medium-format metric cameras. Most of our operations today use UAS with a dual-frequency GNSS receiver and Sony RX1 camera. Unfortunately, this camera is not a metric camera. Thus, I have the following questions:

1. Can we use the ASPRS Accuracy Standards for Digital Geospatial Data in our practice? Are there official guidelines and standards for situations in which small-format, non-metric cameras and UAS are used?
2. I also found your presentation, "Understanding The new ASPRS Positional Accuracy Standards for Digital Geospatial Data,"[1] from a NOAA's National Geodetic Survey (NGS) event, The National Spatial Reference System (NSRS) Modernization Industry Workshop, on May 7-8, 2018. Slide 20 of the presentation lists 4cm as the highest affordable accuracy that one can achieve with UAS. What other conditions and practices should be observed to achieve this accuracy?
3. I also read your white paper that Woolpert published on "The New Standards of Map Accuracy."[2] In Table 3 on Page 5 of that white paper lists the "Horizontal Accuracy Standards for Digital Planimetric Data," in which you multiply map scale factor by 1.25%, 1.5% or 2% to calculate RMSEx and RMSEy (cm). I don't understand what this multiplier means. Is it something like the National Map Accuracy Standards (NMAS), where the horizontal accuracy standard requires that the positions of 90% of all points tested must be accurate within 1/50th of an inch (0.05cm) on the map? Is it something that describes how accurately a user can measure a line on the map with a ruler?

Natasha Akimova, Photogrammetrist, Geoscan Group, St. Petersburg, Russia

1 https://www.google.com/url?sa=t&rct=j&q=&esrc=s&source=web&cd=7&ved=2ahUKEwjQyYa97ZrhAhXa8qYKHTyDCr8QFjAGegQIBBAC&url=https%3A%2F%2Fwww.ngs.noaa.gov%2Fdatums%2Fnewdatums%2Findustry-workshop-presentations%2FASPRS_Accuracy_Standards.pptx&usg=AOvVaw3lIlKirs8s4q8FwU7Ex7GP.

2 https://woolpert.com/wp-content/uploads/2017/05/The-New-Standard-of-Map-Accuracy.pdf.

Dr. Abdullah: I am going to address your questions in the same order as your message.

1. Your observations on the new ASPRS Positional Accuracy Standards for Digital Geospatial Data are accurate. These are the only standards that exist today that are solely designed for today's geospatial sensors and technologies. These standards provide guidance on process control throughout the product-generation phases. They define the requirement for ground control accuracy, aerial triangulation accuracy and final product accuracy, and contain guidelines on checkpoints. While some examples are based on large-format metric cameras, the new standards are designed to be sensor agnostic and data driven. These standards are suitable for current and future technologies, no matter how accurate the products are. You can use it for satellite imagery-derived products, aerial sensors, UAS-based sensors, and mobile mapping lidar and terrestrial lidar sensors. You can use it to evaluate and express products from UAS the same way you use it for products from manned aircraft. The strength of the new

"While some examples are based on large-format metric cameras, the new standards are designed to be sensor agnostic and data driven. These standards are suitable for current and future technologies"

Photogrammetric Engineering & Remote Sensing
Vol. 86, No. 3, March 2020, pp. 141–144.
0099-1112/20/141–144

doi: 10.14358/PERS.86.3.141

standards is that they endorse unlimited accuracy classes. The accuracy class is not based on a preset accuracy number nor does it depend on imagery resolution, contour interval or a map scale, as all these terms are associated with the old generation of mapping practices. Take, for example, ortho accuracy produced from imagery acquired with 5cm resolution. This imagery can be produced with 5cm, 10cm or even 100cm accuracy, depending on how stringent the workflow used during the production process is or the number and quality of the ground control points. With today's various configurations of digital cameras and focal length, such imagery can be acquired from less than 100m (the case of UAS) or by using manned aircraft from an altitude of 1,000m or even higher using cameras with a longer focal length. That is the reason we designed the new standards to be sensor agnostic, focusing on the merit of the final products produced from the sensor. Users can order 5cm orthorectified imagery that has an accuracy of 5cm, if the application requires it and the user is willing to pay extra, or they can order that imagery with an accuracy of 15cm if that will satisfy the project requirements. That is exactly what the new standard is based on. Users or producers can label any level of product accuracy, regardless of the pixel resolution. That is why the new standards provide an unlimited number of accuracy classes. Such flexibility allows the use of metric and non-metric cameras, including the consumer-grade cameras flown on board a UAS. However, users and producers should understand the difference between the two types of camera classes, so they do not oversell products from non-metric cameras. The only complaint I receive from the UAS community about using the new standards for their UAS projects is the number of checkpoints required for accuracy evaluation. The standards call for a minimum of 25 checkpoints to verify the horizontal and vertical accuracy of a project area of no larger than 500 square kilometers. Projects flown by UAS are nowhere near 500 square kilometers, so having the requirement of 25 checkpoints is not practical nor affordable for these small projects. Although this complaint is valid, the ASPRS standards adopted this number to satisfy its statistical sampling theories. To perform a statistically valid test, you need the sample (represented by the areas around the checkpoints) to accurately represent population (represented by the map of the entire project test). Therefore, the larger the sample, the more accurate the test. The National Standard for Spatial Data Accuracy (NSSDA) published by the Federal Geographic Data Committee (FGDC) calls for a minimum of 20 checkpoints. Reducing the number of checkpoints to fewer than 20 or even fewer than 25 may result in skewed results that do not represent a random distribution of errors. Imagine that you are running a test using only 3 checkpoints and found that the errors in one of these 3 checkpoints vastly exceeded the accuracy tolerance expected from this test. These results would mean that 33% of the samples failed the test, and you would have no choice but to reject the tested data. But if you have 25 points, one outlier represents only 4% of the samples failed, which allows for better confidence in the data. My advice to members of the UAS community who are planning to evaluate the accuracy of UAS-derived products is to plan on having 20-25 checkpoints if the project budget allows for it. If not, then the fewer checkpoints available for the test is better than not performing any accuracy evaluation. However, I cannot advise you on using fewer checkpoints routinely, as this method does not yield a statistically valid sample.

"My advice to members of the UAS community who are planning to evaluate the accuracy of UAS-derived products is to plan on having 20-25 checkpoints if the project budget allows for it. If not, then the fewer checkpoints available for the test is better than not performing any accuracy evaluation"

2. As for the slide in my presentation, I am listing it here (Figure 1) for the benefit of the readers:

Can ASPRS Standards be used for UAS products?

Required accuracy for the products:
Ortho Accuracy: 4 cm (RMSEx or y)
DSM Accuracy: 4 cm (RMSEz)

ASPRS Standards Requires:
$RMSE_x$, $RMSE_y$ or $RMSE_z$ (ground control)= $^1/_4$ * $RMSE_{x(Map)}$, $RMSE_{y(Map)}$ or $RMSE_{z(DEM)}$

Ground Control for AT accuracy = 1 cm (RMSEx, y, z)
Check points for QC accuracy = 1.33 cm

Figure 1: UAS products and ASPRS standards.

In that slide, I tried to emphasize the false claims made by many UAS-operators-turned-mappers. Many in the UAS business claim that they are meeting sub-centimeter accuracy on a regular basis. Such a claim has no merit when you discuss it in the context of standard photogrammetric and surveying practices. Everyone knows that if you are testing a mapping product, the reference agent you use to produce the map, which are the ground control points—or, for accuracy evaluation, the checkpoints—need to be of higher fidelity than the produced or tested map. The

new ASPRS standards call for the ground control points used in the aerial triangulation process to be FOUR times more accurate than the generated products noted in the above slide. The standards also call for the checkpoints used to verify product accuracy to be three times more accurate than the tested map. Accordingly, when someone claims that the ortho-rectified mosaic produced from a UAS mission is accurate to 4cm (as RMSE), they need to realize that the ground control points used in processing the data need to be accurate to 1cm (as RMSE). While it's possible to survey ground control points with accuracy of 1cm using traditional surveying techniques, it is not possible to produce this accuracy from RTK surveying practices that are commonly used for surveying ground control points for mapping. Besides not meeting the ground control point accuracy used in the production process, their claim of product accuracy should be based on independent testing using independent checkpoints that are three times more accurate than the tested products and that were not used in the aerial triangulation process. Many of these producers base their accuracy conclusions on the fit of the ground control points in the aerial triangulation process. Again, basing the product accuracy on the aerial triangulation results is not correct because the ground controls used in the processing do not equate to independent checkpoints. It is well known that RTK-based field surveying techniques, which are used to support the majority of mapping projects, result in no better than 2cm accuracy. Therefore, according to the new ASPRS standards, such RTK-based survey can only be used to produce products that are no more accurate than 8cm (or 0.26 feet) or to verify the accuracy of mapping products that are no more accurate than 6cm (or 0.20 feet). That is the reason I question any claim that a UAS-derived product is more accurate than 8cm, unless traditional surveying techniques and differential leveling practices were used to survey the ground control points. Data providers need to educate themselves on photogrammetry and surveying best practices if they want to join the geospatial mapping community. This education can be pursued through participation in the training program that ASPRS offers at its annual conference or through pursuing an ASPRS certification.

"according to the new ASPRS standards, such RTK-based survey can only be used to produce products that are no more accurate than 8cm (or 0.26 feet) or to verify the accuracy of mapping products that are no more accurate than 6cm (or 0.20 feet)"

3. As for the white paper, the accuracy thresholds were based on an earlier version of the ASPRS standards before the final version of the standards were published in 2014. The drafting of the standards lasted three years during which we, the drafting committee, considered different approaches for accuracy classes. The white paper represents the period when the drafting committee considered adopting the same approach as the previous version of the legacy ASPRS standards of 1990, in which there are three accuracy classes: I, II and III. Later in the drafting process, the committee realized that limiting the accuracy to three classes that are fixed to certain accuracy numbers is the wrong approach, since mapping technologies are evolving rapidly, and future technologies may enable us to obtain accuracies that far exceed the thresholds we have today. In addition, we wanted the new standards to be sensor agnostic to apply to all mapping technologies, including the most accurate terrestrial and mobile lidar systems. As for your question on the approach followed in the white paper by assigning 1.25%, 1.5% or 2.0% scale factor, I do not encourage anyone to follow this approach anymore because the drafting committee has since abandoned the use of map scale, contour interval, pixel size, etc., as an accuracy measure. Scale was created to help the mapping process at a time when the only way to produce a map was on paper. This is also true of the use of the old concept of contours and contours interval. I hope users will embrace the new standards and get used to the idea of assigning an accuracy class to the data that suits their needs regardless of the imagery resolution or lidar data quality. We need to start expressing the accuracy for orthorectified imagery as a 15cm or 5cm accuracy class, regardless of the image resolution from which it was produced. This approach is already used by the industry when dealing with lidar data. Of course, best practices should be followed by the data producers and end users when contracting projects. Both should agree on reasonable acquisition parameters of imagery or lidar and the production process to assure that 5cm, 10cm or any other accuracy classes are achievable.

"I question any claim that a UAS-derived product is more accurate than 8cm, unless traditional surveying techniques and differential leveling practices were used to survey the ground control points"

However, although I do not recommend using this approach, I also would like to answer your question on the formulas I used in the white paper as I know some agencies are still using map scale and associated accuracy figures. If you look at Table 1 (also Table 1 in the white paper), which lists the horizontal accuracy classes for orthophoto, you notice that we were going to use Class I with the accuracy of 1 pixel of the orthophoto, Class II with 1.5 pixel

accuracy, and Class III with 2.0 pixel accuracy.

Table 1 Horizontal accuracy classes for ortho imagery.

Horizontal Data Accuracy Class	RMSEx and RMSEy	Orthophoto Mosaic Seamline Maximum Mismatch
I	Pixel size x 1.0	Pixel size x 2.0
II	Pixel size x 1.5	Pixel size x 3.0
III	Pixel size x 2.0	Pixel size x 4.0

To apply these accuracy classes to planimetric paper maps with certain scales, I followed our common practice of associating the 15cm imagery to produce 1:1,200-scale map. Then I used the accuracy figures from Table 1 for 15cm orthophoto, which is 15cm to derive the following relationship to associate the map scale with the map accuracy:

Accuracy (cm) = (15cm/1,200) x 100 x 1,200 = 1.25% x Map Scale Factor = 0.0125 x Map Scale Factor.

I hope I addressed all your questions and concerns.

***Dr. Abdullah is Chief Scientist and Senior Associate at Woolpert, Inc. He is also adjunct professor at Penn State and the University of Maryland Baltimore County. Dr. Abdullah is ASPRS fellow and the recipient of the ASPRS Life Time Achievement Award and the Fairchild Photogrammetric Award.*

GEOSPATIAL REVOLUTION

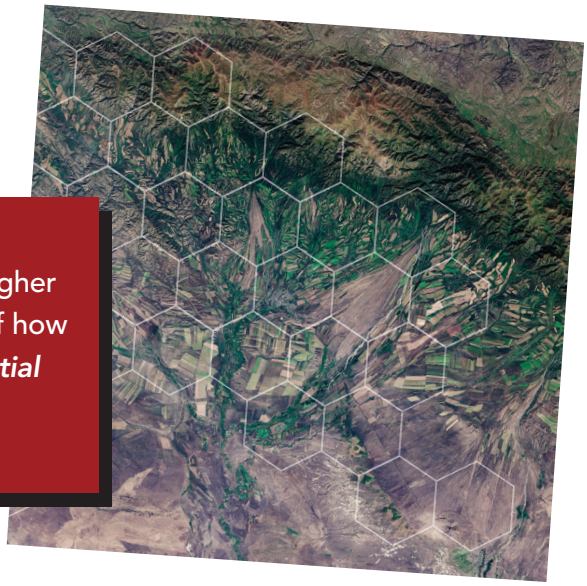

With more than 1 million video views, the ***Geospatial Revolution Project*** is the go-to source for government, higher education, and workforce development for an overview of how geospatial technology is changing the world. The ***Geospatial Revolution Project*** is anchored in a world-class research university and trusted for its PBS editorial standards.

THE NEXT GENERATION

WPSU Penn State is celebrating the 10th Anniversary (2010-2020) of the launch of the original *Geospatial Revolution Project* with a new video episode about next-generation innovations in geospatial technology.

Our Emmy Award-winning production team explores stories from public safety, business, and national defense. The real revolution in geospatial technologies is just beginning!

AUDIENCES & DISTRIBUTION

The new episode—with ready-made *Geospatial Revolution* audiences in government, public safety, industry, education, and the general public—will be screened at conferences, posted to social media, linked to the original project website, and shared with original engagement partners:

- U.S. government *(e.g., U.S. DOD, NGA, FBI, U.S. Army Corps of Engineers)*
- Higher education/workforce development collaborators
- K-12 STEM education

CONTACT

Please make a philanthropic gift to WPSU Penn State to support the new episode. *For more information, contact:*

Elaine Brzycki
Project Development
WPSU Penn State
ejb23@psu.edu

Kristian Berg
Director, Geospatial Revolution Project
WPSU Penn State
kjb35@psu.edu

Dr. Todd S. Bacastow
Teaching Professor
Dept. of Geography • Penn State
tsb4@psu.edu

Karen Schuckman
Associate Teaching Professor
Dept. of Geography • Penn State
kls505@psu.edu

"*Geospatial Revolution* is considered the 'Bible' of the GIS field. I can't wait to see the next episode!"

– Dr. Salvatore Amaduzzi
University of Udine, Italy

WPSU PENN STATE

GEOSPATIAL REVOLUTION
geospatialrevolution.psu.edu

GIS Tips & Tricks

By Al Karlin, Ph.D, CMS-L, GISP and Thomas Lundman

Hidden Talents in your Software?

Most everyone, these days, is familiar with the MicroSoft™ Office (or Office 365™) Suite of software products. We know that we use Word™ for our word processing needs and we fashion our spreadsheets, graphs and tables with Excel™. Databases to Access™ and our e-mails go to Outlook™. Of course, everyone knows that we make our presentation slide decks with PowerPoint™. However, some of these familiar programs have hidden talents. For example, did you know that you could record your screen for demonstrations or training videos using PowerPoint™?

Here are the steps to make a screen recording using PowerPoint™:

1. Open a new PowerPoint™ presentation file, and click on the "Insert" Tab. On the extreme right-hand side of the ribbon in the "Media" group is the "Screen Recording" Icon

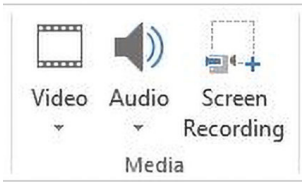

2. Clicking on the "Screen Recording" Icon will activate the PowerPoint Video and Audio (you can record sound also) Control Bar. Note: You can pin the Control Bar to your screen using the pushpin in the lower right corner, or the Control Bar will collapse into the top of your screen (default) as you record. To recover the Control Bar, just mouse to the top of the screen

3. Use the "Select Area" Icon on the Control Bar and drag a box on the screen for the area you want to capture. You can capture a portion of a screen or drag the area across your entire desktop. Select the "Record Pointer" option to include the cursor in your video. Press the "Record" icon to start the recording and proceed to record your screen and speak into your microphone to record your voice. Note: You will have a three second warning countdown for when recording will begin. HINT: You might want to practice your screen movements (and audio) a few times before actually capturing anything.

4. During recording the "Record" icon will be replaced by a "Pause" Icon. To stop the recording, mouse to the top of the screen to expose the Control Bar, and press the "Pause" Button

> ***"...did you know that you could record your screen for demonstrations or training videos using PowerPoint™?"***

5. To finish the recording and insert the video/audio into your slide, close the Control Bar using the "X" in the upper left-corner or use the Keyboard shortcut; Windows+-Shift+Q. This will insert your recording onto your blank slide with the standard player controls beneath the slide:

Photogrammetric Engineering & Remote Sensing
Vol. 86, No. 3, March 2020, pp. 147–148.
0099-1112/20/147–148

doi: 10.14358/PERS.86.3.147

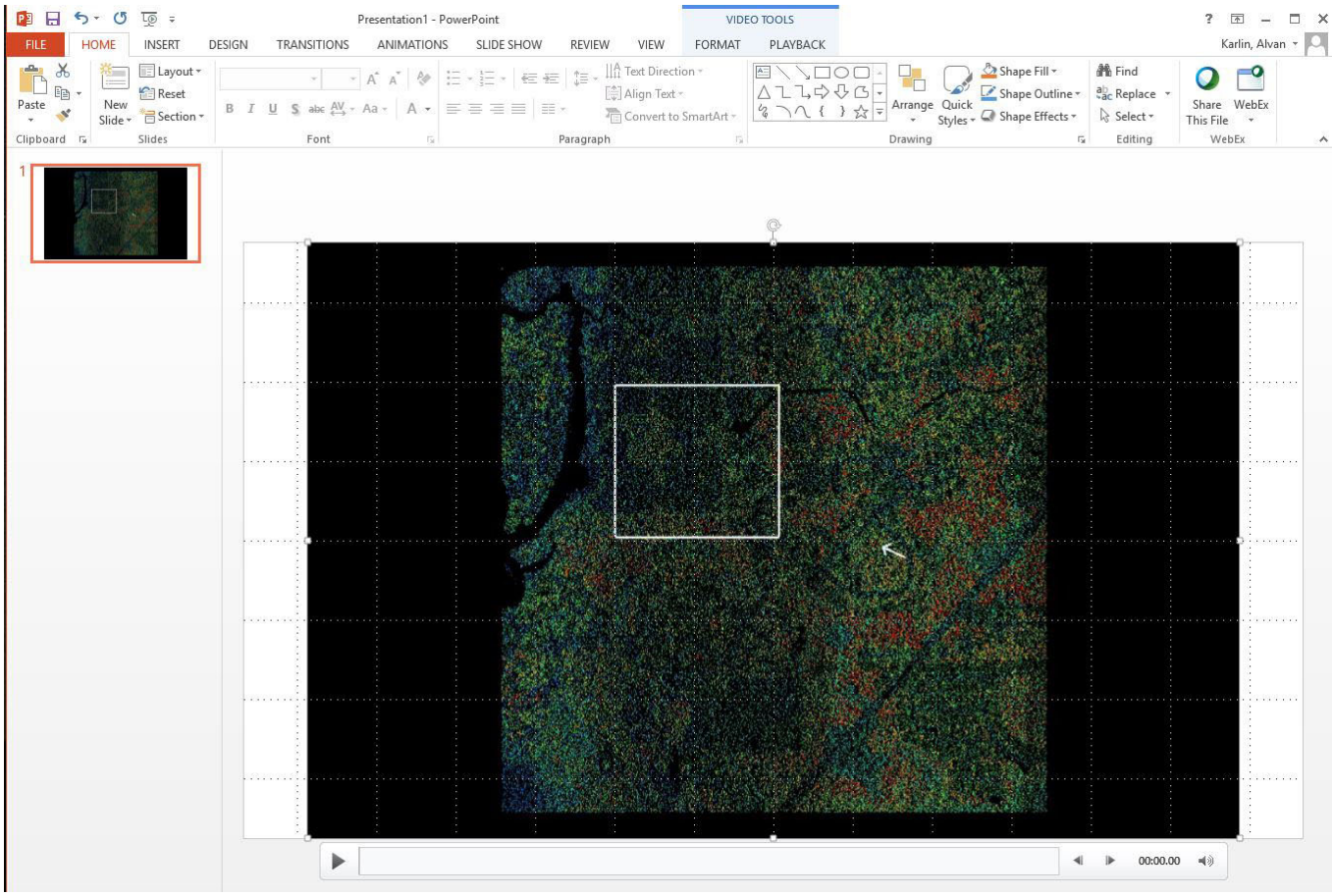

6. Finally, if you want to output the video/audio file to an .MP4 file, just right-click on the slide and select "Save Media as…"; navigate to a directory, name the file and it will save as an .MP4 medial file.

That is all there is to it. Happy recording using this hidden talent in PowerPoint™.

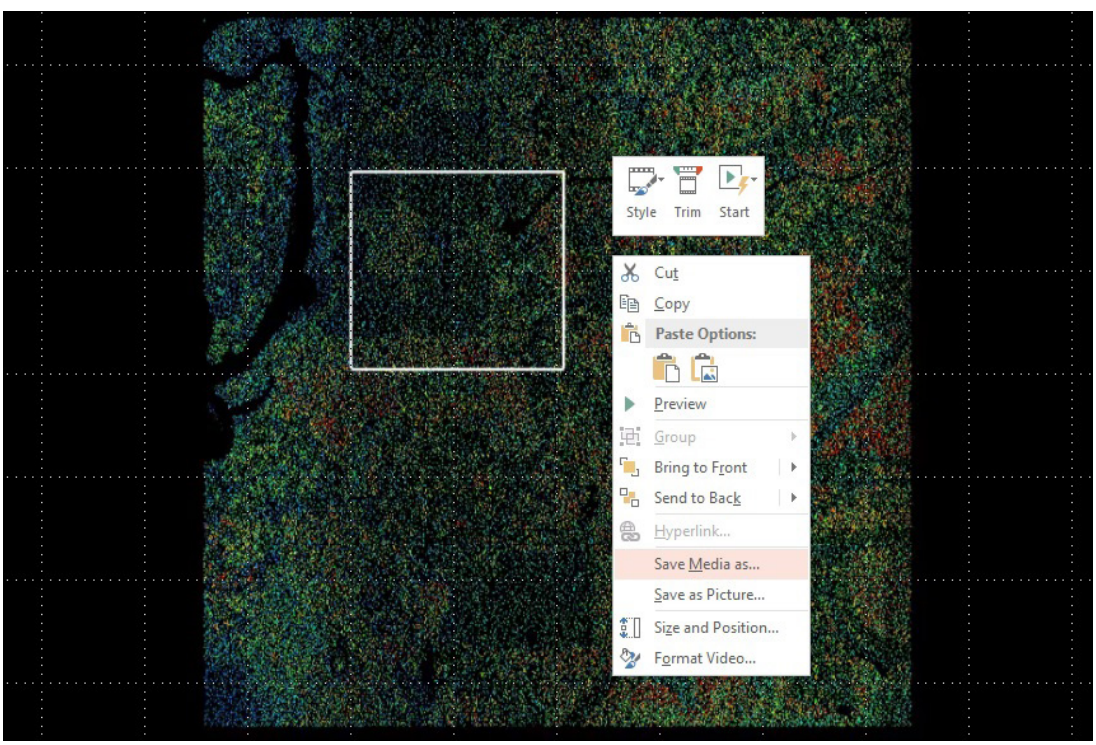

Al Karlin, Ph.D., CMS-L, GISP *and* ***Thomas Lundman*** *are with Dewberry's Geospatial and Technology Services group in Tampa, FL and Fairfax VA. As a Senior GIS Professional, Al works with all aspects of Lidar, remote sensing, photogrammetry, and GIS-related projects. Thomas is a GIS Analyst who works on Lidar and Remote Sensing projects and enjoys picking through processes to find ways to improve them.*

NEW ASPRS MEMBERS

ASPRS would like to welcome the following new members!

Alaska
Ryan Patrick Marlow, CMS

At Large
Ayad Ahmed
A F M Fakhrul Azam
David A. Brown, RPP, CP.
Maurizio .. Buonanno
Prof. Yuhong He
Dr. Serkan Ural

Cascadia
Catherine Green
Ben Meister
Michael Puma
Lauchlan Ray
Dan Trifone

Eastern Great Lakes
Xiaohu Lu
Deborah Sheeler
Michael Evan Vega
Yuan Yang
Parth Bhatt
Shengxi Gui
Dr. Sami Khanal
Bryan Sluis

Florida
Amr Abd-Elrahman
Blake B. Biggs
John Burditt
Tevin Cruz
David Dagostino
Christopher James Griesbach
Ryan Ligon
Mary Elizabeth Voor
Dr. Benjamin Everett Wilkinson

Mid South
Johnny Flores
Dr. Unal Okyay
Jordan Lee Thomas
Destiny Denise Crockett
Greg Jackson
Dr. Fang Qiu
Kelsi Lyn Schwind
Clay D. Smith, CP
Hermogenes David Suarez
Dr. Bandana Kar, Ph.D.
Dr. Dorel Marius Necsoiu, CMS
Alberto Maala Pai
Kutalmis Saylam

North Atlantic
Steven Becker

Northeastern
Daniel Grosche

Pacific Southwest
Yubin Li
Huijie Zhang
Eric Albanese
Adam Downing
Paul Fridley
Dr. Maggi Kelly
Hubiao Lan, CP
Osbaldo Ortiz

Potomac
Megan Averso
Amy Avery Holz
Matthew Kyle Bainbridge
Michael Baranowski
Bryan Francis Behan
Dustin D. Brace
Evan H. Brown, CP, CMS
Charlene Curtis
Saurabh Shankarrao Dhamankar
Benjamin Downey
William P. Foley
Karen L. Jones
Michael Paquette, GISP
George Douglas SIX
Brian K. Tennant
Michael Van Arsdale
Andrew Robert Welti

Rocky Mountain
Dorcas Oluwabimpe Idowu
Marc Miller
Kevin Sacca
Mathew Guy White

FOR MORE INFORMATION ON ASPRS MEMBERSHIP, VISIT

HTTP://WWW.ASPRS.ORG/JOIN-NOW

Your Path To Success In The Geospatial Community

continued on from 134

ACCOMPLISHMENTS

URISA is pleased to announce the newest members of its Vanguard Cabinet. The Vanguard Cabinet (VC) is a URISA initiative (which debuted in 2011) to engage young GIS practitioners, increase their numbers in the organization, and better understand the concerns facing these future leaders of the GIS community. The VC is an advisory board who represent the young membership of the organization. The Cabinet's mission is to collaborate with URISA's Board of Directors and Committees in creating and promoting programs and policies of benefit to young professionals.

Comprised entirely of passionate young members selected from different geospatial disciplines, the Cabinet aims to position URISA as the center of opportunities for ambitious young professionals who are committed to improving URISA and the geospatial profession via innovation, collaboration, networking, and professional development. Each will serve a three-year term.

2020 URISA Vanguard Cabinet Members:

- Josiah Burkett, GIS Analyst, *GeoTechVision Enterprises Limited*, Kingston, Jamaica
- Shenyue Jia, Research Fellow, *Chapman University*, Orange, California
- Rachel Layko, Dangermond Fellow at the N*ational Audubon Society* and Fellow in the *Center for Geospatial Analysis*, *The College of William & Mary Center for Geospatial Analysis*, Williamsburg, Virginia
- Harraz Mohd Reza, GIS Technician, *Governor's Office of Information Technology, State of Colorado*, Denver, Colorado
- Frank Romo, Public Safety GIS IV, *City of Detroit* & CEO at *RomoGIS Enterprises*, Detroit, Michigan
- Dru Sexton, GIS Specialist, *Buckeye Hills Regional Council*, Marietta, Ohio
- Shradha Shrestha, Graduate Research Assistant in NSF INFEWS project, *Rochester Institute of Technology*, New York
- Caitlin Thomas, Geospatial Emergency Management Specialist, *Federal Emergency Management Agency* (*FEMA*), Atlanta, Georgia
- Shivon Van Allen, GIS Technician III, *NW Natural*, Portland, Oregon
- Megan Young, Research Data Specialist II, *California Public Utilities Commission*, San Francisco, California

In addition, Vanguard Cabinet members selected Haley J. Zehentbauer, GIS Analyst, Stark County, Canton, Ohio to serve as VC Chair and Meredith DiMattina, Crime Analyst Supervisor, City of Burlington, North Carolina, to serve as VC Secretary for 2020.

Cabinet members are selected through an application process, with a review by the Vanguard Steering Committee. The application process for 2021 Vanguard Cabinet members will open in October 2020. Learn more about VC activities here: https://www.urisa.org/vanguardcabinet .

CALL FOR NOMINATIONS

URISA's GIS Hall of Fame honors persons and organizations that have made significant and original contributions to the development and application of GIS concepts, tools, or resources, or to the GIS profession.

URISA is inviting nominations for 2020 inductees. Anyone may nominate a person or organization for induction to URISA's GIS Hall of Fame. To make a nomination, submit a written statement to URISA describing:

1. The nominee's achievements, emphasizing significant and original contributions to the development or application of GIS concepts, tools, or resources, or to the GIS profession; and
2. The significance of the nominee's contributions, in terms of their enduring impact on the GIS field or profession, and their social benefit.

Hall of Fame laureates are expected to exemplify vision, leadership, perseverance, community-mindedness, professional involvement, and ethical behavior.

Nominations are due on or before May 11, 2020. The 2020 URISA GIS Hall of Fame celebration will take place during GIS-Pro 2020 in Baltimore, Maryland.

For details about the nominations criteria and process, and to review the path-breaking accomplishments of previous inductees, visit https://www.urisa.org/awards/urisa-gis-hall-of-fame/.

CALENDAR

- 16-18 March, **RSCy2020**, Paphos, Cyprus. For more information, visit: www.cyprusremotesensing.com/rscy2020/
- 23-25 March, **Geo Week**, Washington, DC. For more information, visit https://www.lidarmap.org/geoweek/.
- 7-9 May, **GISTAM 2020—6th International Conference on Geographical Information Systems Theory, Applications and Management**, Prague, Czech Republic. For more information, visit: www.gistam.org/.
- 18-20 May, **UAV STRATUS**, Buffalo, New York. For more information, visit http://stratus-conference.com/home.
- 20-22 May, **AutoCarto 2020**, Redlands, California. For more information, visit https://cartogis.org/autocarto/.
- 15-22 August, **43rd COSPAR Scientific Assembly**, Sydney, Australia. For more information, visit www.cospar-assembly.org/.

SUSTAININGMEMBERS

ACI USA Inc.
Weston, Florida
acicorporation.com
Member Since: 1/2018

Aerial Services, Inc.
Cedar Falls, Iowa
www.AerialServicesInc.com
Member Since: 5/2001

Bohannan Huston, Inc.
Albuquerque, New Mexico
www.bhinc.com
Member Since: 11/1992

Cardinal Systems, LLC
Flagler Beach, Florida
www.cardinalsystems.net
Member Since: 1/2001

Dewberry
Fairfax, Virginia
www.dewberry.com
Member Since: 1/1985

Environmental Research Incorporated
Linden, Virginia
www.eri.us.com
Member Since: 8/2008

Extensis
Seattle, Washington
www.extensis.com
Member Since: 1/1997

GeoBC
Victoria, Canada
www.geobc.gov.bc.ca
Member Since: 12/2008

GeoCue Group
Madison, Alabama
info@geocue.com
Member Since: 10/2003

Geojano
Pleasanton, California
https://geojango.com/
Member Since: 05/2019

Geomni, Inc.
Lehi, Utah
Geomni.net/psm
Member Since: 03/2018

GeoWing Mapping, Inc.
Richmond, California
www.geowingmapping.com
Member Since: 12/2016

Global Science & Technology, Inc.
Greenbelt, Maryland
www.gst.com
Member Since: 10/2010

GPI Geospatial Inc.
formerly Aerial Cartographics of America, Inc. (ACA)
Orlando, Florida
www.aca-net.com
Member Since: 10/1994

Green Grid Inc.
San Ramon, California
www.greengridinc.com
Member Since: 1/2020

Keystone Aerial Surveys, Inc.
Philadelphia, Pennsylvania
www.keystoneaerialsurveys.com
Member Since: 1/1985

Kucera International
Willoughby, Ohio
www.kucerainternational.com
Member Since: 1/1992

L3Harris Corporation
Broomfield, Colorado
www.harris.com
Member Since: 6/2008

Martinez Geospatial, Inc. (MTZ)
Eagan, Minnesota
www.mtzgeo.com
Member Since: 1/1979

Merrick & Company
Greenwood Village, Colorado
www.merrick.com/gis
Member Since: 4/1995

Pickett and Associates, Inc.
Bartow, Florida
www.pickettusa.com
Member Since: 4/2007

PixElement
Columbus, Ohio
www.pixelement.com
Member Since: 1/2017

Quantum Spatial, Inc.
Sheboygan Falls, Wisconsin
www.quantumspatial.com
Member Since 1/1974

Robinson Aerial Survey, Inc. (RAS)
Hackettstown, New Jersey
www.robinsonaerial.com
Member Since: 1/1954

Routescene, Inc.
Durango, Colorado
www.routescene.com/
Member Since: 12/2007

Sanborn Map Company
Colorado Springs, Colorado
www.sanborn.com
Member Since: 10/1984

Towill, Inc.
San Francisco, California
www.towill.com
Member Since: 1/1952

Trimble
Munich, Germany
www.trimble.com/geospatial
Member Since: 4/19942

U.S. Geological Survey
Reston, Virginia
www.usgs.gov
Member Since: 4/2002

Woolpert LLP
Dayton, Ohio
www.woolpert.com
Member Since: 1/1985

PE&RS Special Issue

Call for Submissions

Optical Polarization Remote Sensing & Photogrammetry

Photogrammetric Engineering and Remote Sensing (*PE&RS*) is seeking submissions for special issue on optical polarization remote sensing.

Light is an electromagnetic wave vector and its wave equation of scalar propagation has four basic parameters: amplitude, frequency, phase and polarization. The polarization signal is usually ignored, and the remaining three parameters provide the physical basis of the four major resolutions (radiometric, spectral, spatial and temporal) of optical remote sensing. Nevertheless, polarization, which refers to the asymmetry of the light vibration, provides key information for studying the properties of materials.

More than 30 years of work has resulted in a science of polarization remote sensing (PolRS). PolRS includes the underlying physical theories, measurement instruments, including precision detection technology, and analytical approaches for studying polarization in imagery. The general conclusion of this research is that including the polarization signal in optical remote sensing images (such as hyperspectral or infrared images) can increase the contrast ratio by 2–3 orders of magnitude for mapping snow and ice, water quality, environmental pollution, rock density and roughness, oil spills, vegetation biomass, air pollution particle detection and atmospheric attenuation applications. Thus, PolRS offers a unique detection capability.

This special issue seeks papers on all aspects of optical polarization remote sensing science and technology, including theory, technology and applications.

How to Submit your Manuscript

All submissions will be peer reviewed according to the Photogrammetric Engineering and Remote Sensing (*PE&RS*) guidelines. Submitted manuscripts should not have been published or be under review elsewhere.

Prospective authors should consult the *PE&RS* Instructions for Authors on the journal homepage for guidelines and information on paper formatting and submission.

Authors should submit manuscripts using the *PE&RS* manuscript central system at https://www.editorialmanager.com/asprs-pers/default.aspx. Please choose '*PE&RS* Special Issue Paper' from the 'Manuscript Type' picklist on the submission form, irrespective of the paper type (i.e. even if your paper would normally be classified as a Research Letter, Tech Note, Research Paper, or Review Article). Also, please enter "Polarization" in the space provided on the submission form for the name of the special issue.

Important Dates

Deadline for the submission of contributions: **May 31, 2020**
Expected print publication date: **Late 2020**
Articles will be available online after acceptance, final technical review and the completion of revisions for compliance with journal format. However, the paper copy of the special issue will be published only when all papers are accepted.

If you have any specific questions about the special issue, please contact the editorial team listed below.

Editorial Team

Editor:

- Lei Yan, Peking University, China, lyan@pku.edu.cn
- Jouni Peltoniemi, Finnish Geospatial Research Institute (FGI) Finland, jouni.peltoniemi@nls.fi

Associate Editor:

- Bin Yang, Hunan University, China, binyang@hnu.edu.cn

Edge-Reinforced Convolutional Neural Network for Road Detection in Very-High-Resolution Remote Sensing Imagery

Xiaoyan Lu, Yanfei Zhong, Zhuo Zheng, Ji Zhao, and Liangpei Zhang

Abstract

Road detection in very-high-resolution remote sensing imagery is a hot research topic. However, the high resolution results in highly complex data distributions, which lead to much noise for road detection—for example, shadows and occlusions caused by disturbance on the roadside make it difficult to accurately recognize road. In this article, a novel edge-reinforced convolutional neural network, combined with multiscale feature extraction and edge reinforcement, is proposed to alleviate this problem. First, multiscale feature extraction is used in the center part of the proposed network to extract multiscale context information. Then edge reinforcement, applying a simplified U-Net to learn additional edge information, is used to restore the road information. The two operations can be used with different convolutional neural networks. Finally, two public road data sets are adopted to verify the effectiveness of the proposed approach, with experimental results demonstrating its superiority.

Introduction

With the launch of high-resolution remote sensing satellites—*Ikonos*, *QuickBird*, the WorldView satellites, etc.—we can now obtain abundant very-high-resolution (VHR) remote sensing imagery in a quick and economical way. VHR remote sensing imagery contains more detailed spatial information than low-resolution images, and provides us with massive data resources for ground-object detection (Lei, Wang and Lai 2009; Qulin 2010; Ammour *et al.* 2017). Ground-object detection aims to classify the image into buildings, roads, trees, and water (Kluckner *et al.* 2009; Ammour *et al.* 2017), or binary classification for a single object (Mnih and Hinton 2010). Road detection, known as a fundamental but challenging task in the VHR remote sensing field, has a wide range of applications, including urban planning (Soulard, Acevedo and Stehman 2018), unmanned-vehicle navigation (Hoareau *et al.* 2018), and geographic information systems updating (Mena 2003)c. As a result, scholars have carried out much related research. However, the high resolution brings the problem of a sharp increase in data volume and data complexity, so road detection in VHR remote sensing imagery is greatly affected by occlusions and shadows. Thus, automatic road detection with high precision is a difficult that needs much more research.

Road detection involves producing pixel-level labeling of road surfaces. Researchers have developed many methods for road detection, which can be divided into two main categories: traditional methods (Zhu *et al.* 2004; Saalmüller *et al.* 2009; G. Cheng *et al.* 2014) and those based on deep learning (Wang *et al.* 2015; Maggiori *et al.* 2017; Buslaev *et al.* 2018). Traditional methods require manually designed features according to the characteristics of the road properties. For example, Shi, Miao, and Debayle (2014) incorporated spectral-spatial classification and shape features into the road-detection process. However, this method cannot effectively extract complex circular intersections, and it is necessary to train the support vector machine classifier for each input image. Lv and Wei (2009) used the Hough transform to detect roads from the images, according to the linear topological characteristics of the roads, but this method is not suitable for curved roads. G. Cheng *et al.* (2016) utilized textural and geometric features to obtain a road centerline network. Although this method performs well on rural and suburban roads, performance decreases on urban road images. Accordingly, traditional methods generally require expertise to manually design the geometric, textural, and other visual features of the road, which are then sent to the classifier for classification. Although traditional road-detection methods can achieve relatively good performance, the problems are obvious. Feature extraction and classification are two separate processes, and involving humans in the process of feature design hinders automatic detection.

With the development of deep learning and specialized hardware such as graphics processing units (GPUs), automatically learning features from large-scale remote sensing images has become a reality. Deep-learning-based methods possess a powerful feature-expression ability due to their capacity for unsupervised feature learning. In the field of image analysis, convolutional neural networks (CNNs) are the most commonly applied approach, because of their shared-weights architecture. CNNs were inspired by biological processes (Matsugu *et al.* 2003) and were first successfully applied in document recognition (LeCun *et al.* 1998); they subsequently achieved a performance leap in the 2012 ImageNet Large Scale Visual Recognition Challenge (Krizhevsky, Sutskever and Hinton 2012). For road detection, a patch-based CNN was introduced by Mnih (2013) to recognize the center pixels of the patch. However, such an operation has limitations in computational

Xiaoyan Lu and Zhuo Zheng are with the State Key Laboratory of Information Engineering in Surveying, Mapping, and Remote Sensing, Wuhan University, Wuhan 430079, China.

Yanfei Zhong and Liangpei Zhang are with the State Key Laboratory of Information Engineering in Surveying, Mapping, and Remote Sensing, Wuhan University, Wuhan 430079, China; and the Hubei Provincial Engineering Research Center of Natural Resources Remote Sensing Monitoring, Wuhan University, Wuhan 430079, China (zhongyanfei@whu.edu.cn).

Ji Zhao is with the School of Computer Science, China University of Geosciences, Wuhan 430074, China.

Photogrammetric Engineering & Remote Sensing
Vol. 86, No. 3, March 2020, pp. 153–160.
0099-1112/20/153–160

doi: 10.14358/PERS.86.3.153

efficiency, due to the overlapping patches and the fully connected layer. Subsequently, fully convolutional networks) were proposed (Long, Shelhamer and Darrell 2015), using a CNN as a powerful feature extractor and replacing the fully connected layer with a convolutional layer. Fully convolutional networks can take an input image of any size and generate an output of the corresponding size. Buslaev *et al.* (2018) used a fully convolutional network in the DeepGlobe-CVPR 2018 road-extraction challenge; however, the extraction result was not fine enough, and some details were lost during the forward inference process. U-Net (Ronneberger, Fischer and Brox 2015) was subsequently designed to effectively preserve spatial details in the medical imaging field, by combining low-level feature maps with higher-level ones. U-Net has since become the basic deep-learning framework in pixel-level labeling.

In recent years, deep learning has made many breakthroughs, and effective modules have been developed to promote faster and better learning. Many previous studies have suggested that a shallow network has limited feature-expression ability and does not perform well in complex backgrounds. However, it is difficult to train a very deep network due to the vanishing-gradient problem. He (2016) proposed the deep residual network (ResNet) to ease training of the network via identity connections. Such additional shortcut paths can help the network achieve faster convergence. Since a neural network needs to be not only accurate but also efficient, Chaurasia and Culurciello (2017) developed LinkNet as an efficient neural network, which takes advantage of skip connections, residual blocks, and encoder-decoder architecture.

Even though deep learning provides many solutions for ground-object detection, the problem of road detection in VHR remote sensing images is far from being solved, due to the ubiquitous interference caused by disturbances around the road, which makes it difficult to accurately label road areas near the edge. In order to mitigate the blurring of edges in the semantic segmentation task, Cheng *et al.* (2017) designed a multitask model and used the outputs of the edge network to refine the entire model, which helps obtain spatially consistent results. Liu *et al.* (2018) developed an edge-loss reinforced network to retain the spatial edge information, which involves multiple weighted edge supervisions. Marmanis *et al.* (2018) introduced an end-to-end network with built-in awareness of semantically meaningful edges. In this article, inspired by these methods, the relationship between road area and road edge is established. Additional edge supervision is integrated into the deep network, which takes a simplified U-Net to learn the edge information from the road-detection results and the low-level finer details of different scales.

Through analysis of the problems discussed so far, an edge-reinforced convolutional neural network (ERMS-CNN) for road detection in VHR remote sensing imagery is proposed. It takes two semantic segmentation networks as the basic road-detection network—ResUNet34 and LinkNet34, which use multiscale feature extraction in the center part to obtain robust multiscale context information—then cascade a simplified U-Net to learn the edge information. ResUNet34 and LinkNet34 adopt ResNet34 as the encoder part, and the decoder part concatenates the low-level feature maps with the corresponding high-level ones to restore the spatial information. The main contributions of this article are summed up as follows:

- A powerful ERMS-CNN for road detection is proposed, which can be embedded in different road-detection networks. Considering that shallow networks have limited feature-expression ability, ResNet34 is applied as the encoder part to train a deeper network and more effectively carry out feature learning. Furthermore, the U-shaped architecture is adopted as the decoder part to restore spatial information because of its ability to obtain finer details.
- Multiscale (MS) feature extraction is used to obtain more robust features. Because of the interference of nonroad objects in VHR remote sensing images and the influence of complex road conditions, it is difficult to obtain robust features from feature extraction at a single scale. Thus, parallel atrous convolutions of different atrous rates, extracting MS contextual information, are applied to capture more robust features.
- Edge reinforcement (ER) is applied to help recognize the road. The high resolution brings much noise for road detection, such as the shadows and occlusions caused by disturbance, which makes the road difficult to recognize. To alleviate this problem, additional edge supervision is used, applying a simplified U-Net to learn edge information from the road-detection result and the low-level finer details of different scales.

In order to compare the proposed ERMS-CNN with other advanced road-detection methods, extensive experiments were conducted on two public road data sets: the Cheng data set and the SpaceNet data set. The proposed ERMS-CNN achieved satisfactory performance.

The rest of this article is arranged as follows. The next section describes the related architectures. The proposed ERMS-CNN for road detection is introduced in the section after that. Then come the experimental settings, followed by the experimental results and analysis. Finally, a summary is given of the conclusions and future research.

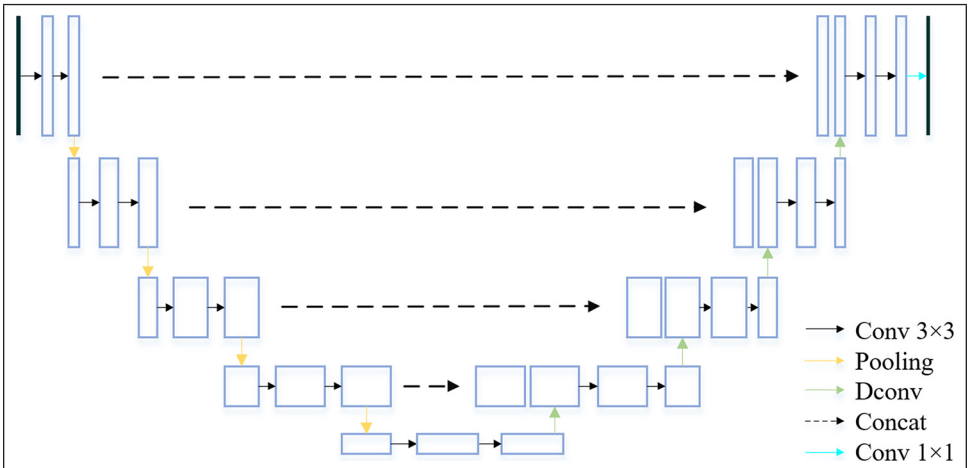

Figure 1. The simplified U-Net architecture.

Related Architectures

U-Net

U-Net (Ronneberger *et al.* 2015) is among the most popular approaches for semantic segmentation tasks, and was first proposed for biomedical image segmentation. Figure 1 shows a U-Net architecture, which includes a contracting path to extract contextual information and a symmetrically expanding path that concatenates the corresponding low-level feature maps. Such a structure can obtain finer pixel-level labeling.

ResNet

ResNet (He *et al.* 2016) was proposed to address the vanishing-gradient problem in training a deep network. Being a powerful feature extractor, ResNet contains several residual blocks, and each block consists of several layers. In each residual unit, ResNet performs identity mapping through shortcut connections, as Figure 2 displays. It can be illustrated by

$$y_l = h(x_l) + F(x_l, W_l) \quad (1)$$

$$x_{l+1} = f(y_l), \quad (2)$$

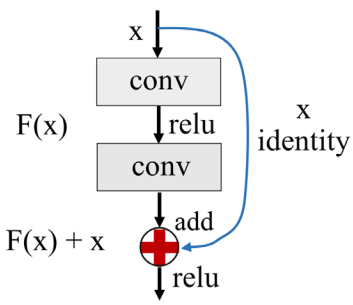

Figure 2. The structures of residual units.

where x_l and y_l are the input and output of the lth residual unit, each residual unit is followed by an activation function, $F(\cdot)$ and $f(\cdot)$ are respectively the residual function and activation function, and $h(\cdot)$ is the identity-mapping function.

The Proposed ERMS-CNN

Figure 3 displays the overall flowchart of the proposed ERMS-CNN for automatic road detection, which consists of three main parts: the powerful road-detection network built on ResNet and U-Net is introduced to achieve efficient road detection; parallel atrous convolutions are used in the center part to extract MS features; and edge reinforcement is applied to better recognize road. The details of the three main parts are provided next.

The Powerful Road-Detection Network

ResNet is a powerful feature extractor, and U-Net has a strong ability to retain spatial details. Therefore, the powerful ERMS-CNN combines the respective advantages of ResNet and U-Net for road detection in VHR remote sensing imagery. At the same time, the ResNet parameters pretrained on ImageNet (Krizhevsky *et al.* 2012) are used and then fine-tuned on the road data set, which is an efficient way to prevent overfitting and obtain fast convergence. The structure of the ERMS-CNN is displayed in Figure 4. In the contracting path, the four residual blocks are designed to extract the features. Before entering into the first residual block, the input images are reduced in size through 7 × 7 convolution (stride = 2) and 3 × 3 max pooling (stride = 2) operations. Meanwhile, there are convolutions (stride = 2) in the last three residual blocks to down-sample the feature maps. Through the last residual block, the output stride is 32. In the expanding path of ResUNet, deconvolution is used to up-sample, the feature maps are concatenated with the corresponding high-level ones after the first three residual blocks, and the number of channels is reduced through 1 × 1 convolution before each concatenation.

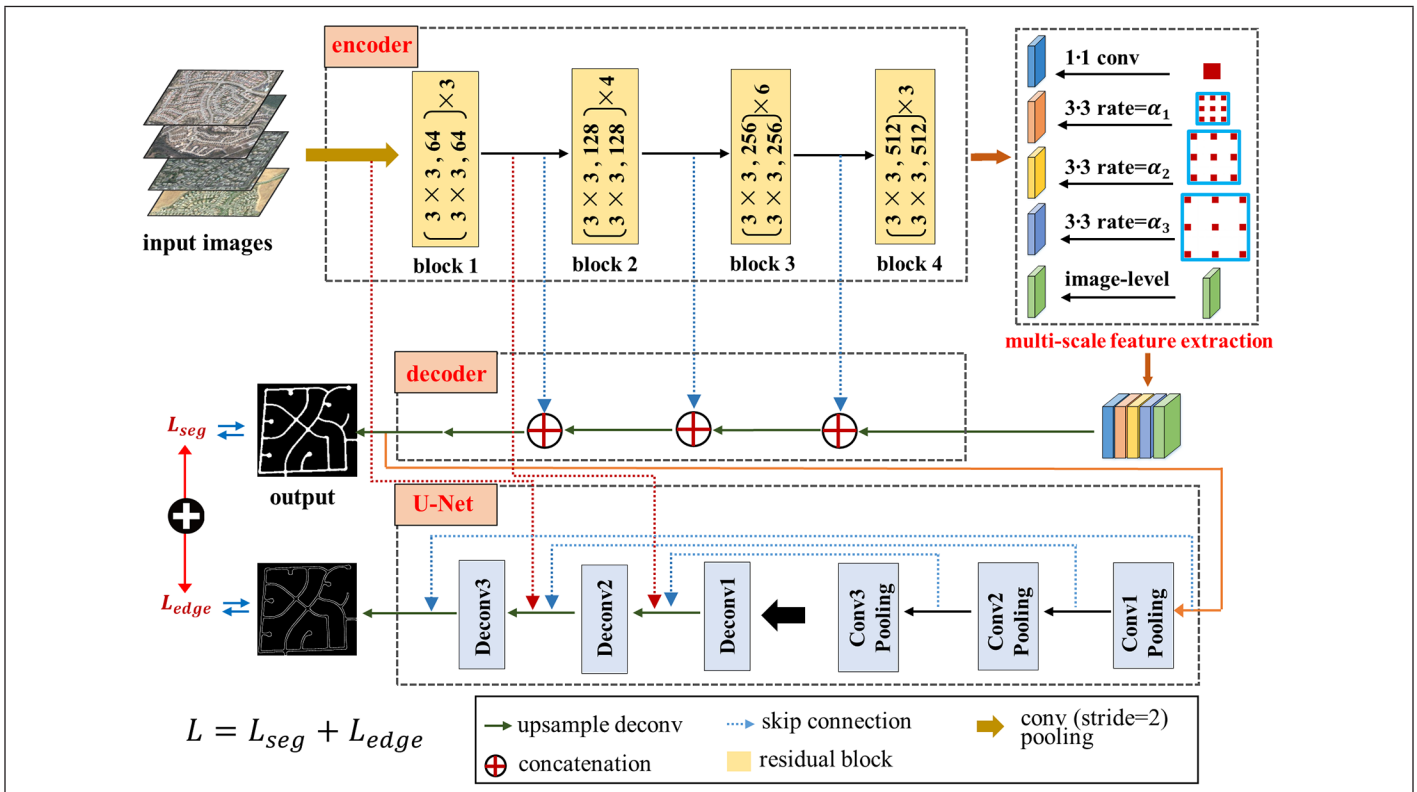

Figure 3. The overall flowchart of the proposed edge-reinforced convolutional neural network for road detection.

Particularly for the decoder block of LinkNet, as Figure 4 shows, 1 × 1 convolution is first adopted to reduce the feature dimensions to 1/4, followed by deconvolution (stride = 2) to upsample, then, 1 × 1 convolution is applied to obtain the output feature maps. Such operations can greatly reduce the computational parameters. After the decoder, the feature maps are restored to the original size of the input image, and the sigmoid classifier is then used to obtain the final probability map.

MS Feature Extraction

MS feature extraction is applied to capture the MS context information, as Figure 5 shows. Such an operation is completed through convolutions of different atrous rates to extract more robust features for road detection. Figure 5 illustrates the difference between the standard and atrous convolutions. The atrous convolution samples the input signal every few inputs for convolution. When the kernel size = 3 × 3 and the atrous rate = 2, the size of the output is 5 × 5, which can effectively enlarge the receptive fields without increasing the number of parameters. In this article, the input sizes of the two data sets are respectively 512 × 512 and 1024 × 1024, and we obtain 16*16 and 32*32 feature maps in the center part of the network, respectively. Therefore, different atrous rates for the two data sets are applied: 1, 2, 4, and 8 for the Cheng data set and 1, 6, 12, and 18 for the SpaceNet data set. MS features are then combined with the original image-level features.

Edge Reinforcement

All the models in this article are trained with the Adam optimizer and adopt the sum of the binary cross-entropy (BCE) and Dice-coefficient loss (DCL) as the loss function. DCL measures the amount of agreement between the predicted results and the ground truth, and has been widely applied in high-class-imbalance segmentation tasks. The loss function is described as follows:

$$L_{\mathrm{BCE}}(P,G) = -\sum_{i=1}^{W}\sum_{j=1}^{H}\left[g_{ij}\cdot \log p_{ij} + \left(1-g_{ij}\right)\cdot \log\left(1-p_{ij}\right)\right] \quad (3)$$

$$L_{\mathrm{DCL}}(P,G) = 1 - \frac{\sum_{i=1}^{N}\left|P_i \cap G_i\right|}{\sum_{i=1}^{N}\left(\left|P_i\right| + \left|G_i\right|\right)} \quad (4)$$

$$\mathrm{Loss} = L_{BCE}(P,G) + L_{DCL}(P,G), \quad (5)$$

where P and G are, respectively, the predicted results and the ground truth; W and H are the width and height; p_{ij} is the probability of being a positive sample; g_{ij} is the label; and N is the batch size. We set N to 4 in our experiments.

To better recognize the road, edge reinforcement is proposed to enhance edge supervision through a simplified U-Net learning road-edge information from the road-detection results and the low-level finer details of different scales. As Figure 3 shows, the simplified U-Net has three down-samples, and the feature maps of the simplified U-Net are 8, 16, 32, and 64, respectively. Meanwhile, the feature maps after the first convolutional layer and the first residual block are concatenated to the simplified U-Net to provide some low-level finer details for the road-edge information learning. Finally, we obtain the probability map through the sigmoid classifier, and we set the threshold to 0.5 to obtain the edge-learning results. By calculating the difference between the edge-learning results and the labels, we obtain the edge loss, namely L_{edge}.

In order to enhance the edge supervision information, we add the edge loss to the total loss:

$$L = L_{\mathrm{seg}} + L_{\mathrm{edge}}. \quad (6)$$

Experimental Settings

Data Sets

The first road data set was built by Cheng *et al.* (2017) and collected from Google Earth. The Cheng data set contains 224 VHR images, for which the ground truth includes both segmentation maps and centerline maps. We used only the segmentation maps, and built edge maps ourselves. The data set was randomly divided into 180 images for training, 30 for test, and 14 for validation. The resolution is 1 m^2/pixel, and the size of each image is at least 600 × 600 pixels. Examples from the data set are shown in Figure 6.

The second road data set was the SpaceNet road data set (Van Etten, Lindenbaum and Bacastow 2018), which contains 2780 images and centerline maps. The size of each image is 1300 × 1300, and the resolution is 0.3 m^2/pixel. Following Singh *et al.* (2018), we used the Euclidean distance transform to generate road heat maps along road centerlines and obtain binary road masks with a threshold of 0.76; and based on this, we built the edge maps. The data set was divided into 2000 training images, 520 test images, and 260 valid images. Examples from the data set are shown in Figure 7.

Evaluation Metrics

In order to quantitatively evaluate the performance of different methods in road detection, three common metrics are used: precision (P), recall (R), and quality (Q). P and R are the proportion of matched positive pixels in, respectively, the predicted results and the true pixels. Q is an overall metric, which is calculated from P and R. The metrics are calculated by the true positives (TP), false positives (FP), and false negatives (FN):

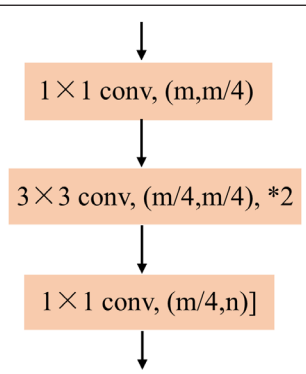

Figure 4. The decoder block in LinkNet.

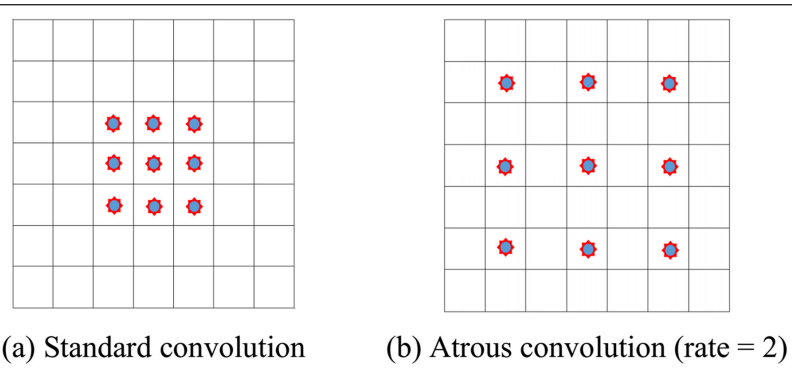

Figure 5. Illustration of standard and atrous convolutions.

$$P = \frac{\mathrm{TP}}{\mathrm{TP} + \mathrm{FP}} \tag{7}$$

$$R = \frac{\mathrm{TP}}{\mathrm{TP} + \mathrm{FN}} \tag{8}$$

$$Q = \frac{\mathrm{P} * \mathrm{R}}{\mathrm{P} - \mathrm{P} * \mathrm{R} + \mathrm{R}}. \tag{9}$$

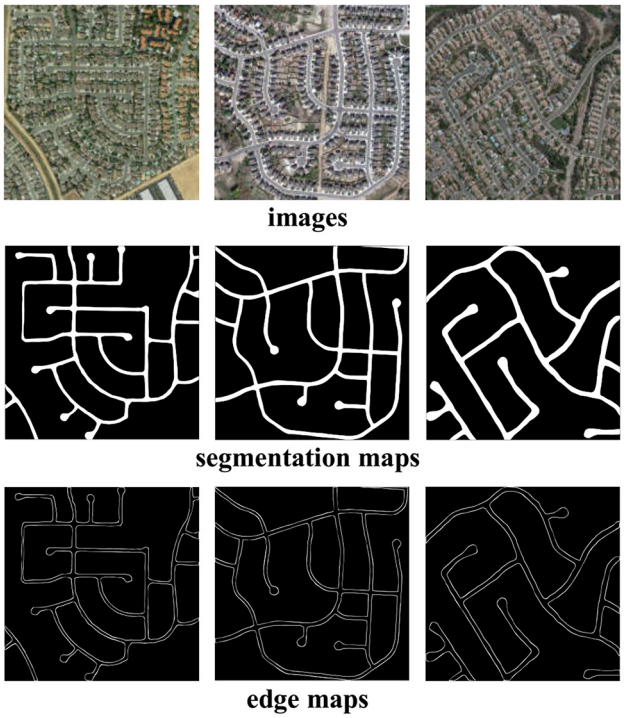

Figure 6. Images and maps of the Cheng data set.

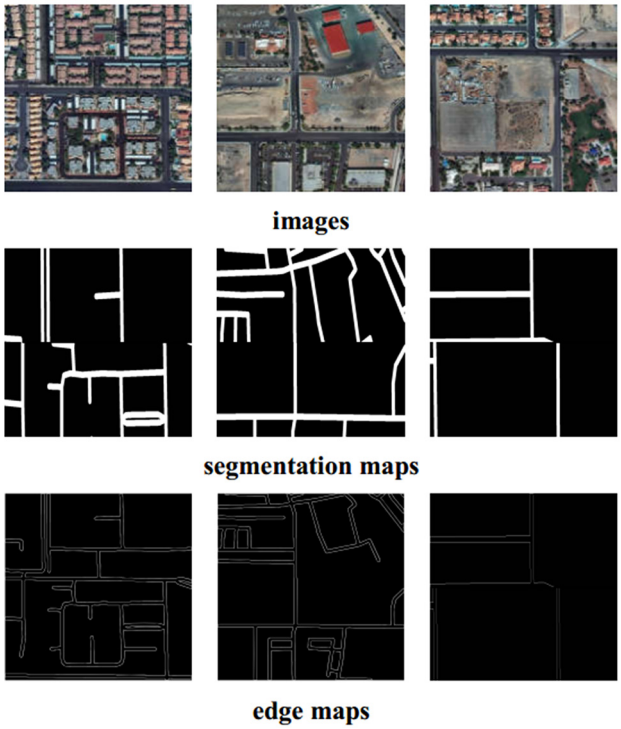

Figure 7. Images and maps of the SpaceNet data set.

Experimental Settings

The proposed ERMS-CNN was evaluated on both data sets using PyTorch (Paszke *et al.* 2017). All the experiments were performed on a server with four Nvidia Titan X Pascal GPU accelerators (with 12 GB of GPU memory). The algorithms we compared were U-Net (Ronneberger *et al.* 2015), ResUNet (He *et al.* 2016), MS-ResUNet, ER-ResUNet, ERMS-ResUNet, LinkNet (Chaurasia and Culurciello 2017), MS-LinkNet, ER-LinkNet, and ERMS-LinkNet. In the training process, the training samples of the two data sets were randomly cropped to 512 × 512 and 1024 × 1024 before being fed into the deep network. For better performance, the ResNet parameters pretrained on ImageNet and data augmentation—including horizontal flip, vertical flip, and diagonal flip—were adopted. The initial learning rate was set to 2×10^{-4}, and was reduced by 5 if the training loss did not decrease over three times. In the inference process, the network takes images of arbitrary size as input and generates probability maps of the same size. We used 0.5 as the threshold to obtain the final road-detection result.

Experimental Results and Analysis

Experiment 1: The Cheng Data Set

The first experiment was conducted on the Cheng data set. The visual comparison of the different methods based on ResUNet is shown in Figure 8, and Table 1 reports the quantitative comparison. The visual comparison of the different methods based on LinkNet is shown in Figure 9, and Table 2 reports the quantitative comparison.

Figure 8 shows the visual comparison of U-Net, ResUNet, MS-ResUNet, ER-ResUNet, and ERMS-ResUNet, where green represents the road being judged as background, red represents the background being judged as road, and blue represents the true positives. The first and second columns are, respectively, the images and maps, and the local area of the image on the left (yellow box area) is shown on the right for better visualization. From the third through seventh columns we can see that the result of U-Net has many red areas, especially near the edge. Part of the reason for this is that the shallow network has limited learning capabilities. Therefore, ResNet is applied to train a deeper network, and road recognition is improved to some extent. However, the road-recognition problem is still far from solved. We expect that this result could be improved by extracting more robust features at multiple scales, and the fifth column confirms that this does indeed work. At the same time, additional edge supervisions are added to the network training, which directs the network to pay more attention to edge-information learning. As can be seen from the sixth column, the additional edge supervisions do indeed help improve road recognition. Based on this, and combined with MS feature extraction, the network can obtain the best result, as shown in the seventh column.

The quantitative results in Table 1 confirm this analysis. The first three columns show the quantitative results of the three full images, and the final column shows the average accuracy of the 30 test images. It can be seen that the proposed ERMS-ResUNet34 achieves the best performance, and ER-LinkNet34 is the second best (better than MS-LinkNet34). The Q of ERMS-ResUNet34 is, respectively, 0.35%, 1.27%, 1.36%, and 4.29% better than those of ER-ResUNet34, MS-ResUNet34, ResUNet34, and U-Net, confirming the superiority of the proposed method. Note also that adding only edge supervisions yields better performance than adding only MS enhancement.

The visual comparison of LinkNet34, MS-LinkNet34, ER-LinkNet34, and ERMS-LinkNet34 is presented in Figure 9. We can see that the proposed ERMS-LinkNet34 has the best performance, eliminating many false positives (red box area). The quantitative comparison in Table 2 reaches the same conclusion, and the Q of ERMS-LinkNet34 is, respectively,

0.33%, 0.74%, and 1.15% better than those of ER-LinkNet34, MS-LinkNet34, and LinkNet34.

Experiment 2: The SpaceNet Data Set

The second experiment was conducted on the SpaceNet road data set, which is a large road data set. Figure 10 displays the visual comparison of the different methods based on ResUNet, and Table 3 shows the quantitative comparison. Figure 11 displays the visual comparison of the different methods based on LinkNet, and the quantitative comparison is presented in Table 4.

Figure 10 shows the visual comparison of U-Net, ResUNet, MS-ResUNet, ER-ResUNet, and ERMS-ResUNet. The visualization result on the right displays the local area of the image on the left. On the whole, the proposed ERMS-ResUNet gives the best results, eliminating many false negatives (red box area). The performance of ER-ResUNet is next. MS-ResUNet is not always better than ResUNet on every image, such as the first image in the red box area, but its average performance over the entire test set is better than that of ResUNet, as can be seen from the quantitative comparison in Table 3. At the same

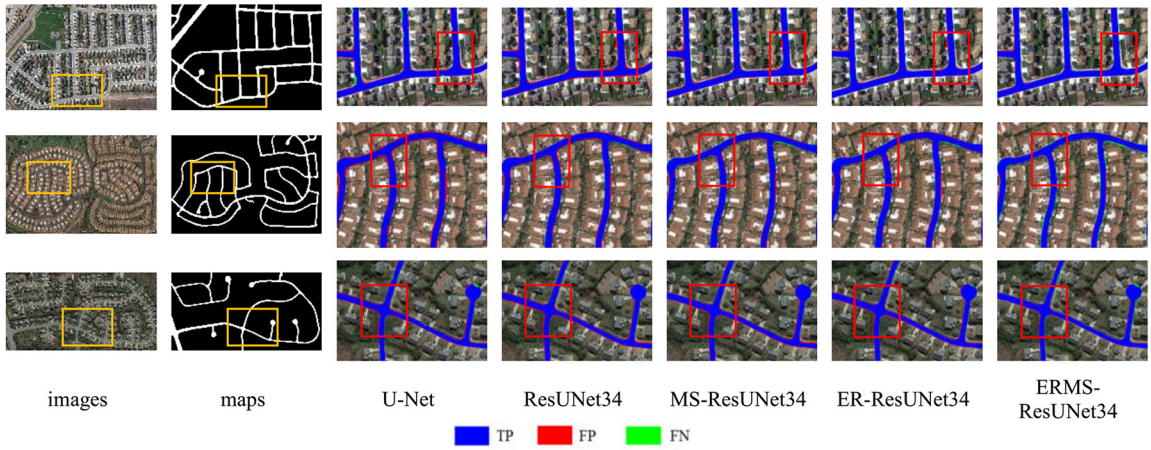

Figure 8. The visual comparison of the methods based on ResUNet on the Cheng data set.

Table 1. Quantitative comparison of the methods based on ResUNet on the Cheng data set.

Method	Image 1			Image 2			Image 3			Average		
	P	R	Q	P	R	Q	P	R	Q	P	R	Q
U-Net	0.9062	0.9505	0.8653	0.8261	0.9867	0.8170	0.8857	0.9480	0.8447	0.9055	0.9224	0.8414
ResUNet34	0.8855	0.9843	0.8732	0.8669	0.9846	0.8552	0.8633	0.9819	0.8498	0.9058	0.9575	0.8707
MS-ResUNet34	0.8934	0.9844	0.8810	0.8902	0.9700	0.8663	0.8788	0.9814	0.8644	0.9079	0.9561	0.8716
ER-ResUNet34	0.9123	0.9766	0.8928	0.8851	0.9741	0.8647	0.8902	0.9801	0.8744	0.9133	0.9612	0.8808
ERMS-ResUNet34	0.9268	0.9667	**0.8981**	0.9391	0.9417	**0.8875**	0.9189	0.9653	**0.8895**	0.9260	0.9515	**0.8843**

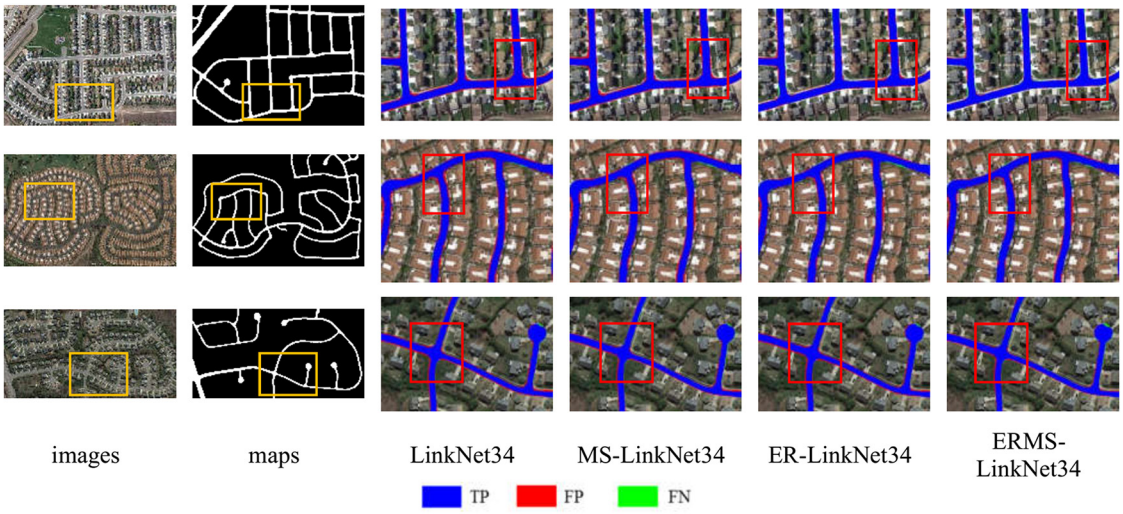

Figure 9. The visual comparison of the methods based on LinkNet on the Cheng data set.

Table 2. Quantitative comparison of the methods based on LinkNet on the Cheng data set.

Method	Image 1			Image 2			Image 3			Average		
	P	R	Q	P	R	Q	P	R	Q	P	R	Q
LinkNet34	0.8781	0.9886	0.8693	0.8354	0.9896	0.8281	0.8632	0.9860	0.8527	0.8909	0.9671	0.8647
MS-LinkNet34	0.8727	0.9865	0.8625	0.8558	0.9838	0.8439	0.8792	0.9787	0.8627	0.8953	0.9670	0.8688
ER-LinkNet34	0.9030	0.9743	0.8820	0.8906	0.9679	0.8650	0.8744	0.9728	0.8536	0.9122	0.9529	0.8729
ERMS-LinkNet34	0.9309	0.9612	**0.8971**	0.8950	0.9661	**0.8677**	0.8902	0.9766	**0.8716**	0.9184	0.9501	**0.8762**

time, Table 3 also verifies the superiority of our proposed method, with its *R* especially displaying a significant advantage (fewer false negatives) and its overall accuracy the best.

Figure 11 displays the visual comparison of LinkNet34, MS-LinkNet34, ER-LinkNet34, and ERMS-LinkNet34. We can see that our proposed ERMS-ResUNet eliminates many false negatives (red box area) and achieves the best performance; and the quantitative comparison in Table 4 leads to the same conclusion.

Conclusions

In this article, an edge-reinforced convolutional neural network is proposed for road detection in very-high-resolution remote sensing imagery. In order to improve road recognition, multiscale feature extraction and edge reinforcement are applied appropriately in the proposed network. In addition, these two operations can be applied to different road-detection networks and obtain the best experimental results. Experiments on the Cheng and SpaceNet road data sets confirm the effectiveness of our proposed method. In our future research, we will explore a more effective method rather than adding additional edge supervision.

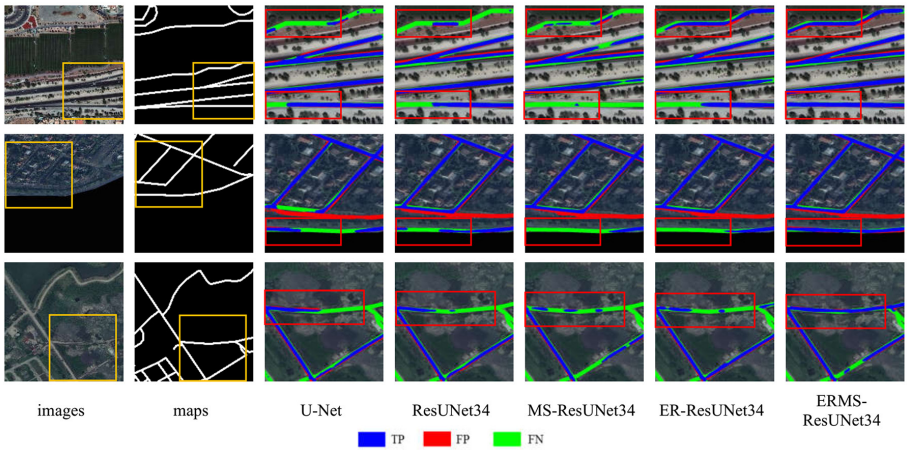

Figure 10. The road-detection results on the Cheng data set.

Table 3. Quantitative comparison of the methods based on ResUNet on the SpaceNet data set.

Method	Image 1			Image 2			Image 3			Average		
	P	R	Q	P	R	Q	P	R	Q	P	R	Q
U-Net	0.8411	0.5809	0.5234	0.6356	0.7430	0.5210	0.7835	0.6719	0.5667	0.7878	0.8023	0.6597
ResUNet34	0.8240	0.5967	0.5293	0.6802	0.7533	0.5562	0.7569	0.5498	0.4673	0.7931	0.8150	0.6721
MS-ResUNet34	0.8366	0.5062	0.4607	0.6838	0.7563	0.5603	0.8595	0.5767	0.5271	0.7933	0.8193	0.6752
ER-ResUNet34	0.8321	0.6102	0.5433	0.6975	0.7542	0.5683	0.8365	0.5848	0.5248	0.7929	0.8170	0.6733
ERMS-ResUNet34	0.8436	0.6647	**0.5918**	0.6979	0.8533	**0.6231**	0.7866	0.6415	**0.5464**	0.7934	0.8253	**0.6793**

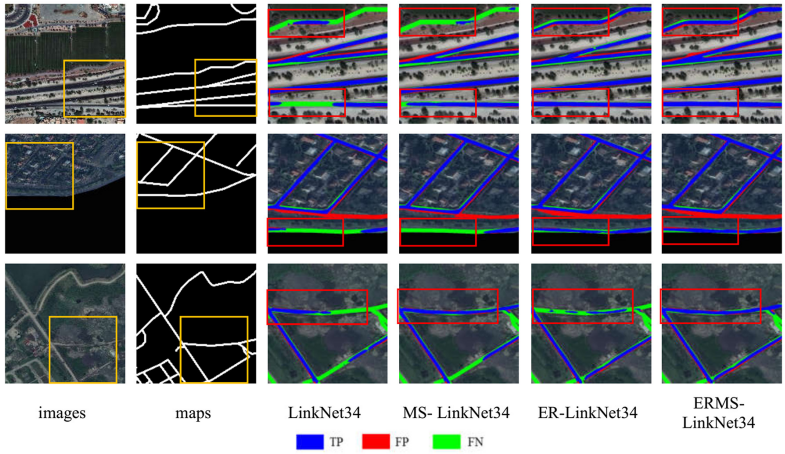

Figure 11. The road-detection results on the Cheng data set.

Table 4. Quantitative comparison of the methods based on LinkNet on the SpaceNet data set.

Method	Image 1			Image 2			Image 3			Average		
	P	R	Q	P	R	Q	P	R	Q	P	R	Q
LinkNet34	0.8467	0.5497	0.4999	0.6662	0.7504	0.5454	0.7847	0.5919	0.5092	0.7928	0.8157	0.6723
MS-LinkNet34	0.8419	0.5627	0.5090	0.6999	0.7455	0.5649	0.8620	0.6260	0.5690	0.7985	0.8169	0.6773
ER-LinkNet34	0.8513	0.7115	0.6329	0.6823	0.8102	0.5883	0.8654	0.5666	0.5207	0.7969	0.8180	0.6769
ERMS-LinkNet34	0.8245	0.7988	**0.6827**	0.6861	0.8342	**0.6037**	0.8606	0.6671	**0.6020**	0.7912	0.8269	**0.6788**

Acknowledgments

This work was supported by the National Natural Science Foundation of China under Grants 41771385 and 41801280.

References

Ammour, N., H. Alhichri, Y. Bazi, B. Benjdira, N. Alajlan and M. Zuair. 2017. Deep learning approach for car detection in UAV imagery. *Remote Sensing* 9 (4):312.

Buslaev, A. V., S. S. Seferbekov, V. I. Iglovikov and A. A. Shvets. 2018. Fully convolutional network for automatic road extraction from satellite imagery. arXiv:1806.05182.

Chaurasia, A. and E. Culurciello. 2017. LinkNet: Exploiting encoder representations for efficient semantic segmentation. Pages 518–521 in *2017 IEEE Visual Communications and Image Processing*, held in St. Petersburg, Fla., 10–13 December 2017. Edited by J. Editor. City, St.: Institute of Electrical and Electronics Engineers.

Cheng, D., G. Meng, S. Xiang and C. Pan. 2017. FusionNet: Edge aware deep convolutional networks for semantic segmentation of remote sensing harbor images. *IEEE Journal of Selected Topics in Applied Earth Observations and Remote Sensing* 10 (12):5769–5783.

Cheng, G., Y. Wang, Y. Gong, F. Zhu and C. Pan. 2014. Urban road extraction via graph cuts based probability propagation. Pages 5072–5076 in *2014 IEEE International Conference on Image Processing*, held in Paris, 27–30 October 2014. Edited by J. Editor. City, St.: Institute of Electrical and Electronics Engineers.

Cheng, G., Y. Wang, S. Xu, H. Wang, S. Xiang and C. Pan. 2017. Automatic road detection and centerline extraction via cascaded end-to-end convolutional neural network. *IEEE Transactions on Geoscience and Remote Sensing* 55 (6):3322–3337.

Cheng, G., F. Zhu, S. Xiang and C. Pan. 2016. Road centerline extraction via semisupervised segmentation and multidirection nonmaximum suppression. *IEEE Geoscience and Remote Sensing Letters* 13 (4):545–549.

He, K., X. Zhang, S. Ren and J. Sun. 2016. Deep residual learning for image recognition. <http://openaccess.thecvf.com/content_cvpr_2016/papers/He_Deep_Residual_Learning_CVPR_2016_paper.pdf> Accessed DD Month YYYY.

Hoareau, G., J. J. Liebenberg, J. G. Musial and T. R. Whitman. 2018. Dynamically establishing a temporary safe route via a network of unmanned aerial vehicles. U.S. Patent 9,897,456, filed January 8, 2016, and issued February 20, 2018.

Kluckner, S., T. Mauthner, P. M. Roth and H. Bischof. 2009. Semantic classification in aerial imagery by integrating appearance and height information. Pages 477–488 in *Computer Vision—ACCV 2009*, held in Xi'an, China, 23–27 September 2009. Edited by H. Zha, R. Taniguchi and S. Maybank. Lecture Notes in Computer Science vol. 5995. Berlin: Springer.

Krizhevsky, A., I. Sutskever and G. E. Hinton. 2012. ImageNet classification with deep convolutional neural networks. Pages 1097–1105 in *Advances in Neural Information Processing Systems 25*, held in Lake Tahoe, Nev., 3–6 December 2012. Edited by F. Pereira, C. J. C. Burges, L. Bottou and K. Q. Weinberger. San Diego, Calif.: Neural Information Processing Systems Foundation.

LeCun, Y., L. Bottou, Y. Bengio and P. Haffner. 1998. Gradient-based learning applied to document recognition. *Proceedings of the IEEE* 86 (11):2278–2324.

Lei, X., W. Wang and J. Lai. 2009. A method of road extraction from high-resolution remote sensing images based on shape features. *Acta Geodaetica et Cartographica Sinica* 38 (5):457–465.

Liu, S., W. Ding, C. Liu, Y. Liu, Y. Wang and H. Li. 2018. ERN: Edge loss reinforced semantic segmentation network for remote sensing images. *Remote Sensing* 10 (9):1339.

Long, J., E. Shelhamer and T. Darrell. 2015. Fully convolutional networks for semantic segmentation. <https://www.cv-foundation.org/openaccess/content_cvpr_2015/papers/Long_Fully_Convolutional_Networks_2015_CVPR_paper.pdf> Accessed DD Month YYYY.

Lv, J.-G. and C.-T. Wei. 2009. Urban straight road extraction from high-resolution remote sensing image based on Hough transform. *Remote Sensing Information* 2009 (3):006.

Maggiori, E., Y. Tarabalka, G. Charpiat and P. Alliez. 2017. High-resolution aerial image labeling with convolutional neural networks. *IEEE Transactions on Geoscience and Remote Sensing* 55 (12):7092–7103.

Marmanis, D., K. Schindler, J. D. Wegner, S. Galliani, M. Datcu and U. Stilla. 2018. Classification with an edge: Improving semantic image segmentation with boundary detection. *ISPRS Journal of Photogrammetry and Remote Sensing* 135:158–172.

Matsugu, M., K. Mori, Y. Mitari and Y. Kaneda. 2003. Subject independent facial expression recognition with robust face detection using a convolutional neural network. *Neural Networks* 16 (5–6):555–559.

Mena, J. B. 2003. State of the art on automatic road extraction for GIS update: A novel classification. *Pattern Recognition Letters* 24 (16):3037–3058.

Mnih, V. 2013. Machine learning for aerial image labeling. Ph.D. dissertation, University of Toronto.

Mnih, V. and G. E. Hinton. 2010. Learning to detect roads in high-resolution aerial images. Pages 210–223 in *Computer Vision—ECCV 2010*, held in Heraklion, Greece, 5–11 September 2010. Edited by K. Daniilidis, P. Maragos and N. Paragios. Lecture Notes in Computer Science vol. 6316. Berlin: Springer.

Paszke, A., S. Gross, S. Chintala, G. Chanan, E. Yang, Z. DeVito, Z. Lin, A. Desmaison, L. Antiga and A. Lerer. 2017. Automatic differentiation in PyTorch. <https://openreview.net/pdf?id=BJJsrmfCZ> Accessed DD Month YYYY.

Qulin, T. 2010. Urban building extraction from VHR multi-spectral images using object-based classification. *Acta Geodaetica et Cartographica Sinica* 39 (6):618–623.

Ronneberger, O., P. Fischer and T. Brox. 2015. U-net: Convolutional networks for biomedical image segmentation. Pages 234–241 in *Medical Image Computing and Computer-Assisted Intervention—MICCAI 2015*, held in Munich, Germany, 5–9 October 2015. Edited by N. Navab, J. Hornegger, W. Wells and A. Frangi. Lecture Notes in Computer Science vol. 9351. Berlin: Springer.

Saalmüller, A., S. Jonjic, H. J. Bühring, M. J. Reddehase and U. H. Koszinowski. 2009. Road extraction from high-resolution remote sensing images based on spectral and shape features. *Proceedings of SPIE* 7495:74953R.

Shi, W., Z. Miao and J. Debayle. 2014. An integrated method for urban main-road centerline extraction from optical remotely sensed imagery. *IEEE Transactions on Geoscience and Remote Sensing* 52 (6):3359–3372.

Singh, S., A. Batra, G. Pang, L. Torresani, S. Basu, M. Paluri and C. V. Jawahar. 2018. Self-supervised feature learning for semantic segmentation of overhead imagery. <https://www.researchgate.net/profile/Suriya_Singh/publication/327546680_Self-Supervised_Feature_Learning_for_Semantic_Segmentation_of_Overhead_Imagery/links/5c0d868ba6fdcc494fe880c1/Self-Supervised-Feature-Learning-for-Semantic-Segmentation-of-Overhead-Imagery.pdf> Accessed DD Month YYYY.

Soulard, C. E., W. Acevedo and S. V. Stehman. 2018. Removing rural roads from the National Land Cover Database to create improved urban maps for the United States, 1992 to 2011. *Photogrammetric Engineering and Remote Sensing* 84 (2):101–109.

Van Etten, A., D. Lindenbaum and T. M. Bacastow. 2018. SpaceNet: A remote sensing dataset and challenge series. arXiv:1807.01232.

Wang, J., J. Song, M. Chen and Z. Yang. 2015. Road network extraction: A neural-dynamic framework based on deep learning and a finite state machine. *International Journal of Remote Sensing* 36 (12):3144–3169.

Zhu, C., Y. Wang, Q. Ma and W.-Z. Shi. 2004. Road extraction from high-resolution remotely sensed image based on morphological segmentation. *Acta Geodaetica et Cartographica Sinica* 33 (4):347–351.

The Application of Bidirectional Reflectance Distribution Function Data to Recognize the Spatial Heterogeneity of Mixed Pixels in Vegetation Remote Sensing: A Simulation Study

Yanan Yan, Lei Deng, and XianLin Liu

Abstract

Spectral decomposition of mixed pixels can provide information about the abundance of end members but fails to indicate the spatial distribution of end members in vegetation remote sensing. This work is a significant attempt to use the bidirectional reflectance distribution function (BRDF) characteristics of mixed pixels in the prediction of spatial-heterogeneity metrics. Data sets from this function with different spatial distributions were constructed by the discrete anisotropic radiative transfer model, and three spatial aggregation and dispersion metrics were calculated: percentage of like adjacencies, spatial division index, and aggregation index. A simple linear regression method was used to construct the prediction model of spatial aggregation and dispersion metrics. The potential of multiangle remote sensing model for identifying spatial patterns well was demonstrated, and its importance was found to differ for different spatial aggregation and dispersion metrics. Specifically, the precision of the model based on multiangle reflectance used for predicting the spatial division index could meet a minimum root mean square of 5.95%. The reflectance features from backward observation on the principal plane play the leading role in recognizing the spatial heterogeneity of mixed pixels. The prediction model is sufficiently robust to distinguish the same vegetation with different growth trends, but also performs well when the ground objects have a smaller reflectance difference in the mixed pixels in a certain band. This study is expected to offer a new thought for spatial-heterogeneity identification of ground objects and thus promote the development of remote sensing technology in assessing spatial distribution.

Introduction

Remote sensing technology is of great significance in studying the dynamic characteristics of the spatial distribution of vegetation under the comprehensive control of environmental heterogeneity and disturbance (Patrick and Ellery 2007; Uuemaa *et al.* 2009; Liu *et al.* 2014). It contributes to revealing the interaction between vegetation cover and natural factors and human disturbance (Saadat *et al.* 2011; Jin *et al.* 2012; Cheng *et al.* 2018; Cleemput *et al.* 2018).

The ground reflectance or emission spectrum signals acquired by remote sensors is recorded in units of pixels. In most cases, there are many mixed pixels, which record comprehensive spectral information of various surface types (Bosdogianni, Petrou and Kittler 1994). It not only affects the accuracy of recognition and classification of land features but also is one of the main challenges facing the development of remote sensing science toward quantification (S. Wu *et al.* 2018; Zhang *et al.* 2018). Spectral mixture analysis is one of the main topics in quantitative remote sensing research (C. Wu and Murray 2003). It is able to provide land cover information at subpixel levels for practical applications (Zhao *et al.* 2016). Presently, research on the mixed-pixel effect in vegetation mapping mostly focuses on extracting estimates of end-member abundance by using a spectral unmixing model (Mylona *et al.* 2017). The end-member abundance analysis results are used to improve the accuracy of land use type area extraction and quantitative parameter inversion (Zhao *et al.* 2016). However, little research has been done on the spatial heterogeneity of mixed pixels. Understanding the spatial heterogeneity of mixed pixels is of great significance to image classification, landscape analysis, and pixel-scale conversion.

For traditional single-direction remote sensing, reflectances of ground objects are obtained from vertical observation but lacking sufficient information to infer the main material spectrum and spatial structure. Multidirectional information of a target ground object can be obtained by multiangle observation, which can enrich the observation information and help extract more detailed and reliable three-dimensional spatial-structural parameters of the ground object than exclusive one-directional observation (Diner *et al.* 1999; Jiao *et al.* 2018). This study attempted to extract and analyse the bidirectional reflectance distribution function (BRDF) characteristics (Gatebe and King 2016) of the mixed pixels to recognize their spatial heterogeneity. The combination with overlapped remote sensing image sets taken by unmanned aerial vehicle-based remote sensing technology is expected to efficiently and accurately acquire the BRDF of scenes (Mu *et al.* 2018; Roosjen *et al.* 2018). In addition, with the development of multiangle remote

Yanan Yan is with the China Institute of Water Resources and Hydropower Research, Beijing 100038, China; Beijing IWHR Technology Co., Ltd., Beijing 100038, China; and the College of Resource Environment and Tourism, Capital Normal University, Beijing 100048, China.

Lei Deng is with the College of Resource Environment and Tourism, Capital Normal University, Beijing 100048, China; and the Key Laboratory of 3D Information Acquisition and Application, Ministry of Education, Capital Normal University, Beijing 100048, China (edenglei@139.com).

XianLin Liu is with the College of Resource Environment and Tourism, Capital Normal University, Beijing 100048, China; and the Chinese Academy of Surveying and Mapping, Beijing 100830, China.

Photogrammetric Engineering & Remote Sensing
Vol. 86, No. 3, March 2020, pp. 161–167.
0099-1112/20/161–167

doi: 10.14358/PERS.86.3.161

sensing satellites such as MODIS and MISR (Thome, Biggar and Choi 2004; Wei and Fang 2016), this study would be applied to remote sensing for investigating the spatial heterogeneity of mixed pixels in vegetation remote sensing.

All in all, spectral mixture analysis of mixed pixels can provide information about the abundance of end members, but it fails to predict their spatial distribution. This article proposes a method to identify the spatial heterogeneity of mixed pixels by using the BRDF data. The objectives of this study were threefold: to develop a potential modelling method to accurately describe the spatial heterogeneity of mixed pixels by using BRDF data, to elaborate the contribution of different multiangle observation data acquired from BRDF to recognize spatial heterogeneity, and to investigate the robustness of the model from the points of vegetation height and leaf area index. The results have important application potential in land cover change detection, remote sensing image scale conversion, and other fields.

Data Sets

This study adopted simplified scene settings to explore the possibility of recognizing the spatial heterogeneity of mixed pixels using BRDF characteristics, hoping to provide a basis for the future study of more complex distribution patterns of ground objects. Therefore, grass and bare soil were selected as research objects. In this section of the article, the setting of the spatial-distribution pattern in each mixed pixel is introduced, and then BRDF data of the modeled scene for each mixed pixel is constructed through discrete anisotropic radiative transfer (DART) software (Malenovský *et al.* 2008).

Vegetation Spatial-Distribution Setting in Each Mixed Pixel

In order to simplify things, the spatial-distribution pattern was set in 3 × 3 grids, as shown in Figure 1, giving nine orientations (east, south, west, north, southeast, southwest, northwest, northeast, and center). Additionally, the distribution of the 9-grid can be regarded as the basic pattern of other distribution modes. In Figure 1, the black square represents a block of grass and the white represents bared land. There are a total of 512 scenario distribution modes.

DART Simulation Data

(DART (Gastellu-Etchegorry *et al.* 2015) can be used to obtain remote sensing images with scene, spatial resolution, and sensor parameters corresponding to the field flight experiments. Developed by the French Centre d'Études Spatiales de la Biosphère laboratory, DART is known to be one of the most comprehensive three-dimensional radiation transmission models, and it can provide easily accessible multiangle data resources for research on this issue. DART is a forward model based on the theory of three-dimensional radiation transmission that uses a variety of simulation methods, including ray tracing and quasi–Monte Carlo photon tracking, which can simulate the radiation transmission process in different scenes and obtain various physical parameters such as reflectance in various bands and directions.

The DART software was used to obtain the BRDF data for each vegetation spatial distribution. Firstly, virtual scenes were constructed according to spatial-distribution patterns (see previous section). Targets were set to Lambertian models, which were isotropic. Isotropy refers to the property that the physical and chemical properties of an object will not change with different directions—that is, the performance values of an object measured in different directions are exactly the same—also known as *homogeneity*. Optical properties of the vegetation (grass) and background (sand) are shown in Figure 2. The DART simulations were conducted in flux-tracking mode. Flux tracking is an extension of classical ray-tracing methods with additional energetic features (Arasa *et al.* 2004). We applied 512 scenarios corresponding to different

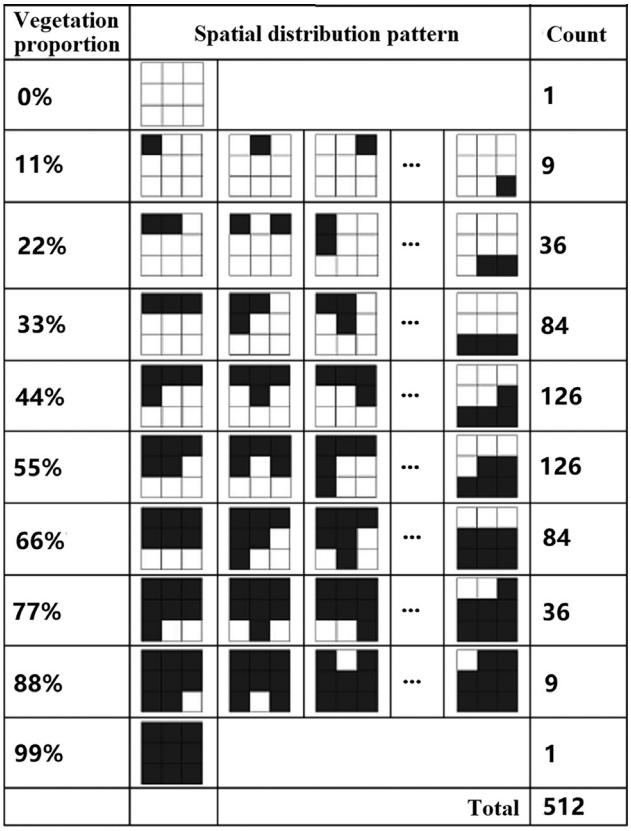

Figure. 1. Illustration of spatial-distribution pattern of vegetation.

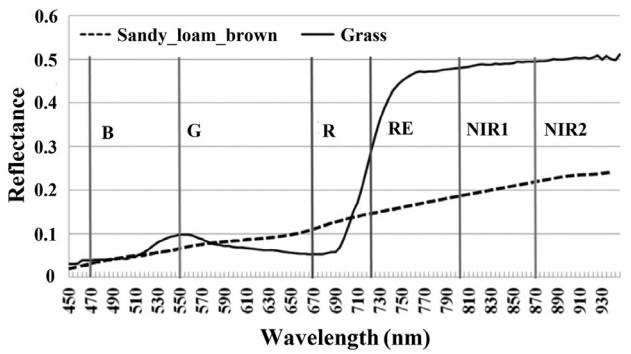

Figure 2. Spectral curves of grass and bared land (sandy_loam_brown), and six bands for modeling research.

spatial distributions. In order to increase the complexity of vegetation growth, the leaf area index was set to 2, 3, and 4, corresponding to vegetation heights of 20, 30, and 40 cm. A total of 4608 samples were obtained. DART-modeled spectral images were generated for each scenario at the following wavelengths: blue band (470 nm), green band (550 nm), red band (670 nm), red-edge band (722 nm), near-infrared band 1 (802 nm), and near-infrared band 2 (870 nm); the setting of spectral attributes refers to the Cubert UHD 185 hyperspectral sensor (Deng *et al.* 2018). The DART variables used for the 512 scenario simulations are summarized in Table 1.

Methods

The application of BRDF data to recognize the spatial heterogeneity of mixed pixels was composed of three parts: description of spatial heterogeneity within pixels, spatial-heterogeneity metrics prediction model based on BRDF characteristics,

Table 1. Input variables for the discrete anisotropic radiative transfer (DART) scenes used to generate hyperspectral images for four study scenarios.

DART Input Variable	Scenario1~Scenario512
Sun position	
Zenith angle (°)	30
Azimuth angle (clockwise from north; (°)	175
Spectral bands	Full width at half maximum = 8 nm
Central wavelength (nm)	
Blue	B470
Green	G550
Red	R670
Red-edge	R722
Near-infrared band 1	N 1:802
Near-infrared band 2	N 2:870
Scene parameters	Study site
Cell size (*x*, *y*, *z*; m)	0.2 × 0.2 × 0.1
Scene dimensions (*x*, *y*; m)	0.6 × 0.6
Spatial distribution	512 scenarios[a]
Leaf area index (LAI) & vegetation height (cm), one plot	2, 20 2, 30 2, 30 3, 20 3, 30 3, 30 4, 20 4, 30 4, 30
Soil	2D Lambertian model
Target parameters	Lambertian

[a]In text, under Vegetation Spatial-Distribution Setting in Each Mixed Pixel.

and model accuracy assessment. The details are given in the following sections.

Description of Spatial Heterogeneity Within Pixels

Percentage of like adjacencies (PLADJ; Equation 1), spatial division index (DIVISION; Equation 2), and aggregation index (AI; Equation 3) were calculated with Fragstats 3.4 software (O'Neill *et al.*, 1988) to describe the spatial heterogeneity within pixels.

PLADJ is calculated as

$$\mathrm{PLADJ} = \left[\frac{\sum_{i=1}^{m} g_{ii}}{\sum_{i=1}^{m} \sum_{k=1}^{m} g_{ik}} \right] \times 100, \tag{1}$$

where g_{ii} is the number of nodes between patch type i and patch type i calculated based on the double method, and g_{ik} is the number of nodes between patch type i and patch type k calculated based on the double method.

DIVISION is calculated as

$$\mathrm{DIVISION} = \left[1 - \sum_{i=1}^{m} \sum_{j=1}^{m} \left(\frac{a_{ij}}{A} \right)^2 \right], \tag{2}$$

where a_{ij} is the area of patch ij, and A is the total area of the landscape.

AI is calculated as

$$\mathrm{AI} = \left[\sum_{i=1}^{m} \left(\frac{g_{ii}}{\max g_{ii}} \right) P_i \right] \times 100, \tag{3}$$

where P_i refers to the area proportion of patch type i in the landscape.

These metrics reflect the spatial structural composition, and characterize some aspects of the spatial configuration. PLADJ is calculated by the adjacency matrix, which can characterize the probability of one patch type appearing adjacent to another on a spatial map. Therefore, it can be used to measure the aggregation degree of a characteristic patch type, whose minimum value corresponds to the maximum dispersion, and vice versa. PLADJ numerically equals the division of the number of adjacencies to a certain type of patch by the number of all adjacencies to this patch, multiplied by 100 to obtain a percentage. When a certain type of patch is maximally dispersed—which means there is no adjacency—PLADJ equals 0.

DIVISION characterizes the probability that two randomly selected pixels are not in the same patch. Values range from 0 to 1, with higher values meaning higher fragmentation and 0 when there is only one path.

AI indicates the degree of aggregation (distribution pattern) of individuals within the group. Many forms of AI can be used to analyze the distribution frequency of individuals in each interval. When the fragmentation degree of a certain type of patches reaches the maximum, AI equals 0; as the aggregation increases, the AI value grows, reaching 100 when the patches become a compact whole.

Spatial-Heterogeneity Metrics Prediction Model Based on BRDF Characteristics

BRDF Angular Sampling

BRDF angular sampling of each sample was used in the study with observations originating from the principal and cross planes. Considering the limitation of the maximum view zenith angle obtained from remote sensing sensors, the view zenith angle was set to a maximum of 55° and sampled at intervals of 10°. Figure 3 shows the angular sampling of each sample used in the study.

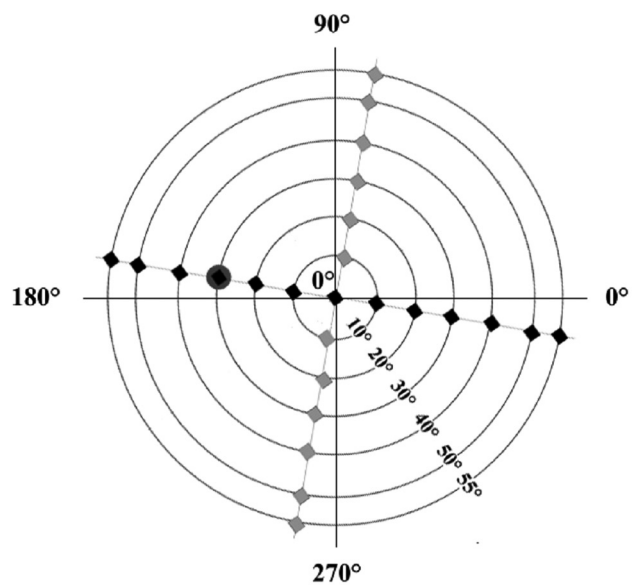

Figure 3. Bidirectional reflectance distribution function angular sampling of each sample used in the study, with observations originating from the principal and cross planes. The circle point indicates the solar position. Polar radius represents zenith angle, and polar angle represents azimuth angle in polar coordinates.

Prediction-Model Building

The purpose of this article is to investigate the validity of multiangle observation data in predicting spatial metrics, so the complexity of the algorithm model is not addressed here. A simple linear regression model (Raftery, Madigan and Hoeting 1997) was adopted to construct the prediction model. The model is a regression analysis that uses a least-square function called a linear regression equation to model the relationship between one or more independent variables and dependent variables. In this article, dependent variables are the spatial-heterogeneity metrics. There are two independent variables: the reflectance data obtained directly from the vertical observation angle, and the reflectance data from the multiangle vertical observation according to BRDF angular sampling. Prediction models were constructed in the blue, green, red, red-edge, near-infrared 1, and near-infrared 2 bands. Sixty percent of the samples were used for modeling, and the rest for validation.

Model Accuracy Assessment

The correlation coefficient and relative root mean square error (RRMSE; Equation 4) were used as evaluation standards to provide an overall assessment of the method in this article. The correlation coefficient indicates the degree of fit between simulated and measured values; the closer the value is to 1, the higher the reference value of the fitting curve. The RRMSE is mainly used for model validation, reflecting the deviation between simulated and measured values. The smaller the value is, the higher the precision of the model:

$$\mathrm{RRMSE} = \sqrt{\frac{\sum_{i=1}^{n}\left(\mathrm{metric}_{\mathrm{ref},i} - \mathrm{metric}_{\mathrm{mod},i}\right)^2}{n}} \times \frac{n}{\sum_{i=1}^{n}\mathrm{metric}_{\mathrm{ref},i}} \times 100. \quad (4)$$

Results

Evaluation Results of the Prediction Model

Regression models for prediction of spatial-heterogeneity metrics were constructed by using vertical and multiangle reflectance data. The evaluation results of the applicability of the model are shown in Figure 4. For the three divergence indices, the model based on multiangle reflectance (MA-model) is more accurate than the model based on single vertical-angle reflectance (0°-model) in all bands. The ascending order of accuracy of bands in the 0°-model was red-edge, green, blue, red, and near-infrared. In the red-edge band, the accuracy of the model is very poor, and in the near-infrared band, the correlation index of the model is relatively high. The reflectance difference of samples in the red-edge band is the smallest, and that in near-infrared bands is obvious. The results show that in the near-infrared band, the vertical observation of mixed spectra of scenes is highly correlated with the spatial pattern. Fortunately, the prediction accuracy in all bands was, to a large extent, improved by MA-models. Among them, the near-infrared-band model improves accuracy less, and the visible-band model improves accuracy more, especially in the red-edge band.

Figure 4 reveals that the models for DIVISION are the best, followed by the models for PLADJ and then the models for AI; the average correlations corresponding to the six bands are 0.94, 0.82, and 0.65, respectively, and the average RRMSE values are 7.14%, 30.31%, and 38.15%. The relatively large errors between the simulation and reference

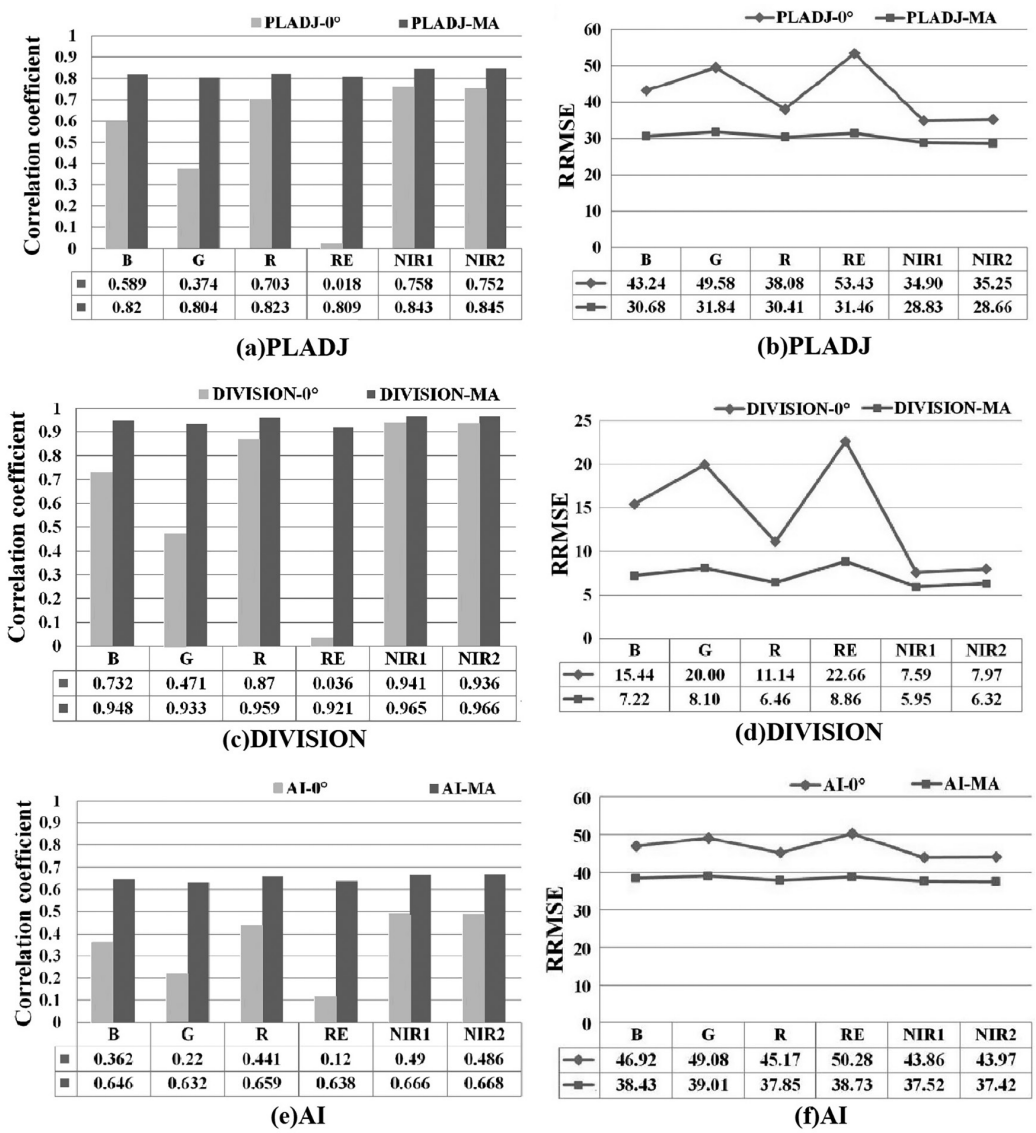

Figure 4. Accuracy evaluation between the reference value and predictive values obtained from models based on multiangle reflectance (MA-model) and single vertical-angle reflectance (0°-model).

values in the models for AI and PLADJ show that the multiangle data improved the prediction accuracy but failed to meet the requirement of the practical application. In contrast, there was small error between the simulation and true values in the MA-models for DIVISION, which indicates that based on multiangle observation data, DIVISION prediction can be well achieved by a simple linear regression model. As shown in Figure 4c and 4d, DIVISION prediction is well implemented by the 0°-model in the near-infrared band, which can be attributed to the high reflectance difference (approximately 0.3) between the grass and the bare land. Such a high reflectance difference between ground objects can have an obvious influence on the sensitivity of the reflectances of mixed pixels to the spatial distribution. Therefore, DIVISION prediction precision can be improved by multiangle observation data when the reflectance difference among ground objects in a band is small.

To conclude, the DIVISION prediction model based on multiangle observation data was applicable. We then compared the applicability of the 0°-model and the MA-model. Figure 5 shows the reference values of DIVISION with the predicted values created with the 0°-model and the MA-model, both of which achieve relatively precise prediction in the whole range. The highest precision is achieved in the near-infrared band, as shown in Figure 5e and 5f. Compared with the 0°-model, the MA-model mainly improved the prediction precision of the first and second halves of the DIVISION range in the near-infrared band.

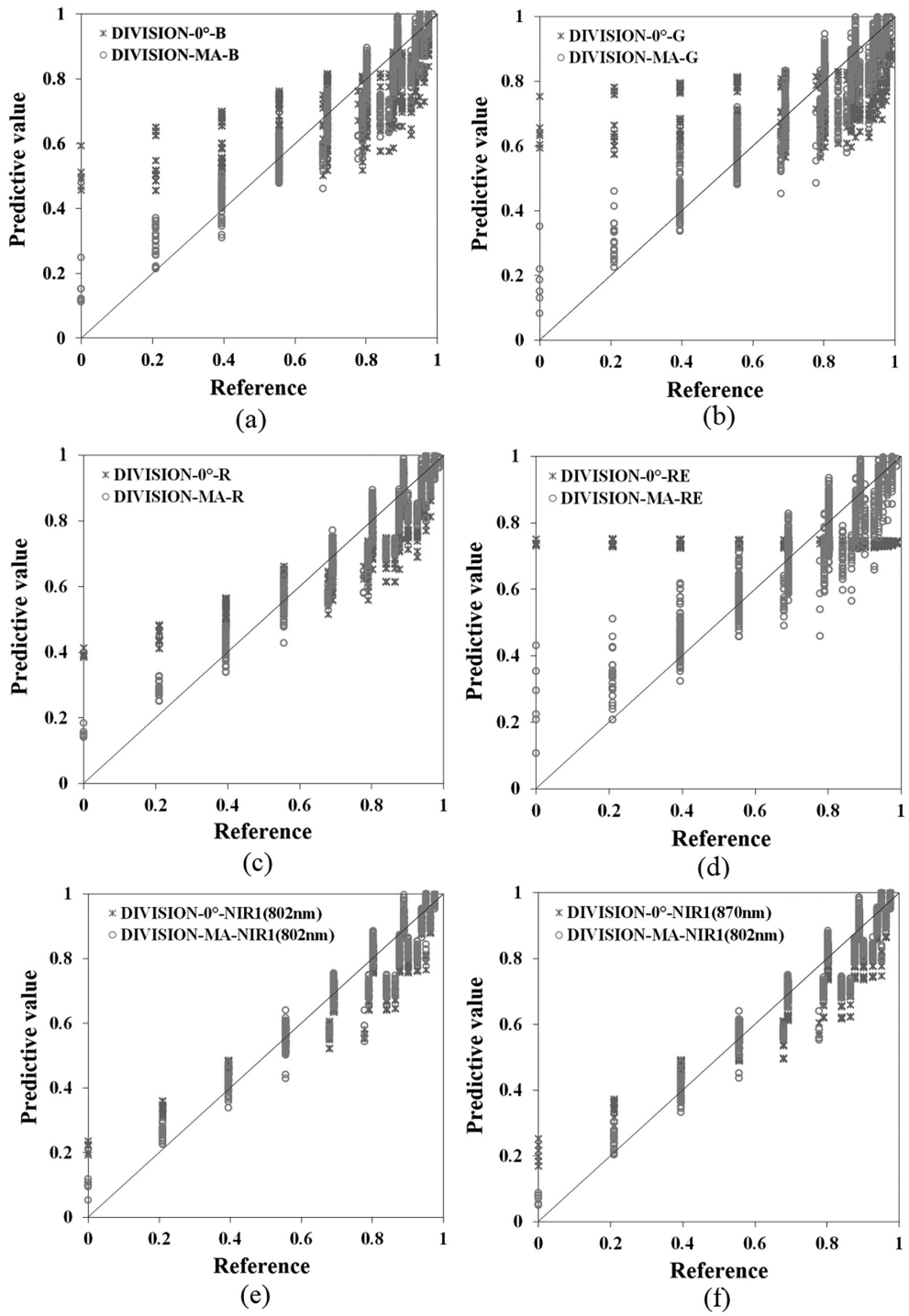

Figure 5. Comparison of the reference value of the spatial division index with the predicted value created with the model based on multiangle reflectance. (a) Blue band, (b) green band, (c) red band, (d) red-edge band, (e) near-infrared band (802 nm), and (f) near-infrared band (870 nm).

Contribution of Different Multiangle Observation Data Acquired from BRDF

To investigate the influence of the observation angle on the precision of the DIVISION prediction model, we calculated the difference of the observation angle in the MA-model in different bands. As shown in Figure 6, the *x*-axis represents the observation zenith angles of the principal and cross planes, and the *y*-axis represents different bands. The circle size is proportional to the importance. The importance of features was calculated using SPSS Clementine software, and the indicators included the sensitivity and information gain contribution. The observation angle on the principal plane was found to be much more important than that on the cross plane. Specifically, the backward observation angle is more important than the forward one on the principal plane, with important angles concentrated in the interval of [−30°, 10°]. On the cross plane, angles of −40°, −20°, 20°, and 40° are important; 40° is the most important for the blue-green band the near-infrared band. It is safe to conclude that the backward reflection features are more sensitive to the structural information of scenes on the principal observation plane than are the forward ones. This understanding is important for the selection of observation angles in applying multiangle remote sensing to identify the spatial heterogeneity of ground objects.

Influence of Vegetation Height and Leaf Area Index (LAI) on the Identification Using DIVISION

The effect of physiological parameters of vegetation on the model accuracy is discussed from the perspectives of vegetation height and LAI. The original multiangle observation data samples were first divided into three sets according to grass heights of 20, 30, and 40 cm. The original samples were then again divided into three sets according to LAI values of 2, 3, and 4. Based on these six data sets, a simple regression model was used to construct the DIVISION prediction model, with the precision evaluation results shown in Table 2.

Excellent prediction precision was achieved in MA-models constructed for different physiological parameters of vegetation (Table 2), as demonstrated by the strong correlation (> 95%) between the prediction and true values in each model in each band and the small RRMSE (< 8%). In terms of the vegetation height, 30 cm contributed to the best prediction results, with the RRMSE reaching as low as 4.88%. As for LAI, all large errors occurred in the sets with an LAI value of 4. This phenomenon depends on the relationships among vegetation height, imaging resolution, and solar altitude; relevant issues will be discussed in a future study.

Conclusion

This study explored the applicability of the BRDF characteristics of mixed pixels in recognition of spatial heterogeneity. BRDF data sets of different spatial distributions were constructed by the DART model, and the landform aggregation and dispersion metrics (i.e., PLADJ, DIVISION, and AI) of each spatial distribution were calculated. Moreover, a simple linear regression method was used to construct the prediction model of the spatial-heterogeneity metrics. Sensitivity analyses were implemented from the perspectives of observation-angle importance and the physiological parameters of vegetation. The specific conclusions are as follows:

- The proposed method based on BRDF data has great potential in identifying spatial patterns of mixed pixels. The precision of the MA-model used for DIVISION prediction could meet a minimum RRMSE of 5.95%.
- The backward reflection features on the principal plane play the leading role in the recognition of the spatial heterogeneity of mixed pixels.
- The prediction model has great potential in distinguishing the same vegetation with different growth trends, and also performs well when the ground objects have a smaller reflectance difference in the mixed pixels in a certain band.

This study efficiently applied BRDF data to identify the spatial heterogeneity of mixed pixels and thus would promote the development of remote sensing technology in assessing spatial distribution. It is beneficial for landscape pattern evolution and scale conversion of remote sensing images. In addition, the application of multiangle UAV and satellite data for the prediction of spatial heterogeneity of mixed pixels will be developed in coming research. The relationships among physiological parameters of vegetation and imaging resolution will be systematically analysed, and more types of indices for describing spatial distribution will be explored in the future.

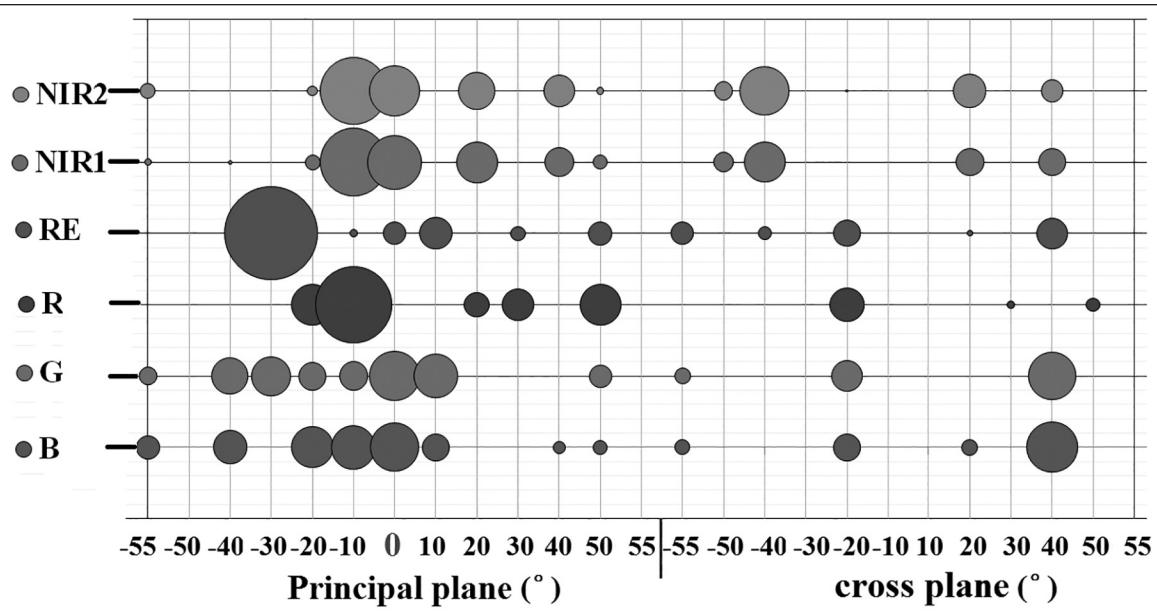

Figure 6. Bubble map displaying the importance of observation angles in different bands.

Table 2. Influence of physiological parameters of vegetation on model precision.[a]

Parameter	Relative root mean square error						R^2					
	B	G	R	RE	NIR1	NIR2	B	G	R	RE	NIR1	NIR2
Vegetation height												
20 cm	5.51	5.88	5.13	6.13	5.01	5.01	0.973	0.968	0.975	0.965	0.977	0.976
30 cm	5.38	5.63	5.38	5.76	4.88	4.88	0.973	0.971	0.974	0.969	0.978	0.977
40 cm	5.63	7.01	5.51	7.38	5.13	5.13	0.971	0.955	0.971	0.95	0.976	0.976
Leaf area index												
2	5.50	5.88	5.13	6.13	5.00	5.00	0.973	0.968	0.975	0.965	0.977	0.976
3	7.25	5.00	6.00	6.00	5.38	5.38	0.95	0.977	0.966	0.966	0.974	0.973
4	5.63	7.00	5.50	7.38	5.13	5.13	0.971	0.955	0.971	0.95	0.976	0.976

[a]Abbreviations: B = blue; G = green; R = red; RE = red -edge; NIR1 = near-infrared band 1; NIR2 = near-infrared band 2.

References

Alphan, H. and N. Çelik. 2016. Monitoring changes in landscape pattern: Use of Ikonos and Quickbird images. *Environmental Monitoring and Assessment* 188:81.

Anchang, J. Y., E. O. Ananga and R. Pu. 2016. An efficient unsupervised index based approach for mapping urban vegetation from IKONOS imagery. *International Journal of Applied Earth Observation and Geoinformation* 50:211–220.

Arasa, J., S. Bosch, J. Ferre-Borrull and C. Pizarro. 2004. Comparison of flux-tracing-based and diffraction-based strategies for optical system evaluation. *Proceedings of SPIE* 5249:34–41.

Bosdogianni, P., M. Petrou and J. Kittler. 1994. Mixed pixel classification in remote sensing. *Proceedings of SPIE* 2315: 494–505.

Deng, L.,, Y. Yan, H. Gong, F. Duan and R. Zhong. 2018. The effect of spatial resolution on radiometric and geometric performances of a UAV-mounted hyperspectral 2D imager. *ISPRS Journal of Photogrammetry and Remote Sensing* 144:298–314.

Diner, D. J.,, G. P. Asner, R. Davies, Y. Knyazikhin, J.-P. Muller, A. W. Nolin, B. Pinty, C. B. Schaaf and J. Stroeve. 1999. New directions in Earth observing: Scientific applications of multiangle remote sensing. *Bulletin of the American Meteorological Society* 80 (11):2209–2228.

Gastellu-Etchegorry, J.-P., T. Yin, N. Lauret, T. Cajgfinger, T. Gregoire, E. Grau, J.-B. Feret, M. Lopes, J. Guilleux, G. Dedieu, Z. Malenovský, B. D. Cook, D. Morton, J. Rubio, S. Durrieu, G. Cazanave, E. Martin and T. Ristorcelli. 2015. Discrete anisotropic radiative transfer (DART 5) for modeling airborne and satellite spectroradiometer and LIDAR acquisitions of natural and urban landscapes. *Remote Sensing* 7 (2):1667–1701.

Gatebe, C. K. and M. D. King. 2016. Airborne spectral BRDF of various surface types (ocean, vegetation, snow, desert, wetlands, cloud decks, smoke layers) for remote sensing applications. *Remote Sensing of Environment* 179:131–148.

Jia, K.,, S. Liang, X. Gu, F. Baret, X. Wei, X. Wang, Y. Yao, L. Yang and Y. Li. 2016. Fractional vegetation cover estimation algorithm for Chinese GF-1 wide field view data. *Remote Sensing of Environment* 177:184–191.

Jiao, Z.,, X. Zhang, F.-M. Bréon, Y. Dong, C. B. Schaaf, M. Román, Z. Wang, L. Cui, S. Yin, A. Ding and J. Wang. 2018. The influence of spatial resolution on the angular variation patterns of optical reflectance as retrieved from MODIS and POLDER measurements. *Remote Sensing of Environment* 215:371–385.

Lantz, N. J. and J. Wang. 2013. Object-based classification of Worldview-2 imagery for mapping invasive common reed, *Phragmites australis*. *Canadian Journal of Remote Sensing* 39 (4):328–340.

Liu, G., L. Zhang, Q. Zhang, Z. Musyimi and Q. Jiang. 2014. Spatio-temporal dynamics of wetland landscape patterns based on remote sensing in Yellow River Delta, China. *Wetlands* 34 (4):787–801.

Malenovský, Z.,, E. Martin, L. Homolová, J.-P. Gastellu-Etchegorry, R. Zurita-Milla, M. E. Schaepman, R. Pokorný, J.G.P.W. Clevers and P. Cudlín. 2008. Influence of woody elements of a Norway spruce canopy on nadir reflectance simulated by the DART model at very high spatial resolution. *Remote Sensing of Environment* 112 (1):1–18.

Mu, X., W. Song, Z. Gao, T. R. McVicar, R. J. Donohue and G. Yan. 2018. Fractional vegetation cover estimation by using multi-angle vegetation index. *Remote Sensing of Environment* 216:44–56.

Mylona, E. A., O. A. Sykioti, K. D. Koutroumbas and A. A. Rontogiannis. 2017. Spectral unmixing-based clustering of high-spatial resolution hyperspectral imagery. *IEEE Journal of Selected Topics in Applied Earth Observations and Remote Sensing* 10 (8):3711–3721.

O'Neill, R. V.,, J. R. Krummel, R. H. Gardner, G. Sugihara, B. Jackson, D. L. DeAngelis, B. T. Milne, M. G. Turner, B. Zygmunt, S. W. Christensen, V. H. Dale and R. L. Graham. 1988. Indices of landscape pattern. Landscape Ecology 1 (3):153–162.

Patrick, M. J. and W. N. Ellery. 2007. Plant community and landscape patterns of a floodplain wetland in Maputaland, Northern KwaZulu-Natal, South Africa. *African Journal of Ecology* 45 (2):175–183.

Raftery, A. E., D. Madigan and J. A. Hoeting. 1997. Bayesian model averaging for linear regression models. *Journal of the American Statistical Association* 92 (437):179–191.

Roosjen, P.P.J.,, B. Brede, J. M. Suomalainen, H. M. Bartholomeus, L. Kooistra and J.G.P.W. Clevers. 2018. Improved estimation of leaf area index and leaf chlorophyll content of a potato crop using multi-angle spectral data—Potential of unmanned aerial vehicle imagery. *International Journal of Applied Earth Observation and Geoinformation* 66:14–26.

Thome, K. J. S. F. Biggar and H. J. Choi. 2004. Vicarious calibration of Terra ASTER, MISR, and MODIS. *Proceedings of SPIE* 5542: 290–299.

Uuemaa, E., M. Antrop, J. Roosaare, R. Marja and Ü Mander. 2009. Landscape metrics and indices: An overview of their use in landscape research. *Living Reviews in Landscape Research* 3:1.

Wei, S. and H. Fang,. 2016. Estimation of canopy clumping index from MISR and MODIS sensors using the normalized difference hotspot and darkspot (NDHD) method: The influence of BRDF models and solar zenith angle. *Remote Sensing of Environment* 187:476–491.

Wu, C. and A. T. Murray. 2003. Estimating impervious surface distribution by spectral mixture analysis. *Remote Sensing of Environment* 84 (4):493–505.

Wu, S., J. Ren, Z. Chen, W. Jin, X. Liu, H. Li, H. Pan and W. Guo. 2018. Influence of reconstruction scale, spatial resolution and pixel spatial relationships on the sub-pixel mapping accuracy of a double-calculated spatial attraction model. *Remote Sensing of Environment* 210:345–361.

Zhang, Y., G. M. Foody, F. Ling, X. Li, Y. Ge, Y. Du and P. M. Atkinson. 2018. Spatial-temporal fraction map fusion with multi-scale remotely sensed images. *Remote Sensing of Environment* 213:162–181.

Zhao, J., Y. Wang, H. Zhang, Z. Zhang, X. Guo, S. Yu and W. Du. 2016. Spatially and temporally continuous LAI datasets based on the mixed pixel decomposition method. *SpringerPlus* 5:516.

WHO'S WHO IN ASPRS

BOARD OF DIRECTORS

BOARD OFFICERS

President
Thomas Jordan, Ph.D.
University of Georgia

President-Elect
Jeff Lovin
Woolpert

Vice President
Jason M. Stoker, Ph.D
U.S. Geological Survey

Past President
Anne Hillyer, CP
Bonneville Power Administration (USDOE)

Treasurer
Stewart Walker, Ph.D.

Secretary
Roberta E. Lenczowski

BOARD MEMBERS

Sustaining Members Council – 2019
Chair: Joe Cantz
Vice Chair: TBA
www.asprs.org/About-Us/Sustaining-Members-Council.html

Early-Career Professionals Council – 2020
Chair: Peng Fu
Vice Chair: TBA

Region Officers Council – 2021
Chair: Lorraine B. Amenda, PLS, CP
Vice Chair: Demetrio Zourarakas

Student Advisory Council – 2020
Chair: Victoria Scholl
Vice Chair: TBA
http://www.asprs.org/Students/Student-Advisory-Council.html

Technical Division Directors Council – 2020
Chair: John McCombs
Vice Chair: Bandana Kar, Ph.D.

TECHNICAL DIVISION OFFICERS

Geographic Information Systems Division – 2021
Director: Xan Fredericks
Assistant Director: Denise G. Theunissen
www.asprs.org/Divisions/GIS-Division.html

Lidar Division – 2020
Director: Amar K. Nayegandhi, CP, CMS
Assistant Director: Joshua Nimetz, CMS
www.asprs.org/Divisions/Lidar-Division.html

Photogrammetric Applications Division – 2020
Director: Paul C. Bresnahan
Assistant Director: Kurt Rogers
www.asprs.org/Divisions/Photogrammetric-Applications-Division.html

Primary Data Acquisition Division – 2021
Director: Jon Christopherson
Assistant Director: J. Chris Ogier
www.asprs.org/Divisions/Primary-Data-Aquisition-Division.html

Professional Practice Division – 2022
Director: Harold W. Rempel, III, CP
Assistant Director: TBA
www.asprs.org/Divisions/Professional-Practice-Division.html

Remote Sensing Applications Division – 2020
Director: David W. Kreighbaum
Assistant Director: Raechel A. White, Ph.D.
www.asprs.org/Divisions/Remote-Sensing-Applications-Division.html

Unmanned Autonomous Systems (UAS) – 2020
Director: Benjamin Vander Jagt, Ph.D.
Assistant Director: Megan Miller, Ph.D.

REGION PRESIDENTS

Alaska Region
David Parret
http://www.asprsalaska.org/

Cascadia Region
TBA
http://columbia.asprs.org/CRR/

Central New York Region
John Boland, C.P.
http://www.esf.edu/asprs/

Eastern Great Lakes Region
Edward Kunz, GISP
http://egl.asprs.org/

Florida Region
Erin McCormick
http://florida.asprs.org/

Heartland Region
Paul Manley
http://heartland.asprs.org/

Intermountain Region
TBA
http://asprsintermountain.weebly.com/

Mid-South Region
Dr. David Hughes
https://www.asprs.org/all-regions/mid-south.html

New England Region
TBA
http://neweng.asprs.org/

North Atlantic Region
Richard W. Carlson, Jr., P.L.S., C.P.
http://natlantic.asprs.org/

Pacific Southwest Region
Riadh Munjy, Ph.D.
https://pswasprs.org/

Potomac Region
Jackie Carr
http://www.asprspotomac.org/

Rocky Mountain Region
Jeffrey M. Young
http://www.asprs-rmr.org/

Western Great Lakes Region
Kirk Contrucci, CP
http://wgl.asprs.org/

Self-Calibration of the Stereo Vision System of the Chang'e-4 Lunar Rover Based on the Points and Lines Combined Adjustment

Shuo Zhang, Yang Jia, Song Peng, Bo Wen, Youqing Ma, Chen Qi, Bing Sima, and Shaochuang Liu

Abstract

The stereo vision system is the special engineering measurement instrument of the Chang'e-4 lunar rover. It is composed of the Navigation Camera (NavCam) and the Mast Mechanism (MasMec). An improved self-calibration method for the stereo vision system of the Chang'e-4 lunar rover is proposed. The method consists of two parts: the NavCam's self-calibration and the MasMec's self-calibration. A combined adjustment based on the points and lines is proposed. The baseline constraint of the NavCam is considered. The self-calibration model of the MasMec is established based on the product-of-exponentials formula. Finally, the premission laboratory calibration and the on-site calibration are carried out. The laboratory calibration shows that the proposed approach has high accuracy. The checkpoint with a distance of about 2.7 m to the left NavCam has a point error of about 4 mm. Finally, the proposed approach is applied in the on-site calibration.

Introduction

The Chang'e-4 is the world's first spacecraft to soft-land on the far side of the Moon. The Chang'e-4 lunar prober is composed of the relay satellite, the lander, and the lunar rover. The lander-rover system successfully landed on the Von Karman impact crater at 10:26 A.M. (GMT+08:00) on 3 January 2019. The design life of the Chang'e-4 lunar rover is 90 days. It can drive over rocks up to 20 cm high and across a 25-cm-deep pit and can travel up to 200 miles per hour. The inertial measurement unit (IMU) is used to measure the position and attitude of the lunar rover.

The stereo vision system is an important engineering measurement instrument for the lunar rover. Many tasks rely on the stereo vision system, including camera localization, terrain reconstruction, and path programming. The stereo vision system of the Chang'e-4 lunar rover is composed of the Navigation Camera (NavCam) and the Mast Mechanism (MasMec). The NavCam belongs to the engineering camera. It is composed of the left NavCam and the right NavCam. The NavCam and the MasMec on the rover are shown in Figure 1. The parameters of the NavCam are given in Table 1. The image-matching strategy is shown in Figure 2.

Shuo Zhang, Youqing Ma, Bing Sima, and Shaochuang Liu are with the Aerospace Information Research Institute, Chinese Academy of Sciences, North of No. 20, DaTun Road, ChaoYang District, Beijing, China (liusc@radi.ac.cn).

Yang Jia, Song Peng, and Bo Wen are with the China Academy of Space Technology, No. 104, YouYi Road, HaiDian District, Beijing, China.

Chen Qi is with the School of Geodesy and Geomatics, Wuhan University, No. 129, LuoYu Road, HongShan District, Wuhan, China.

Table 1. Parameters of the NavCam. These are factory default.

Parameters	NavCam
Focal length, mm	16.5
Array size, pixel	1024 × 1024
Field of view, °	45 × 45
Baseline length, mm	280
Color or panchromatic	panchromatic
Pixel size, μm	13

The stereo vision system should be calibrated before use. The purpose of calibration is to obtain the parameters of the stereo vision system accurately. In the laboratory, we can accurately estimate the parameters of the stereo vision system by laying out the control field and using high-precision measuring instruments. But the parameters will change after rocket launch, orbital transfer, soft landing, and long-term on-site operation. Furthermore, a lack of texture, no control point, and no high-precision measuring instrument are characteristic of the lunar environment. Therefore, the on-site calibration of the stereo vision system of the lunar rover is an important and challenging issue.

Related Work

The traditional photogrammetry is based on feature points. However, the combined adjustment of the multi-source data has become one of the most important developments in photogrammetry. Zhang *et al.* (2008) proposed a photogrammetric model of lines and curves. This approach can incorporate physical feature points, straight lines, circles, and linear curves. The combined adjustment is proposed to correct the misregistration between the laser altimetry data of the Mars Orbiter Laser Altimeter and the high-resolution images of the Mars Orbiter Camera (Yoon and Shan 2005). The combined adjustment approach to integrate multi-source and multi-resolution satellite imagery (ZY-3, SPOT-7, Pleiades-1, Cartosat-1, and Worldview-1) for improved geo-positioning accuracy without the use of ground control points is proposed (Tang *et al.* 2016). The combined block adjustment approach to integrate multiple strips of the Chinese Chang'e-2 imagery and NASA's Lunar Reconnaissance Orbiter Laser Altimeter data for precision lunar topographic model is proposed (Wu *et al.* 2014). The asymmetric reweighting method is proposed to model the distribution of the errors correctly for the combined bundle adjustment of oblique images (Xie *et al.* 2016). The combined adjustment with linear array and frame array imagery is established (Zhang *et al.* 2013).

Photogrammetric Engineering & Remote Sensing
Vol. 86, No. 3, March 2020, pp. 169–176.
0099-1112/20/169–176

doi: 10.14358/PERS.86.3.169

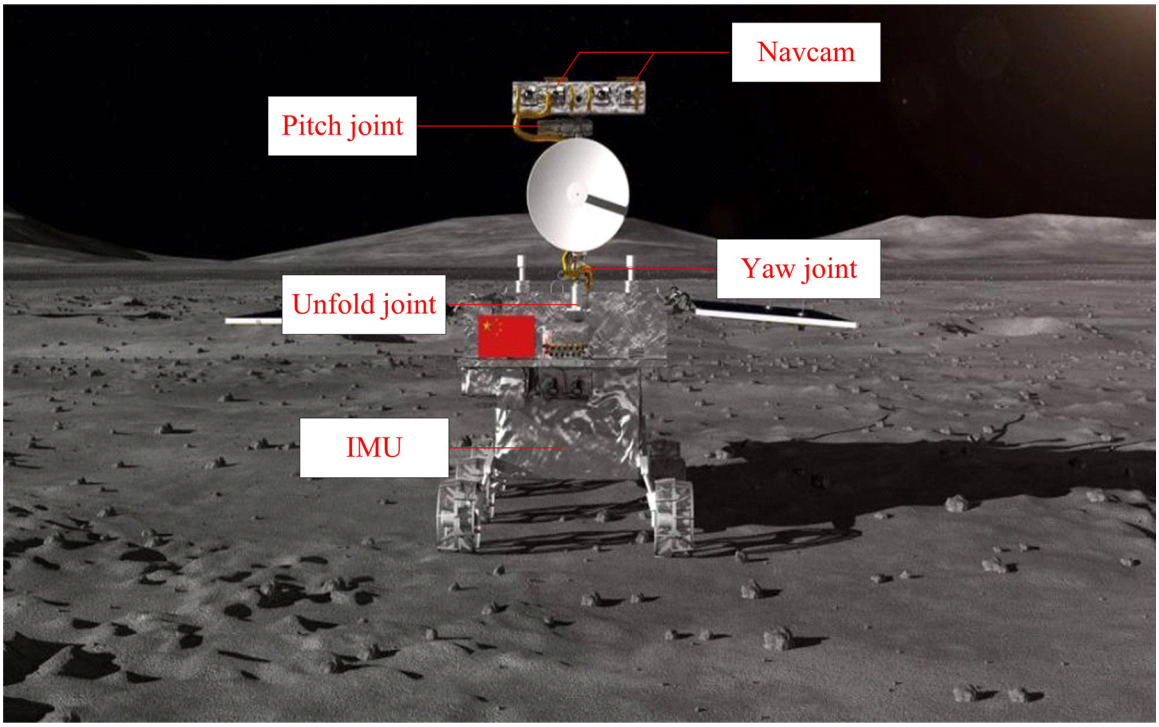

Figure 1. The NavCam and the MasMec. The NavCam is installed on the Pan-Tilt. The Pan-Tilt is connected to the MasMec. The MasMec is connected to the top plate of the lunar rover. The MasMec is made up of three revolute joints: the unfold joint, the yaw joint, and the pitch joint. The MasMec can drive the NavCam to photograph with any pose. The yaw joint can rotate from −180º to +180º. The pitch joint can rotate from −70º to +80º. The unfold joint can rotate from −90º to +70º. The IMU is installed in the inside of the lunar rover.

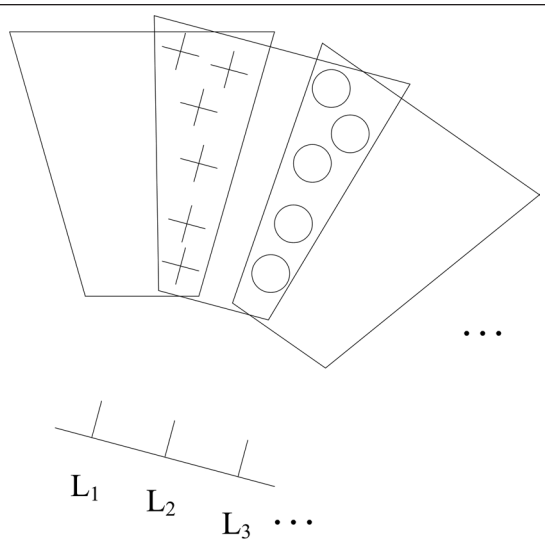

Figure 2. Image-matching strategy. The left sequence images are matched first, then the right sequence images. The left sequence images are taken as the example in figure. L_1 is the first image in the left sequence images, and L_2 is the second image in the left sequence images. The cross (×) stands for the overlapping region between L_1 and L_2, and the circle (○) stands for the overlapping region between L_2 and L_3. The overlapping ratio between the two images is 30%.

The improved on-site calibration method is proposed based on the on-site calibration method of the Chang'e-3 lunar rover (Zhang *et al.* 2017). The improved method is practical for use in the Chang'e-4 lunar rover. The improvements are as follows:

1. The lines on the lunar rover are added in the calibration model. The combined adjustment is proposed based on the feature points on the lunar terrain and the lines on the lunar rover. The improvement increases the number of observations in the feature-poor lunar environment. The points and lines can occupy the field of view of the NavCam uniformly.
2. The baseline constraint is considered. Baseline constraints can enhance the stability of the calibration in the lunar environment without control points.
3. The improved method does not require any control points. This makes the on-site calibration not limited by the inter-visibility between the lunar rover and the lander; see the method in Zhang *et al.* (2017).

On-Site Calibration Model

Coordinate Systems

The following coordinate systems are used in the method. All these coordinate systems are right-handed. The coordinate systems and their relations are shown in Figure 3.

Image Plane Coordinate System (IP System)

The IP system is used to define the image coordinates of the feature points and the feature lines. One is defined on the left NavCam image, and another is defined on the right NavCam image. The origin *o* is in the upper left corner of the first pixel. The *x*-axis points to the right, and the *y*-axis points down.

Camera Coordinate System (CC System)
The CC system is used to describe the elements of the exterior orientation (EO) of the images. One is defined on the left NavCam, and another is defined on the right NavCam. The origin O_C is in the camera projection center. The X_C-axis points to the right, the Y_C-axis points down, and the Z_C-axis points to the front.

Rover Body Coordinate System (RB System)
The RB system is used to describe the position and attitude of the lunar rover. All measurement results are unified in the RB system. The origin O_R is in the geometric center of the structure baseplate of the lunar rover. The X_R-axis points to the front, the Y_R-axis points to the right, and the Z_R-axis points down.

Cube Mirror Coordinate System (CM System)
The cube mirror is a glass cube block. The crosshair is engraved on its +Z surface. It is used mainly to aim during the NavCam's installation. The cube mirror is mounted on the top of the left and the top of the right NavCam. Therefore, there are two CM systems. One is defined on the left cube mirror, and another is defined on the right cube mirror. The origin O_M is in the cube center. The X_M-axis points to the right, the Y_M-axis points down, and the Z_M-axis points to the front.

Work Flow of the Method

The on-site calibration approach includes two parts: the NavCam's calibration and the MasMec's calibration. The work flow of the method is shown in Figure 4.

The first step, the combined adjustment based on the points and lines, is proposed. At the same time, the baseline constraint of the NavCam is considered. Then the improved interior orientation (IO) elements and the EO elements are estimated based on the NavCam's calibration. The IO elements include principal point (x_0, y_0), principal distance (f_x, f_y), radial distortion (k_1, k_2), and tangential distortion (p_1, p_2). The EO elements include transitional elements (X_S, Y_S, Z_S) and angle elements (φ, ω, κ). The EO elements are specified in relation to the CC system and the RB system.

The second step, the MasMec calibration model, is proposed based on the POE formula (Chen *et al.* 2014). The improved kinematic parameters of the MasMec are estimated. The kinematic parameters are (ω_{1i}, ω_{2i}, ω_{3i}, v_{1i}, v_{2i}, v_{3i}), where i = 1, 2, 3 represents the unfold joint, the yaw joint, and the pitch joint. The (ω_{1i}, ω_{2i}, ω_{3i}) is the directional unit vector of the ith joint axis in the RB system. This vector has no physical unit. The (v_{1i}, v_{2i}, v_{3i}) is the position of the ith joint axis in the RB system. The unit of this vector is millimeters. Because the EO elements of the left NavCam are the input for the MasMec model, the IO and EO elements are not the final result of the processing chain in Figure 4.

NavCam Model

Points-Based Calibration Model
The lunar terrain is one of the photographic targets of the NavCam. The feature points on the lunar terrain are used to establish the NavCam's calibration model. This model is established based on the bundle adjustment (Wang 1979). It consists of the following four steps:

1. Note the automatically matched the corresponding image points. First, the sequence images of the left NavCam are matched. Then the sequence images of the right NavCam are matched. (It does not match the left and the right views of the stereo image.) The scale-invariant feature transform algorithm is used to match the adjacent images (Lowe 2004). The random sample consensus algorithm is used to eliminate the mismatch points (Bolles and Fischler 1981).

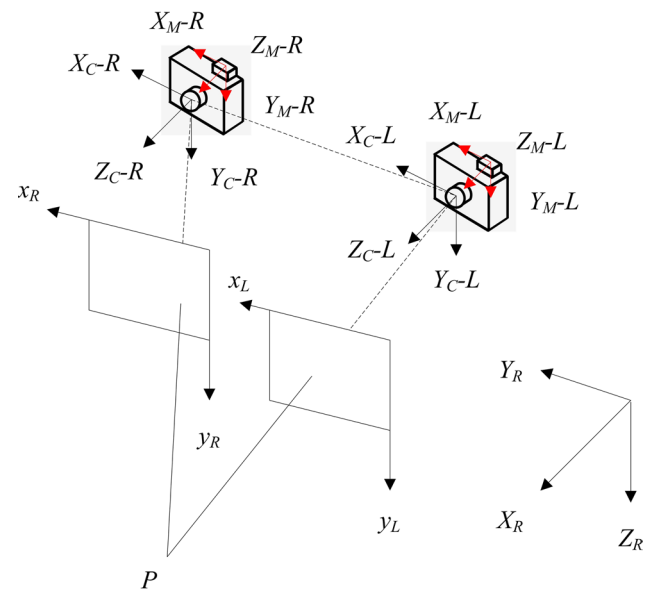

Figure 3. Coordinate systems and their relations: o_L-x_Ly_L and o_R-x_Ry_R are the left IP system and the right IP system. respectively; O_C-L-X_C-LY_C-LZ_C-L and O_C-R-X_C-RY_C-RZ_C-R are the left CC system and the right CC system, respectively; O_M-L-X_M-LY_M-LZ_M-L and O_M-R-X_M-RY_M-RZ_M-R are the left CM system and the right CM system, respectively; and O_R-$X_RY_RZ_R$ is the RB system.

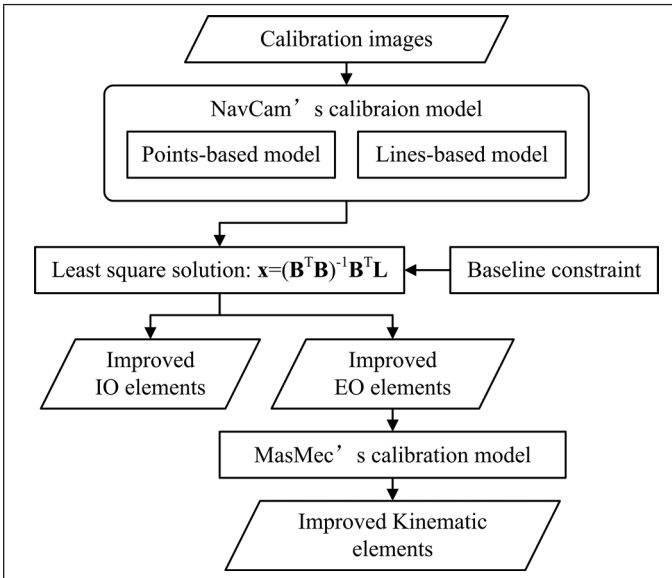

Figure 4. Work flow of the method.

2. Determine relative orientation. The relative orientation is determined by aligning the images and estimating the EO elements between the adjacent images. The factory value of the NavCam is used as the initial value of the IO parameters. The initial values of the EO elements are estimated based on the MasMec model (see the section "MasMec Model"). The EO parameters are determined in relation to the CC system and the RB system.
3. Calculate model connection in the strip aerial triangulation. The model connection is calculated using the 3D coordinates (X, Y, Z) of all matched points.
4. Estimate the bundle adjustment. The bundle adjustment is estimated using the improved IO elements of the NavCam,

the improved EO elements of every image, and the improved 3D coordinates of all matched points in the RB system. The observation equation is given as

$$\begin{cases} x - x_0 - \Delta x = -f_x \dfrac{a_1(X - X_S) + b_1(Y - Y_S) + c_1(Z - Z_S)}{a_3(X - X_S) + b_3(Y - Y_S) + c_3(Z - Z_S)} \\ y - y_0 - \Delta y = -f_y \dfrac{a_2(X - X_S) + b_2(Y - Y_S) + c_2(Z - Z_S)}{a_3(X - X_S) + b_3(Y - Y_S) + c_3(Z - Z_S)} \end{cases}. \quad (1)$$

Line-Based Calibration Model

The lines on the lunar rover are valuable in the sparsely controlled lunar environment. The lines on the lunar rover and the solar array are used to estimate the vanishing points (see Figure 7). The vanishing points are used to calibrate the camera. The vanishing points approach was once used to calibrate the camera in architectural situations (Grammatikopoulos *et al.* 2007). Then the vanishing points approach was developed to calibrate the roadside camera in traffic situations (You and Zheng 2016). The trajectory of the cloud movement is used to estimate the vanishing points. Then the calibration approach based on the cloud motion is proposed (Jacobs *et al.* 2013).

The line-based calibration model consists the following three steps:

1. Estimate the lines. The Canny algorithm is used to estimate the lines (Canny 1986). The split-and-merge algorithm is used to fit the line segments (Borges and Aldon 2000).
2. Estimate the vanishing points. The relationship between the lines and the vanishing points is formulated (Van Den Heuvel 1998).
3. Construct the calibration model based on the vanishing points. Vanishing points are not the destination. They are the bridge for the lines and the IO and EO elements. The relationship between the vanishing points and the IO and EO elements is established according to Xie *et al.* (2004). The relationship between the vanishing points along the *XYZ* axis and the IO and EO parameters is given as

$$\begin{cases} x_{X_\infty} = f\cot\varphi\sec\omega\cot\kappa - f\tan\omega\sin\kappa \\ y_{X_\infty} = -f\cot\varphi\sec\omega\sin\kappa - f\tan\omega\cos\kappa \\ x_{Y_\infty} = f\cot\omega\sin\kappa \\ y_{Y_\infty} = f\cot\omega\cos\kappa \\ x_{Z_\infty} = -f\tan\varphi\sec\omega\cos\kappa - f\tan\omega\sin\kappa \\ y_{Z_\infty} = f\tan\varphi\sec\omega\sin\kappa - f\tan\omega\cos\kappa \end{cases}. \quad (2)$$

Baseline Constraint

The NavCam has a pair of stereo cameras. It is installed with a fixed baseline length. The baseline length refers to the *X* component of the EO parameters from the right NavCam to the left NavCam. The fixed relationship between the left NavCam and the right NavCam is used to establish the baseline constraint. There is the following restrictive constraint between the left NavCam and the right NavCam (Zheng *et al.* 2012):

$$\begin{pmatrix} \left[\left(\mathbf{R}_l^T\mathbf{R}_r\right)_i - \left(\mathbf{R}_l^T\mathbf{R}_r\right)_j\right]_{12} \\ \left[\left(\mathbf{R}_l^T\mathbf{R}_r\right)_i - \left(\mathbf{R}_l^T\mathbf{R}_r\right)_j\right]_{13} \\ \left[\left(\mathbf{R}_l^T\mathbf{R}_r\right)_i - \left(\mathbf{R}_l^T\mathbf{R}_r\right)_j\right]_{23} \\ \left[\mathbf{R}_l^T(\mathbf{T}_r - \mathbf{T}_l)\right]_i - \left[\mathbf{R}_l^T(\mathbf{T}_r - \mathbf{T}_l)\right]_j \end{pmatrix} = 0. \quad (3)$$

The rotation matrices **R** and the translation vectors **T** are given in relation to the CC frame and the RB frame. $\mathbf{R}_l$ is the rotation matrix of the left NavCam, $\mathbf{R}_r$ is the rotation matrix of the right NavCam, $\mathbf{T}_l$ is the translational vector of the left NavCam, and $\mathbf{T}_r$ is the translational vector of the right NavCam. The subscripts *i* and *j* stand for the *i*th stereopair and the *j*th stereopair, respectively. The subscript numbers stand for the column and the row. For example, the number 12 stands for the first row and the second column of the rotation matrix **R**.

Weighted Least-Squares Optimization

Finally, the weighted least-squares optimization is used to estimate the IO and EO elements. The error equation is given as

$$\begin{cases} \min \quad \mathbf{v}^T\mathbf{P}\mathbf{v} \\ \mathbf{v}_1 = \mathbf{B}\mathbf{x} - \mathbf{l}_1 \quad \mathbf{P}_1 \quad BA \\ \mathbf{v}_2 = \mathbf{A}\mathbf{x} - \mathbf{l}_2 \quad \mathbf{P}_2 \quad VP \\ \mathbf{C}\mathbf{x} - \mathbf{G} = 0 \quad BC \end{cases} \quad (4)$$

where *BA* is the error equation of the bundle adjustment, $\mathbf{P}_1$ is the corresponding weight matrix, *VP* is the error equation of the vanishing points calibration model, and $\mathbf{P}_2$ is the corresponding weight matrix. The weight matrix **P** is determined based on the posteriori weight estimate (Li 1982). *BC* is the error equation of the baseline constraint, $(\mathbf{v}_1, \mathbf{v}_2)^T$ is the correction vector of the image points, $(\mathbf{l}_1, \mathbf{l}_2, \mathbf{G})^T$ are the residual error vectors, **x** is the correction vector of the IO and EO elements, and **A**, **B**, and the **C** are the corresponding coefficient matrix. Finally, Equation 4 is solved based on the conventional least-squares approach.

MasMec Model

The POE formula is used to establish the kinematic calibration model of the MasMec (Park 1994). The POE formula can effectively overcome the singularity problem of the classical Denavit–Hartenberg model when the adjacent joints are close to parallel (He *et al.* 2010). It is proved that the POE formula has continuity, integrity, and minimality (Chen *et al.* 2014). The determined EO parameters of the left NavCam related to the MasMec are shown in Figure 5.

The kinematic model of the MasMec based on the POE formula is given as

$$\mathbf{g} = e^{\hat{\xi}_1 q_1} \cdot e^{\hat{\xi}_2 q_2} \cdot e^{\hat{\xi}_3 q_3} \cdot \mathbf{g}_{CR}(0), \quad (5)$$

where $e^{\hat{\xi}_1 q_1}$ stands for the exponent formula of the unfold joint, $e^{\hat{\xi}_2 q_2}$ stands for the exponent formula of the yaw joint, and $e^{\hat{\xi}_3 q_3}$ stands for the exponent formula of the pitch joint. The explicit expression of $e^{\hat{\xi} q}$ is given in He *et al.* (2010); $\hat{\xi}$ is the twist of the joint, q_1 is the joint variable, and $\mathbf{g}_{CR}(0)$ is the transformation matrix from the CC system to the RB system when the MasMec is in the zero position. The zero position means that the rotation angle of all three joints is zero.

Equation 5 is expanded by the first-order Taylor series. Then $\mathbf{g}^{-1}$ is multiplied in both sides of the expanded equation. Finally, the kinematic error model (Equation 6) is obtained, and only the twist error $\delta\xi$ is considered:

$$\delta\mathbf{g}\mathbf{g}^{-1} = \left(\frac{\partial\mathbf{g}}{\partial\xi}\delta\xi\right)\mathbf{g}^{-1}. \quad (6)$$

The weighted least-squares optimization is used to estimate the kinematic parameters. The nominal kinematic parameter is taken as the initial value.

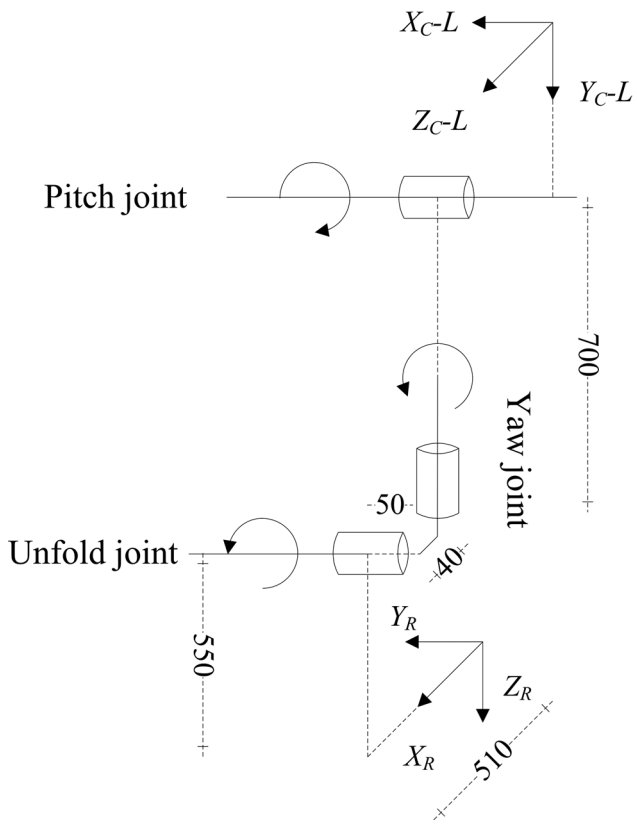

Figure 5. Relation between the determined EO parameters of the left NavCam and the MasMec: O_C-L-X_C-LY_C-LZ_C-L is the left CC system, and O_R-$X_RY_RZ_R$ is the RB system. All three joints are described in the RB system. The sizes given in the figure are the design values. The unit of the sizes is millimeters. The arrow arc stands for the positive rotation of the joint.

Experiments

Premission Calibration

The premission calibration is conducted in the Lunar Environment Simulation Laboratory. The core area is a rectangular region. The size of the core area is 20 × 20 m. Volcanic ash is filled in the core area and simulates the lunar soil. A large lamp array is installed on the north wall and simulates the lunar illumination. An industrial crane is used to lift the rover to simulate the one-sixth gravity of the Moon. High-accuracy measurement devices (IGPS, theodolite, laser tracker) are used to measure the key points on the lunar rover.

The NavCam performs sequence imaging. The rotation angle of the unfold joint is 0°. The rotation angle of the yaw joint is from −90° to +90° and shoots one stereopair at 18° intervals. The rotation angle of the pitch joint is −30°. Eleven stereo images are obtained. The measurement values of the rotation angles of all three joints are known. This value is measured by the rotation transformer. The NavCam images are processed according to the proposed method (see the section "NavCam Model"). The tie points are matched between the adjacent images of the sequence images. First, the sequence images of the left NavCam are matched. Then the sequence images of the right NavCam are matched. The 4637 points are matched in the left NavCam images, and the 4284 points are matched in the right NavCam images.

The feature lines on the lunar rover are estimated. The 33 lines are estimated from the left NavCam images, and the 35 lines are estimated from the right NavCam images. Finally, the IO and EO elements of the NavCam can be estimated. The improved IO elements are given in Table 2, and the improved EO elements are given in Table 3.

Table 2. Improved IO elements. The associated cameras are the NavCam. The calibration type is laboratory. RMSE stands for the root-mean-square error; (x_0, y_0) stands for the coordinates of the principal point in the IP system; (f_x, f_y) stands for the principal distance along the x and y axes; k_1 and k_2 are the radial distortion coefficients; and p_1 and p_2 are the tangential distortion coefficients. The unit of the principal point and the focal length is millimeters. The distortion coefficient has no unit.

	Left NavCam		Right NavCam	
Parameters	**Value**	RMSE	**Value**	**MSE**
x_0	6.790105	0.009217	6.585086	0.005577
y_0	6.566679	0.007969	6.559867	0.007332
f_x	16.60829	0.006318	16.69137	0.005057
f_y	16.61011	0.007423	16.68556	0.006318
k_1	−1.786E-08	2.840E-09	−7.812E-09	1.881E-09
k_2	1.870E-14	7.106E-15	1.348E-15	3.429E-15
p_1	−1.053E-06	3.021E-07	−1.080E-06	2.876E-07
p_2	2.105E-07	2.917E-07	5.201E-07	2.694E-07

Table 3. Improved EO elements. The associated cameras are the NavCam. The calibration type is laboratory. The EO parameters are given in relation to the CC system and the CM system. This is because these two systems are relatively fixed. There are two different CM systems: one for the left NavCam and one for the right NavCam (one per camera). (X, Y, Z) are the translation parameters, and $(\varphi, \omega, \kappa)$ are the rotation parameters. The unit of (X, Y, Z) is millimeters. and the unit of $(\varphi, \omega, \kappa)$ is radians.

	Left NavCam		Right NavCam	
Parameters	**Value**	RMSE	**Value**	RMSE
X	31.184	0.114	31.287	0.185
Y	31.806	0.173	31.996	0.209
Z	−3.308	0.323	−4.695	0.403
φ	−0.0016	0.0016	−0.0022	0.0031
ω	0.0007	0.0009	0.0012	0.0015
κ	0.0003	0.0005	0.0003	0.0004

The calibrated EO elements of the left NavCam are taken as the input for the MasMec calibration (see Figure 5). This is because the Tool coordinate system required by the MasMec model is defined as the left CC system. Nominal kinematic parameters use the design value of the MasMec. The improved kinematic parameters of the MasMec are given in Table 4.

Table 4. Improved kinematic parameters. The associated object is the MasMec. The calibration type is laboratory. ω_i stands for the directional unit vector of the ith joint axis in the RB system, and v_i stands for the position of the ith joint axis in the RB system. ω_i has no units, and the unit of v_i is millimeters.

	Unfold Joint		Yaw Joint		Pitch Joint	
Parameters	**Value**	RMSE	**Value**	RMSE	**Value**	RMSE
ω_1	0.003	0.0047	−0.003	0.0027	−0.003	0.0025
ω_2	−0.999	0.0032	0.002	0.0045	0.997	0.0028
ω_3	0.002	0.0029	−1.001	0.0037	0.003	0.003
v_1	−551.658	0.284	57.389	0.362	1248.739	0.265
v_2	0.592	0.260	467.390	0.401	0.735	0.403
v_3	−517.849	0.336	0.628	0.486	469.647	0.338

All the parameters of the stereo vision system are listed in Tables 2–4. The 24 checkpoints are used to verify the accuracy of the points. The checkpoints are measured by theodolite. The measurement accuracy of the checkpoints is superior to 0.1 mm. The checkpoints are shown in Figure 6.

The improved IO and EO parameters are substituted into the forward intersection based on the stereo images (Wang 1979). The approach estimates the 3D coordinate of the checkpoints. Finally, the position error is given in Table 5.

Table 5. Position error. The calibration type is laboratory. The position error is obtained through P_F subtracted from P_T. P_F stands for the 3D coordinates, which are estimated by the forward intersection. P_T stands for the 3D coordinates, which are measured by theodolite. Then the RMSE is calculated for the position error. The unit of the RMSE is millimeters, and the unit of the distance to the left NavCam is meters.

ID	RMSE	Distance to Left NavCam
1	3.933	2.689
2	4.458	2.463
3	5.425	3.955
4	5.812	3.881
5	4.105	3.874
6	3.831	3.812
7	6.706	5.985
8	6.741	5.936
9	7.596	6.303
10	7.261	6.287
11	6.005	7.097
12	6.327	6.991
13	10.470	10.113
14	12.111	10.084
15	13.862	9.676
16	15.612	9.580
17	13.647	9.836
18	17.878	9.622
19	22.750	13.884
20	22.091	13.537
21	30.368	16.295
22	27.194	15.736
23	23.831	15.508
24	26.871	15.721

On-Site Calibration

The proposed method is practical and is used in the on-site calibration of the stereo vision system of the Chang'e-4 lunar rover. First, the surrounding terrain of the landing site is sequence imaged. This is the first detection point after landing. The station name is called Top Station. The lunar rover is still on the top of the lander. The lunar rover and the lander are still not separate.

The sequence images of the Top Station are used for the on-site calibration. The state of the MasMec is as follows. The unfold angle is 0°. The yaw angle is from −180° to +180° and shoots one stereopair at 20° intervals. The pitch angle is −30°. A total of 18 stereopairs are obtained.

The tie points are matched. The 7517 points are matched from the sequence images of the left NavCam. The 6809 points are matched from the sequence images of the right NavCam.

The feature lines on the lunar rover are estimated. The 417 lines are estimated from the sequence images of the left NavCam. The 435 lines are estimated from the sequence images of the right NavCam. A total of 852 lines are estimated. The estimated points and lines are shown in Figure 7. The improved IO elements are given in Table 6. The improved EO elements are given in Table 7. The improved kinematic parameters are given in Table 8.

Table 6. Improved IO elements. The associated cameras is the NavCam. The calibration type is on-site. RMSE stands for root-mean-square error; (x_0, y_0) stands for the coordinates of the principal point in the IP system; and (f_x, f_y) stands for the principal distance along the x and y axes. k_1 and k_2 are the radial distortion coefficients, and p_1 and p_2 are the tangential distortion coefficients. The unit of the principal point and the focal length is millimeters, and the distortion coefficient has no unit.

	Left NavCam		Right NavCam	
Parameters	Value	RMSE	Value	RMSE
x_0	6.756578	0.007696	6.631196	0.007124
y_0	6.595018	0.007189	6.568668	0.007007
f_x	16.58892	0.005486	16.71426	0.005668
f_y	16.60362	0.006188	16.71005	0.005551
k_1	−1.483E-08	−1.786E-08	−6.253E-09	−7.812E-09
k_2	1.701E-14	1.871E-14	1.385E-15	1.348E-15
p_1	−3.490E-06	−1.054E-06	−3.827E-06	−1.081E-06
p_2	−7.767E-07	−2.106E-07	−9.781E-07	−5.202E-07

Table 7. Improved EO elements. The associated cameras are the NavCam. The calibration type is on-site. (X, Y, Z) are the translation parameters, and $(\varphi, \omega, \kappa)$ are the rotation parameters. The unit of (X, Y, Z) is millimeters, and the unit of $(\varphi, \omega, \kappa)$ is radians.

	Left NavCam		Right NavCam	
Parameters	Value	RMSE	Value	RMSE
X	31.382	0.155	31.932	0.203
Y	31.593	0.190	31.763	0.225
Z	−8.165	0.383	−4.660	0.379
φ	−0.0019	0.0011	−0.0015	0.0026
ω	0.0005	0.0015	0.0008	0.0020
κ	0.0006	0.0007	0.0007	0.0009

Table 8. Improved kinematic parameters. The associated object is the unfold joint, the yaw joint, and the pitch joint of the MasMec. The calibration type is on-site. ω_i stands for the directional unit vector of the ith joint axis in the RB system, and v_i stands for the position of the ith joint axis in the RB system. ω_i has no units, and the unit of v_i is millimeters.

	Unfold Joint		Yaw Joint		Pitch Joint	
Parameters	Value	RMSE	Value	RMSE	Value	RMSE
ω_1	0.005	0.0037	−0.004	0.0033	−0.003	0.0031
ω_2	−1.002	0.0041	0.001	0.0049	1.001	0.0028
ω_3	0.003	0.0035	−0.997	0.0032	−0.002	0.0032
v_1	−557.875	0.196	55.839	0.316	1243.840	0.299
v_2	0.624	0.225	461.330	0.275	0.801	0.353
v_3	−524.764	0.293	0.784	0.304	461.593	0.264

Discussion

The RMSE values are small both for the laboratory result (Tables 2–4) and for the on-site result (Tables 6–8). It can reflect that the proposed method has the high theoretical accuracy. There are small changes in the parameters by comparing the on-site results (Tables 6–8) with the laboratory results (Tables 2–4). Overall, the EO elements are very similar except for the Z value of the left NavCam. The change comes from the difference of the points used and the lines in the two different environments (lunar and laboratory). The Z-direction's model points of the on-site calibration are not evenly distributed. The $+Z$ is the direction of the optical axis of the NavCam.

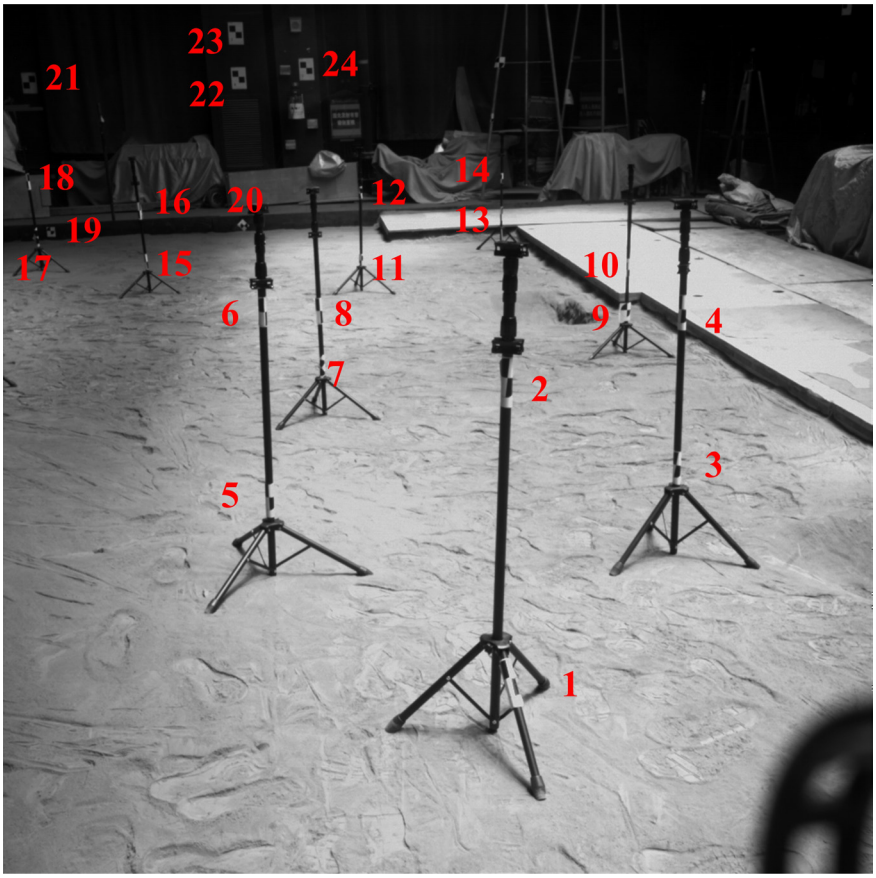

Figure 6. Checkpoints. The calibration type is laboratory. The checkpoints in the image are not used for the laboratory calibration.

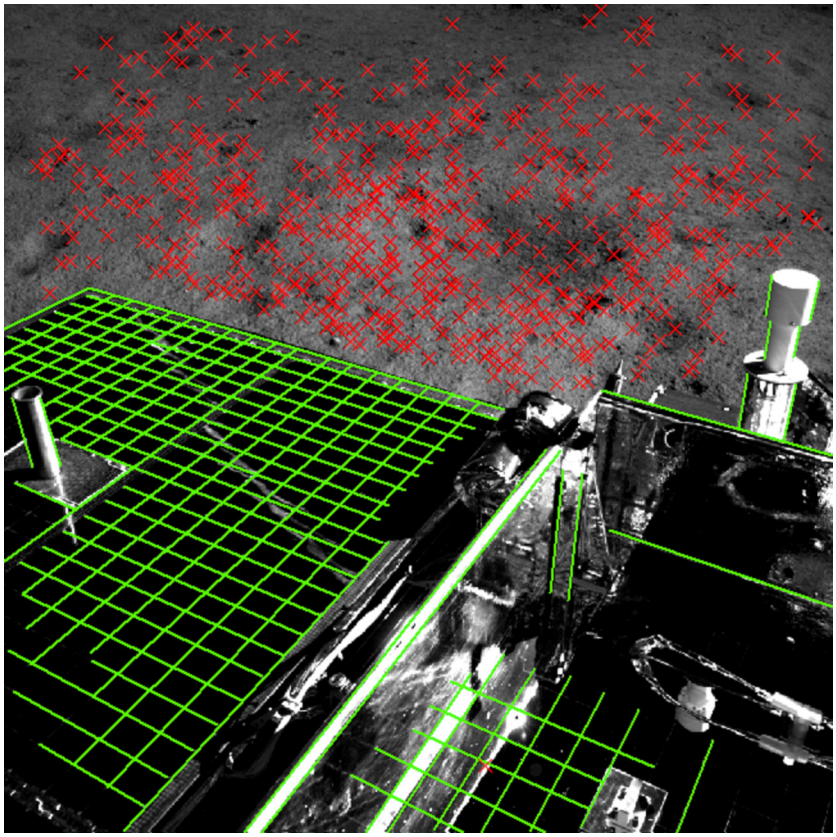

Figure 7. Points and lines are estimated from the sequence images of left NavCam. The location of the lunar rover is on top of the lander. The tie points are matched from stereopair L_1–L_2 and stereopair L_2–L_3. The lines are estimated from the image L_2. L stands for the sequence images of the left NavCam. The subscript *i* stands for the *i*th image of the sequence images of the left NavCam.

The difference does not have a serious impact. Because the IO and EO parameters are estimated as a whole, they are globally optimal.

The point accuracy is the most direct way to judge the accuracy of the calibration approach. Table 5 provides a detailed and accurate overview of the point accuracy. It can be seen from Table 5 that the checkpoints with a distance of about 2.7 m to the left NavCam have a point error of about 4 mm. The measurement accuracy of the control point is 0.1 mm. The achieved accuracy in the laboratory calibration proved that the proposed approach can meet the precision requirements of the on-site calibration.

Conclusions

The improved on-site calibration method for the stereo vision system of the Chang'e-4 lunar rover is proposed. The improvements are as follows. First, the lines on the lunar rover are used. Second, the NavCam's baseline constraint is considered. Third, the improved method does not require any control points.

The premission laboratory calibration and the on-site calibration are carried out. The following three conclusions are drawn by comparing the on-site results with the laboratory result. First, the proposed method has high accuracy. The laboratory calibration shows that the checkpoints with a distance of about 2.7 m to the left NavCam have a point error of about 4 mm. Second, the EO elements are very similar except for the Z value of the left NavCam. The change comes from the difference of the points used and the lines in two different environments (lunar and laboratory). The Z-direction's model points of the on-site calibration are not evenly distributed. The $+Z$ is the direction of the optical axis of the NavCam. The difference does not have the serious impact. Because the IO and EO parameters are estimated as a whole, they are the globally optimal.

China plans to send a Mars rover in 2020. The Mars rover will also be equipped with the stereo vision system. The proposed self-calibration approach not only is used on the Chang'e-4 lunar rover but also can be used on the self-calibration of the stereo vision system of the Mars rover.

Acknowledgments

The author thanks Prof. Shaochuang Liu for the idea's support and the article's modification support. The author thanks Prof. Yang Jia for the mission support and the article's modification support. The author thanks Song Peng and Bo Wen for the technical support. The author thanks Youqing Ma, Chen Qi, and Bing Sima for the experiment help and data processing help.

References

Bolles, R. C. and A. M. Fischler. (1981. A RANSAC-based approach to model fitting and its application to finding cylinders in range data. *International Joint Conference on Artificial Intelligence* 1981:637–643.

Borges, G. A. and M. L. Aldon. 2000. A split-and-merge segmentation algorithm for line extraction in 2d range images. *Proceedings of the 15th International Conference on Pattern Recognition* 1:441–444.

Canny, J. 1986. A computational approach to edge detection. *IEEE Transactions on Pattern Analysis and Machine Intelligence* 6:679–698.

Chen, G., H. Wang and Z. Lin. 2014. Determination of the identifiable parameters in robot calibration based on the POE formula. *IEEE Transactions on Robotics* 30 (5):1066–1077.

Grammatikopoulos, L., G. Karras and E. Petsa. 2007. An automatic approach for camera calibration from vanishing points. *ISPRS Journal of Photogrammetry and Remote Sensing* 62 (1):64–76.

He, R., Y. Zhao, S. Yang and S. Yang. 2010. Kinematic-parameter identification for serial-robot calibration based on POE formula. *IEEE Transactions on Robotics* 26 (3):411–423.

Jacobs, N., M. T. Islam and S. Workman. 2013. Cloud motion as a calibration cue. *Proceedings of the IEEE Conference on Computer Vision and Pattern Recognition* 2013:1344–1351.

Li, D. 1982. A posteriori weight estimation in self-calibrating bundle block adjustment. *Geomatics and Information Science of Wuhan University* 1:16–24.

Lowe, G. 2004. Distinctive image features from scale-invariant keypoints. *International Journal of Computer Vision* 60 (2):91–110.

Park, F. C. 1994. Computational aspects of the product-of-exponentials formula for robot kinematics. *IEEE Transactions on Automatic Control* 39 (3):643–647.

Tang, S., B. Wu and Q. Zhu. 2016. Combined adjustment of multi-resolution satellite imagery for improved geo-positioning accuracy. *ISPRS Journal of Photogrammetry and Remote Sensing* 114:125–136.

Van Den Heuvel, F. A. 1998. Vanishing point detection for architectural photogrammetry. *International Archives of Photogrammetry and Remote Sensing* 32:652–659.

Wang, Z. Z. 1979. *The Principle of Photogrammetry*. Beijing: China Surveying and Mapping.

Wu, B., H. Hu and J. Guo. 2014. Integration of Chang'e-2 imagery and LRO laser altimeter data with a combined block adjustment for precision lunar topographic modeling. *Earth and Planetary Science Letters* 391:1–15.

Xie, L., H. Hu, J. Wang, Q. Zhu and M. Chen. 2016. An asymmetric re-weighting method for the precision combined bundle adjustment of aerial oblique images. *ISPRS Journal of Photogrammetry and Remote Sensing* 117:92–107.

Xie, W., Z. Zhang and J. Zhang. 2004. Multi-image based camera calibration without control points. *International Archives of the Remote Sensing and Spatial Information Sciences: XXXV Congress* 2004:36–41.

Yoon, J. S. and J. Shan. 2005. Combined adjustment of MOC stereo imagery and MOLA altimetry data. *Photogrammetric Engineering and Remote Sensing* 71 (10):1179–1186.

You, X. and Y. Zheng. 2016. An accurate and practical calibration method for roadside camera using two vanishing points. *Neurocomputing* 204:222–230.

Zhang, S., S. Liu, Y. Ma, C. Qi, H. Ma and H. Yang. 2017. Self calibration of the stereo vision system of the Chang'e-3 lunar rover based on the bundle block adjustment. *ISPRS Journal of Photogrammetry and Remote Sensing* 128:287–297.

Zhang, Y., L. Lin, M. Zheng and J. Xiong. 2013. Combined bundle block adjustment with spaceborne linear array and airborne frame array imagery. *The Photogrammetric Record* 28 (142):162–177.

Zhang, Z., Y. Zhang, J. Zhang and H. Zhang. 2008. Photogrammetric modeling of linear features with generalized point photogrammetry. *Photogrammetric Engineering and Remote Sensing* 74 (9):1119–1127.

Zheng, S., R. Huang, B. Guo and K. Hu. 2012. Stereo-camera calibration with restrictive constraints. *Cehui Xuebao/Acta Geodaetica et Cartographica Sinica* 41:877–885.

Reducing Shadow Effects on the Co-Registration of Aerial Image Pairs

Matthew Plummer, Douglas Stow, Emanuel Storey, Lloyd Coulter, Nicholas Zamora, and Andrew Loerch

Abstract

*Image registration is an important preprocessing step prior to detecting changes using multi-temporal image data, which is increasingly accomplished using automated methods. In high spatial resolution imagery, shadows represent a major source of illumination variation, which can reduce the performance of automated registration routines. This study evaluates the statistical relationship between shadow presence and image registration accuracy, and whether masking and normalizing shadows leads to improved automatic registration results. Eighty-eight bitemporal aerial image pairs were co-registered using software called Scale Invariant Features Transform (*SIFT*) and Random Sample Consensus (*RANSAC*) Alignment (*SARA*). Co-registration accuracy was assessed at different levels of shadow coverage and shadow movement within the images. The primary outcomes of this study are (1) the amount of shadow in a multi-temporal image pair is correlated with the accuracy/success of automatic co-registration; (2) masking out shadows prior to match point select does not improve the success of image-to-image co-registration; and (3) normalizing or brightening shadows can help match point routines find more match points and therefore improve performance of automatic co-registration. Normalizing shadows via a standard linear correction provided the most reliable co-registration results in image pairs containing substantial amounts of relative shadow movement, but had minimal effect for pairs with stationary shadows.*

Introduction

Rapid acquisition and delivery of information regarding land surface features that are altered by natural hazards can improve the strategies and reaction times of emergency responders (Stow *et al.* 2018). Visual and automated analyses of aerial imagery captured before and after a hazard provide a basis for detecting changes and evaluating the condition of features deemed critical to emergency response teams. When assessing many sites and large amounts of image data, time-expensive visual interpretation alone may be inadequate for generating critical information in a timely manner, necessitating automated or semiautomated image processing approaches. While image preprocessing and automated image change detection software are valuable, further work is required to integrate such technology in a reliable manner for time-sensitive image processing applications (Lippitt and Stow 2015).

Matthew Plummer is with Critigen, Inc., Jacksonville, FL and was with the Department of Geography, San Diego State University, 5500 Campanile Drive, San Diego, CA 92182 (mattjplummer@gmail.com).

Douglas Stow, Emanuel Storey, Lloyd Coulter, and Andrew Loerch are with the Department of Geography, San Diego State University, 5500 Campanile Drive, San Diego, CA 92182 (stow@mail.sdsu.edu).

Nicholas Zamora is with Leidos, 10260 Campus Point Drive, M/S C5, San Diego, CA 92121 (zamora.nick@gmail.com).

Accurate image registration is a critical component of image-based change detection (Zitová and Flusser 2003). Registration has traditionally been achieved by manual point selection, but automated methods are now common practice due to recent computational advances and are especially relevant in time-sensitive applications. Automatic image registration is commonly based on the scale-invariant feature transform (SIFT) algorithm, which identifies corresponding geometric features among images for use as control points (Lowe 2004). SIFT software is readily available, imbedded in many image registration routines, does not require training, and has been effective in our testing towards the development of automated, near-real-time image registration.

Automatic registration is challenging in the presence of relief displacement, especially in more geometrically complex urban areas (Suri and Reinartz 2010; Han *et al.* 2014). An image acquisition technique called repeat station imaging (RSI), (formerly referred to as frame center matching), is useful in minimizing effects of variable view geometry and relief displacement (Coulter, Stow, and Baer 2003; Stow, Coulter, and Baer 2003). RSI utilizes global navigation satellites to navigate aerial platforms and trigger image capture at nearly the same position and altitude in the sky as a previously acquired image (Coulter *et al.* 2015). By acquiring images in this manner, the effects of parallax feature displacement on registration accuracy is greatly minimized (Stow *et al.* 2016). While using RSI, in combination with automated routines like SIFT, greatly increase the ease of preprocessing multi-temporal imagery, the effectiveness of automatic registration algorithms can be reduced greatly by radiometric variability within scenes. Key sources of radiometric variability in multi-temporal aerial imagery include dynamic atmospheric conditions, changes in solar orientation, camera exposure settings, and shadows that change in extent or location through time (transient shadows).

Transient shadows in multi-temporal image sets can lead to errors in image registration and subsequent change detection (Benediktsson and Sveinsson 1997; Wang *et al.* 1999). Differences in illumination from shadowing can yield image brightness differences that are similar to or greater than those associated with changes of interest. Shadows can also cause time varying lighting effects on texture, or a suppressed range of digital number values in shadowed areas (Shu and Freeman 1990; Dare 2005; Liu and Yamazaki 2012). Detecting shadows in optical remotely sensed imagery is a prevalent topic in remote sensing literature (Adeline *et al.* 2013). Shadow detection methods can be categorized as four types: model-based, physics-based, machine learning, and property-based methods (Adeline *et al.* 2013). The binary classification of pixels in shadowed areas is the basis for shadow removal via masking or normalization. Masking refers to the process of removing (i.e., setting pixels' digital numbers to zero or black)

Photogrammetric Engineering & Remote Sensing
Vol. 86, No. 4, April 2020, pp. 177–186.
0099-1112/20/177–186

doi: 10.14358/PERS.86.4.177

pixels classified as shadows, whereas normalization refers to augmenting the digital number (DN) values of shadowed pixels to approximate directly illuminated conditions (Li, Zhang, and Shen 2014).

Shadow normalization is generally achieved by: (1) gamma correction, (2) histogram matching, or (3) linear correction (Sarabandi *et al.* 2004; Ma, Qin, and Shen 2008; Lorenzi, Melgani, and Mercier 2012). Several studies have demonstrated superior results from linear adjustment (Shu and Freeman 1990; Storey *et al.* 2017). Shadow normalization is most successful when sunlit pixels of a certain material are used to brighten shadowed pixels of the same material, and less successful when material reflectance differences are not considered (Sarabandi *et al.* 2004; Dare 2005; Lorenzi, Melgani, and Mercier 2012). However, image classification to identify material types typically involves substantial computational time and often subjective human interventions, both of which are inconsistent with time-sensitive application requirements.

Most literature on shadow effects in remote sensing is focused on the development and improvement of shadow detection techniques (Adeline *et al.* 2013). Research on shadow normalization has demonstrated its utility for enhancing change detection accuracy, but has not addressed the specific topic of improving image registration by shadow removal or normalization (Ma, Qin, and Shen 2008; Liu and Yamazaki 2012; Li, Zhang, and Shen 2014). Several image registration studies suggest that time-varying illumination effects degrade registration performance (Wong and Clausi 2007; Arévalo and González 2008; Han *et al.* 2014), but these were focused generally on the advancement of point matching routines and not on shadow effects. The possibility that *a priori* shadow removal could enhance registration accuracy is implicitly recognized but not explored in the extant literature.

More advanced algorithms for identifying prospective match points and performing image co-registration continue to be developed, for example those that utilize deep learning approaches such as convolutional neural networks (Wei *et al.* 2018). Deep learning and other machine learning approaches require extensive pretraining based on hundreds to thousands of images. Several proceedings papers have appeared recently in the computer vision literature, reporting advances in match point selection with deep learning routines, based on two or three standardized, ground photo testing data sets (e.g., Liberty and Yosemite) (Balntas, Tang, and Mikolajczyk 2015; Balntas *et al.* 2016; Fischer, Dosovitskiy, and Brox 2014; Mitra 2017). While promising, presently there are no suitable trained networks based on aerial image data, and no attempts to date to explore whether deep learning routines are more robust for selecting match points between bitemporal image pairs containing transient shadows.

A clearer understanding of the relation between shadows and image registration accuracy is likely to enhance the utility of remote sensing in near-real-time applications. If shadow presence in imagery is detrimental enough to automatic registration routines to render them unreliable and inaccurate, subsequent change detection results would be of equally limited utility. Thus, if reducing shadow effects from multi-temporal imagery lead to a significant enough improvement in registration accuracy, it could enable near-real-time change detection applications. The objectives of this study are to characterize the negative effects of shadows on automatic image registration of bitemporal image pairs (i.e., co-registration), and assess approaches for reducing these effects on the co-registration accuracy of aerial RSI pairs. Using aerial image data from two urban study sites in San Diego County, Calif., we establish a direct connection between shadow presence between scenes and co-registration accuracy. We also evaluate the benefits of masking and of normalizing shadows before co-registration to improve the co-registration accuracy of aerial image pairs.

The following research questions and subquestions are addressed in this paper:

1. Is there a statistically significant relationship between extent and movement of shadows and the co-registration accuracy of aerial image pairs?
   a. What is the relationship between the total amount of shadow present between images in a pair and their co-registration accuracy?
   b. What is the relationship between the amount of shadow movement over time between images in a pair and their co-registration accuracy?
2. How do masking and normalizing shadows in aerial image pairs prior to co-registration affect image co-registration accuracy?

Methods

Data

A set of color (red-green-blue or RGB) aerial images was used for testing shadow effects on image co-registration. This data set includes a total of 99 individual 8-bit TIFF images from two sites in San Diego County: Palomar Medical Center and a multi-family residential area in the northeast portion of the City of San Diego, hereafter referred to as the Hospital and MFR sites, respectively. All images were captured using a Nikon D800 digital single lens reflex camera (36 megapixel) with a 50 mm lens, at an average height of 670 m above ground level (H_{AGL}), making the ground sampling distance (GSD) approximately 0.08 m for each image. Each site is covered by multiple image frames that serve as the baseline or *time-1* (*t-1*) images for evaluating the co-registration process. At both sites, the *t-1* images include separate frames that were captured in a series along a flight line, and therefore exhibit varying scene composition. The *time*-2 (*t-2*) images that were later registered to the *t-1* images were acquired using the RSI approach (Coulter *et al.* 2015; Stow *et al.* 2016). All *t-1* images from both sites were captured in the morning, while the associated *t-2* images were taken at either a similar time of the morning (i.e., *similar-time* pairs) or during the afternoon (i.e., AM-PM pairs). The *t-2* images in similar-time pairs were all captured on the same day as the *t-1* images, whereas some of the *t-2* images in AM-PM pairs were acquired two weeks later than the *t-1* images. The 99 total images comprise 88 image pairs, as each *t-1* image was used in combination with several *t-2* images. Of the 88 image pairs, 28 are similar-time pairs, while 60 are AM-PM pairs. Site specific details of image coverage are summarized in Table 1.

Table 1. Information on the number of similar-time, AM-PM, and total image pairs at each site, along with the height above ground level (H_{AGL}) at which the images were taken and their GSD.

Site	*t-1* images	*t-2* images (similar time/afternoon)	Image pairs (similar time/ AM-PM)	H_{AGL}	GSD
Hospital	6	8 (3/5)	48 (18/30)	670 m	0.08 m
MFR	5	8 (2/6)	48 (10/30)	670 m	0.08 m

Image Co-Registration Procedure and Accuracy Metrics

Automated co-registration of aerial image pairs was performed using a SIFT and Random Sample Consensus Alignment (SARA). The SARA procedure utilizes the SIFT routine to find points in the two images and evaluate their similarity based on their 128-value descriptors (Lowe 2004). Points that are likely matches form an initial set of control points, from

which the RANSAC algorithm finds a model that accurately fits as many points as possible while excluding any outliers (Fischler and Bolles 1981). The remaining points represent the final set of control points, 10% of which we used for accuracy testing (i.e., test points), while the remaining 90% were used in image transformation. We applied a second-order polynomial warping transformation, which has been shown to be effective for aerial frame RSI pairs (Stow *et al.* 2016).

We first quantified co-registration accuracy as positional offset between *t-1* and *t-2* using the root-mean-square error (RMSE) of the distance (in pixels) between points in the SARA test point sets. Radiometric differences associated with the image pairs were quantified using root-mean-square difference (RMSD) of the pixel intensity values, as derived from the hue-saturation-intensity transform of the co-registered images. As the image pairs were acquired using RSI under consistent exposure settings and represent mainly unchanged scenes (from *t-1* to *t-2*), pixel-level radiometric variations are principally a consequence of misregistration and incomplete radiometric normalization of differential illumination. RMSD thus serves as a second metric for quantifying co-registration accuracy; it also provides a measure for quantifying relative differences in misregistration among image pairs in a manner that is directly relevant to change detection (Stow 1996).

Because shadows have the potential to reduce the number of discoverable control points that enhance co-registration performance, we also used *image co-registration success rate* and *number of test points used* as metrics of co-registration performance. If during the co-registration of an image pair with SARA an insufficient number of control points (< 7) are selected, or an excessive RMSE value (> 50 pixels) is yielded, the co-registration process is aborted and a failure to produce a solution is reported. The threshold of 50 pixels RMSE was selected after experimentation, to ensure that a sufficient sample size of AM-PM image pairs was successfully co-registered by SARA to enable meaningful statistical assessment. Our success rate metric was thus defined as the number of image pairs successfully co-registered (i.e., solutions produced by SARA) divided by the total number of image pairs attempted to be co-registered. The SARA procedure also reports the number of test points used to calculate each image pair's RMSE statistic, which can serve as a proxy for the number of control points used to co-register each pair (e.g., roughly nine times the number of test points). Thus, we tabulated the number of test points used, where a greater number of test points (and therefore control points) typically results in more accurate co-registration results.

In order to generate more representative co-registration accuracy metrics by reducing bias from outliers and chance solutions, all image pairs were run ten times through SARA. Due to this, the RMSE, RMSD, and number of test points metrics reported are averages across the ten iterations of SARA. As a result of using ten iterations, any image pair that did not successfully co-register in all ten iterations was considered a failure in the image co-registration success rate metric. Most image pairs that did not successfully co-register in all ten attempts typically yielded RMSE and RMSD values which tended to vary erratically and were unreliable. For that reason, the constraint of an image pair needing to successfully co-register in all ten iterations of SARA is reasonable.

Shadow Detection

We implemented a model-based approach (Adeline *et al.* 2013) to detect and classify shadows in multi-temporal image pairs. We first applied spectral transformations from the images. The Q and Y components of the Luma-in-phase-quadrature (YIQ) color space were shown by Tsai (2006) to outperform other transformations for shadow detection. The YIQ color space is derived from the RGB model (Equation 1):

$$\begin{bmatrix} Y \\ I \\ Q \end{bmatrix} = \begin{bmatrix} 0.299 & 0.587 & 0.114 \\ 0.596 & -0.275 & -0.321 \\ 0.212 & -0.523 & 0.311 \end{bmatrix} \begin{bmatrix} R \\ G \\ B \end{bmatrix} \tag{1}$$

Shadow detection was based on the ratio of Q and Y (Q/Y), which is generally sensitive to the spectral and radiometric properties of shadows. Following the procedure in Tsai (2006), a (Q + 1)/(Y + 1) ratio image was obtained and rescaled to the range of values in [0, 255]. Shadows were classified in the rescaled ratio image based on Otsu's automated histogram thresholding method, which is used widely to discriminate shadowed and nonshadowed pixels (Otsu 1979; Tsai 2006). However, in our preliminary shadow classification trials, it was apparent that the method described above led to substantial errors of commission. To remedy this, we multiplied the unscaled $(Q + 1)/(Y + 1)$ ratio images by the ratio of the blue band and intensity values (B/I) derived from the original RGB images to form a modified ratio image. For this application, intensity (I) was defined as a panchromatic average value (Equation 2):

$$I = \frac{R + G + B}{3} \tag{2}$$

We used the ratio of blue to intensity (B/I) because previous work has shown it is also sensitive to shadows, owing to their inherently low radiance coupled with a high proportion of blue light from diffuse illumination (Liu and Yamazaki 2012; Storey *et al.* 2017). We rescaled the modified ratio image in the range of values in [0, 255] and applied Otsu's thresholding method to the resulting image. The improvement of shadow detection accuracy by using the modified ratio images over the original ratio images is visually obvious.

Shadow Normalization

Three different shadow normalization procedures were tested in a comparative manner to determine their effects on image co-registration. Image brightness data was obtained from areas adjacent to the shadows, which are the most likely to contain materials of similar reflectance. The technique we used for sampling the brightness distribution of nearby pixels emulates that of Tsai (2006). Contiguous spatial clusters of pixels classified as shadows were grouped to form unique shadow regions (i.e., objects). Morphological dilation was then used to create buffer zones to a distance of 10 pixels surrounding each shadow region. The shadow regions were normalized individually using the DN values derived from its surrounding buffer zone on a band-by-band basis. Unlike the methodology in Tsai (2006), only shadow regions composed of greater than 25 pixels were normalized. This was based on an assumption that small shadow regions would not have a substantial effect on the ability of SIFT to find quality control points. Ignoring small (i.e., < 25 pixels) shadow regions also aided in reducing the computational load of the normalization routines. A threshold of 25 pixels was arrived at through testing and visual inspection of the shadow regions found in the image data. Additionally, the largest shadow region excluded using this threshold cannot affect more than ten percent of the pixels in a SIFT descriptor window.

The first shadow normalization method we tested is a linear correction approach based on Equation 3 (Sarabandi *et al.* 2004; Liu and Yamazaki 2012):

$$DN_r = (DN_i - \mu_S) \times (\sigma_{NS} / \sigma_S) + \mu_{NS} \tag{3}$$

where DN_i is the input value of a pixel in a given shadow region, μ_S and μ_{NS} represent the mean values of a shadow region

and its buffer zone (respectively), σ_S and σ_{NS} represent standard deviation values of a shadow region and its buffer zone (respectively), and DN_r is the resultant normalized pixel value.

We also tested a gamma correction method (Equation 4) which considers shadows as a multiplicative noise source (Sarabandi *et al.* 2004; Wan, King, and Li 2012; Jain and Khunteta 2017):

$$DN_r = (DN_i)^{1/\gamma} \tag{4}$$

where DN_i is the input value of a pixel in a given shadow region, DN_r is the resultant normalized pixel value, and γ is the gamma parameter (slope of the regression line in log-log space) relating the brightness of the shadow region to its corresponding buffer zone. In practice, DN values should be normalized according to radiometric resolution, so in the case of 8-bit images the above equation can be written as:

$$\frac{DN_r}{255} = \left(\frac{DN_i}{255}\right)^{1/\gamma} \tag{5}$$

The mean values of a given shadow region and its buffer zone are used to calculate the γ parameter used to normalize shadow pixels.

Histogram matching was selected as a third shadow normalization approach. This is a nonlinear, frequency-based matching approach used to shift the brightness distribution of a subject image to approximate that of a reference image that has been used successfully in shadow normalization (Cox, Roy, and Hingorani 1995; Helmer and Ruefenacht 2005; Tsai 2006). In our application, the histogram of each shadow region is shifted to match its corresponding buffer zone in an automated fashion.

Assessing Effects of Shadow Presence on Co-Registration Accuracy

To evaluate the influence of shadows on image co-registration quality, we compared areal proportions of transient and total shadow in the co-registered image pairs with their RMSE and RMSD values. The total amount of shadow in an image pair is defined as the proportion of image pixels in the overlapping area of its two images that are shadowed in the *t-1* and/or *t-2* image. The amount of transient shadow in an image pair is defined as the proportion of image pixels in the overlapping area of its two images that are shadowed in *only one of the t-1 or t-2 images*. As with RMSE and RMSD values, the amount of total and transient shadow in each pair is characterized as the average from ten iterations of SARA. Shadow pixels were excluded from the calculations of the RMSD metric in order to prevent them from biasing the RMSD values. Including shadow pixels, specifically ones affected by transient shadow, would introduce radiometric biases when attempting to understand co-registration effects on RMSD. We also evaluated the effects of shadow presence on co-registration accuracy by comparing RMSE, RMSD, co-registration success rate, and number of test points used for RMSE calculation of similar-time and AM-PM pairs.

To qualitatively assess the influence of shadows on image co-registration performance, we examined images depicting the location of control points used to co-register the similar-time and AM-PM image pairs. These images (i.e., *control point images*) are generated for the *t-1* and *t-2* images in every successfully co-registered pair. The control point images provide more context to the quantitative co-registration metrics by revealing how control point selection in SARA differs with varying amounts of total shadow and transient shadow between images.

Effects of Shadow Masking and Normalization on Co-Registration Accuracy

We applied each shadow normalization technique to a representative subset of 22 images (similar-time as well as AM-PM pairs) in order to identify which approach provided the most accurate co-registration results. The optimal normalization method was applied to the total set of images in order to compile three versions of every image pair: original, shadow-masked, and shadow-normalized. We computed co-registration RMSE values, RMSD values, co-registration success rate, and number of test points used for the RMSE calculations and compared these metrics for the three versions of image pairs. Shadow pixels were excluded from the RMSD calculations of shadow-masked and original image pairs. This was not possible for RMSD values obtained for the shadow-normalized image pairs because the normalized shadow pixels could not be reliably identified again through an alternative method. Other methods for partially remedying this discrepancy biased the SARA control point selection process. Thus, shadow pixels were not excluded in the RMSD calculations of the shadow-normalized image pairs.

The effects of shadow masking and normalization on co-registration performance were qualitatively examined by comparing the control point images of shadow-masked and shadow-normalized image pairs to those of the original image pairs. The control point images augment the results of the quantitative co-registration metrics by illustrating how masking and normalizing shadows affect the control point selection in SARA.

Results

Effects of Shadows on Co-Registration Accuracy

Scatterplots and regression results of RMSE and RMSD as a function of total shadow and transient shadow for each original image pair for the Hospital and MFR sites are shown in Figure 1 and Figure 2, respectively.

Co-registration accuracy of image pairs at both sites is significantly and inversely related to the amount of total shadow and transient shadow. The RMSE and RMSD values of co-registered pairs in both datasets are more strongly associated with transient shadow than total shadow, with the exception of average RMSE in the Hospital dataset. Both total and transient shadow present in the co-registered pairs are more strongly related to RMSD than they are to RMSE. The strengths of correlation of RMSE and RMSD with total shadow and transient shadow are generally higher for the Hospital dataset than for the MFR dataset. A potential reason for this is the anchoring effect of the similar-time pairs for the Hospital site on those variable distributions.

The influence of shadow presence on co-registration performance was also assessed by comparing the co-registration results of the similar-time and AM-PM image pairs for both sites as shown in Table 2. For both sites, RMSE and RMSD values of AM-PM pairs are at least two times greater than those of the similar-time pairs. The substantially lower average number of test points and lower co-registration success rates also signify lower image co-registration performance among AM-PM pairs relative to similar-time pairs.

Table 2. Co-registration performance for the Hospital and MFR sites.

Site	Image pair type	RMSE	RMSD	Number of points	Success rate
Hospital	Similar time	2.46	13.35	96.61	100%
Hospital	AM-PM	7.43	29.81	3.30	90%
MFR	Similar time	2.14	15.16	66.56	100%
MFR	AM-PM	6.45	32.89	2.75	73.3%

RMSE is given in units of pixels and RMSD is given in units of intensity.

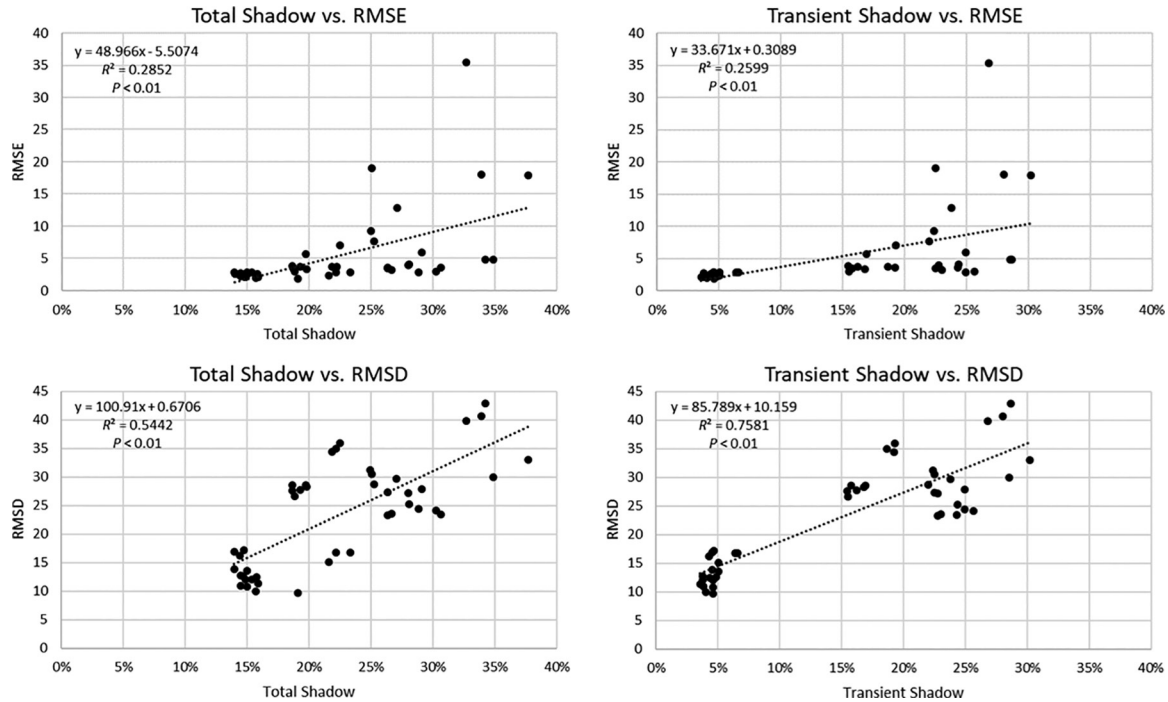

Figure 1. Total shadow and transient shadow versus RMSE and RMSD at the Hospital site. RMSE is given in units of pixels and RMSD in units of intensity.

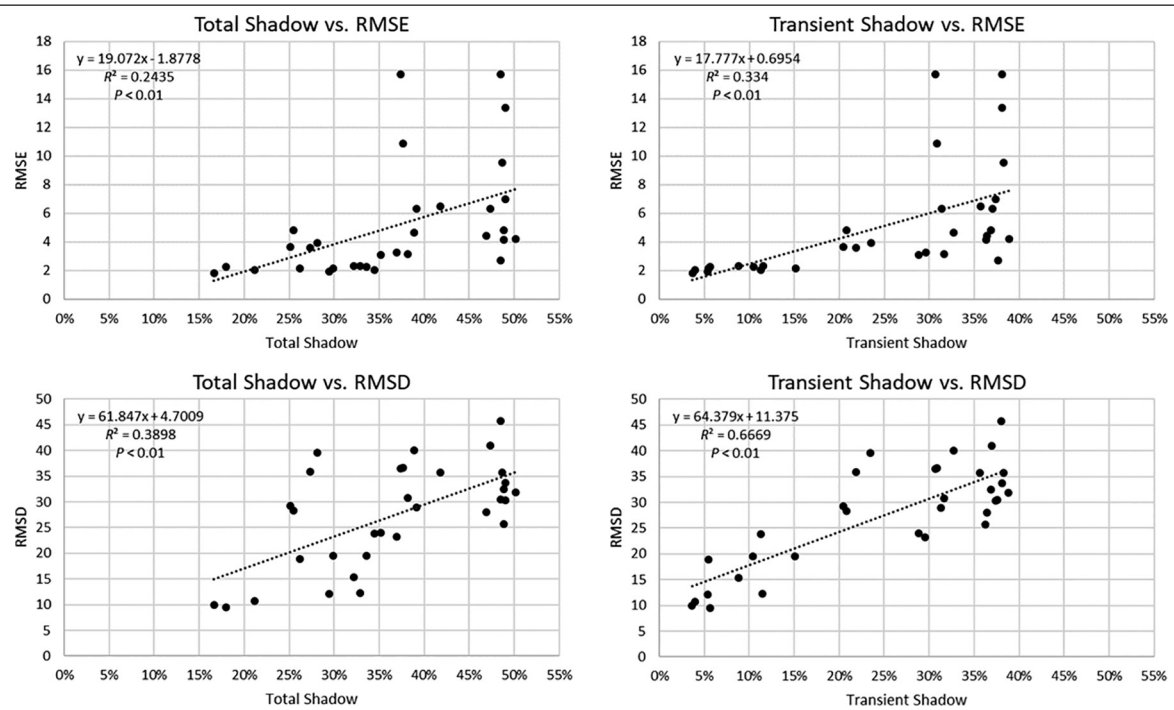

Figure 2. Total shadow and transient shadow versus RMSE and RMSD at the MFR site. RMSE is given in units of pixels and RMSD in units of intensity.

Subsets of the control point images for a similar-time and an AM-PM pair depicting the same scene at the MFR site are shown in Figure 3. The distribution of and differences in control points found within these subsets are representative of what we observed for the majority of the co-registered pairs of both sites.

As illustrated in the insets of Figure 3a and 3b, SARA frequently used control points located in shadow regions to co-register the similar-time image pairs at both sites. A closer inspection showed that those control points had the same positional accuracy as control points located in fully illuminated areas. Control points were also evenly dispersed throughout the scenes of all of the similar-time image pairs at both sites. In other words, the percentage of control points located in shadow (and fully illuminated) regions was roughly equivalent to the areal proportion of shadow

Figure 3. Subsets showing the location of control points found in the *t-1* and *t-2* images of an original similar-time and AM-PM image pair at the MFR site. The red dots represent control points used to co-register the image pairs. Green dots represent test points used to calculate the RMSE of the image pair.

(and fully illuminated) pixels in similar-time pairs. As first indicated by the test points metric used, AM-PM image pairs were co-registered using a much smaller number of control points than the similar-time pairs. The control point images also reveal that control points used in AM-PM image pairs were much less likely to be located in shadow regions. Of those control points, the majority were not affected by transient shadow (i.e., their SIFT descriptors did not contain transient shadow pixels), such as the control point located in the top right corner of Figure 3c and 3d. As such, they have the same high positional accuracy of points located in fully illuminated areas. The rare control points that were located in transient shadow regions have positional offsets that vary but do not exceed five or six pixels.

Effectiveness of Masking and Normalization on Increasing Co-Registration Accuracy

The RMSE, RMSD, number of test points, and co-registration success rate values of the shadow-normalized image pairs for each normalization approach are listed in Table 3. For the similar-time image pairs, the three shadow normalization approaches yielded similar average RMSE values, with linear correction yielding the lowest co-registration error (2.29) relative to gamma correction and histogram matching (2.32 and 2.35, respectively). Gamma correction yielded the lowest average RMSD value (14.60), while linear correction and histogram matching yielded similar average RMSD values (17.00 and 17.49, respectively). Co-registration performances in terms of the average number of points used for the RMSE calculations were not substantially different among the shadow normalization approaches. Linear correction, gamma correction, and histogram matching yielding point totals of 70.55, 68.91, and 70.36, respectively for similar-time pairs.

Table 3. Co-registration metrics for shadow-normalized image pairs using linear correction, gamma correction, and histogram matching for the Hospital and MFR sites.

Image pair type	Normalization method	RMSE	RMSD	Number of points	Success rate
Similar time	Linear correction	2.29	17.00	70.55	100%
	Gamma correction	2.32	14.60	70.36	100%
	Histogram matching	2.35	17.49	68.91	100%
MFR	Linear correction	3.57	33.51	5.36	100%
	Gamma correction	6.18	31.47	4.45	100%
	Histogram matching	4.00	33.50	5.36	100%

Considering both similar-time and AM-PM image pairs, the RMSE and number of test point metrics favor linear correction, while the RMSD metric favors gamma correction. Based on a visual assessment of the images that had been subjected

Figure 4. Original image, shadow mask, and results of shadow normalization via linear correction for an image for the Hospital and MFR sites. Hospital site: (a) original, (c) detected shadows in turquoise, and (e) linear correction shadow normalization product. MFR site: (b) original, (d) shadow mask, and (f) linear correction normalization product.

to both normalization methods, however, linear correction provides superior contrast and acuity (restoration of detail) compared to gamma correction. Shadow pixels of gamma corrected images yielded average intensity values that resemble global (scene-wide) intensity, and thus yielded the lowest average RMSD among the normalization methods. This effect is not necessarily due to more accurate co-registration. Therefore, the linear correction normalization method was selected as the optimal approach and applied to the remainder of image pairs. Examples of the original, shadow mask, and linear correction product for an image at the Hospital site and MFR site are shown in Figure 4.

Co-registration performance based on the original, shadow-masked, and shadow-normalized (via linear correction) image pairs for both sites are shown in Table 4. For similar-time image pairs associated with both sites, neither masking nor

Table 4. Co-registration results of original, shadow-masked, and shadow-normalized image pairs for the Hospital and MFR sites.

Site	Image pair type	Version	RMSE	RMSD	Number of points	Success rate
Hospital	Similar time	Original	2.46	13.35	96.61	100%
		Masked	2.57	17.20	60.44	100%
		Normalized	2.53	15.29	79.34	100%
	AM-PM	Original	7.43	29.81	3.30	90%
		Masked	7.78	35.40	2.33	60%
		Normalized	5.28	32.17	3.83	100%
	Similar time	Original	2.14	15.16	66.56	100%
		Masked	2.27	20.02	38.70	100%
		Normalized	2.38	19.53	49.80	100%
MFR	AM-PM	Original	6.45	32.89	2.75	73.33%
		Masked	9.37	39.40	2.29	23.33%
		Normalized	3.70	34.39	5.66	96.67%

normalizing shadows resulted in higher co-registration performance over the original image pairs according to any of the metrics. Masking shadows did not improve co-registration performance in the AM-PM pairs for either site based on their higher RMSE values, higher RMSD values, lower number of test points used, and substantially lower co-registration success rate compared to the originals. However, normalizing shadows led to a notable improvement in the co-registration of the AM-PM pairs at both sites. With the exception of the RMSD metric, all of the co-registration metrics for the shadow-normalized AM-PM pairs improved over those of the original pairs.

The primary and obvious difference between the control point images for shadow-masked and original image pairs (both similar-time and AM-PM) is the absence of control points located in shadow regions of shadow-masked pairs. Masking shadows also lowered the number of control points selected in fully illuminated regions of similar-time and AM-PM image pairs. The distribution and positional accuracy of control points in fully illuminated regions of shadow-masked and original image pairs are otherwise similar. Examples of the control point images for shadow-masked image pairs were not helpful in illustrating our observations and therefore not included. Figure 5 contains subsets of the control point images for the shadow-normalized (via linear correction) version of the similar-time and AM-PM image pairs depicted in Figure 3. The distribution of, and differences in, control points found within these subsets are representative of what we observed for the majority of the co-registered shadow-normalized pairs of both sites.

Figure 5. Subsets showing the location of control points found in the *t-1* and *t-2* images of a shadow-normalized similar-time and AM-PM image pair at the MFR site. The red dots represent control points used to co-register the image pairs. Green dots represent test points used to calculate the RMSE of the image pair.

How shadow normalization improved co-registration performance of the AM-PM image pairs at both sites is illustrated in the insets of Figure 5c and 5d. Normalizing shadows increased the number of control points selected in both the fully illuminated and shadow regions of AM-PM image pairs. Despite what is depicted in Figure 5a and 5b, shadow normalization actually decreased the number of control points located in fully illuminated and especially shadow regions of similar-time image pairs. For both similar-time and AM-PM image pairs, some control points selected in normalized shadow regions are offset by two or three pixels more than control points within shadow regions of original image pairs. The positional accuracy of control points selected in shadow-normalized and original image pairs are otherwise the same.

Discussion and Conclusion

The results of this study represent the first empirical substantiation of the connection between shadows and automatic image co-registration accuracy. Capturing image pairs using the RSI approach was important for isolating the influence of total and transient shadow on co-registration accuracy by ensuring that images composing each pair had similar viewing geometries. RMSE and RMSD metrics for both sites exhibit significant, negative linear correlation with amounts of total as well as transient shadow. Our findings also indicate that transient shadows are more strongly correlated with reduced co-registration performance than shadows that are stationary in multi-temporal imagery. This differential response results from how shadow movement affects the way control points are recognized in feature space by the SIFT algorithm in SARA. That is, features that remain at a similar intensity through time are more likely to be accepted as control points than features that change in intensity due to transient shadows. This response was shown to be true in practice through the analysis of the control point images. For both study sites, total shadow and transient shadow exhibit a stronger correlation with RMSD than RMSE, suggesting that the influence of pixel-level radiometric variation due to misalignment can be more substantial than geometric misalignment due to shading. This finding also indicates a strong potential influence of misregistration on image-based change detection.

The stark difference between the co-registration performance of similar-time and AM-PM pairs is further evidence of how transient shadows can be detrimental to co-registration performance. The most pronounced difference between the two types of pairs is the dramatically lower number of test points, and therefore control points, used in AM-PM pairs. This is connected to the failure of some AM-PM pairs to co-register which, based on an analysis of SARA output logs, was in most instances due to SARA generating an insufficient number of control points (< 7) to compute a warping transformation. By

visual inspection we found that the number of control points located in and outside of shadow regions of AM-PM pairs decreased, illustrating that the negative effects of shadow movement on co-registration are not limited to just those pixels representing transient shadow. The visual inspection also revealed that control points located in shadow regions have the same high quality and are as likely to be selected as those in fully illuminated areas of similar-time pairs. This further suggests that shadow movement, not shadow presence *per se*, is the main way in which shadows impede accurate co-registration.

Beyond limiting the number of control points selected, transient shadows could also theoretically lead SARA to use inaccurate control points by causing two different image features to appear similar enough in SIFT feature space to be considered the same, or a match. The analysis of the control point images for AM-PM pairs show that this does not occur though. Instead, control points affected by transient shadow were rarely used to co-register AM-PM pairs and even when they were, their positional accuracy was not severely impacted. The low co-registration accuracy of image pairs containing large amounts of transient shadow is therefore primarily attributed to a paucity and uneven distribution of control points, and not the use of inaccurate control points.

Masking shadows did not benefit the co-registration performance of similar-time pairs because it prevented the use of high quality control points that are frequently found in shadow regions. It was also ineffective in improving the co-registration performance of AM-PM pairs because shadow masking does not properly address the problem of transient shadows limiting the number control points selected. Shadow normalization was beneficial to the co-registration of AM-PM pairs at both sites by allowing SARA to find and utilize more control points, in both shadow and fully illuminated regions than was possible in the original AM-PM pairs. Thus, shadow normalization helps to restore the ability of SARA to find reliable control points throughout the images containing substantial shadow movement. The greater number of well-distributed control points that resulted from normalizing shadows in AM-PM pairs appears to outweigh the side effect of lower positional accuracy of some control points in normalized shadow regions. Shadow normalization enhanced co-registration results for the AM-PM pairs of the MFR site more than for the Hospital site. This is likely because more changes in scene features were captured in the AM-PM pairs for the Hospital site due to construction activity. Greater amounts of scene change make it more challenging to find matching scene features through automated methods and therefore fewer control points are selected.

Shadow normalization did not however improve the co-registration performance of similar-time pairs at either site, due primarily to a decrease in the number of control points used in co-registration. This decrease observed in both normalized shadow regions and fully illuminated areas can be explained by the way SIFT initially locates features in image scenes. In short, the control points used in SARA represent image locations that have intensity values that remain the local minimum or maximum through a series of smoothing operations in SIFT. Shadows naturally represent areas that commonly are local minima in our data. By normalizing shadow regions, the locations of local minima and maxima change in the image data. In the case of similar-time image pairs where shadows are mostly stationary, these changes in local minima and maxima appear to restrict the SARA routine's procedure for selecting control points. In addition to a lower number of control points, the higher RMSE and RMSD values of shadow-normalized similar-time pairs could be influenced by the lower positional accuracy of control points located in normalized shadow regions. The lower positional accuracy of those points is likely caused by the high texture of the normalized shadow regions.

Future research should involve testing image pairs associated with a wider range of scene types under varied illumination and shadow conditions. Improvements in shadow detection and normalization techniques are also needed in order to increase the benefit these provide for automatic registration and change detection with bitemporal image pairs affected by transient shadow. If timeliness and automation are not constraints, more computationally intensive shadow detection and normalization routines could be implemented. Even more promising, match point selection algorithms based on deep learning routines could potentially facilitate greater accuracy and timeliness when co-registering bitemporal images affected by transient shadows. The latter will require a major investment in developing pretrained deep learning networks based on an extensive collection of aerial image data sets and interactive labeling of shadow features, as well as robust testing, similar to that implemented in this study.

Acknowledgments

The work was partially funded by the National Science Foundation Directorate of Engineering, Infrastructure Management and Extreme Events (IMEE) program (Grant Number G00010529) and the United States Department of Transportation (USDOT) Office of the Assistant Secretary for Research & Technology (OST-R) Commercial Remote Sensing and Spatial Information Technologies Program (CRS&SI), cooperative agreement # OASRTRS-14-H-UNM. Richard McCreight of NEOS, Ltd. captured aerial imagery utilized for this study.

References

Adeline, K. R. M., M. Chen, X. Briottet, S. K. Pang and N. Paparoditis. 2013. Shadow detection in very high spatial resolution aerial images: A comparative study. *ISPRS Journal of Photogrammetry and Remote Sensing* 80:21–38.

Arévalo, V. and J. González. 2008. An experimental evaluation of non-rigid registration techniques on Quickbird satellite imagery. *International Journal of Remote Sensing* 29 (2):513–527.

Arévalo, V., J. González and G. Ambrosio. 2008. Shadow detection in colour high-resolution satellite images. *International Journal of Remote Sensing* 29 (7):1945–1963.

Balntas, V., L. Tang and K. Mikolajczyk. 2015. Bold-binary online learned descriptor for efficient image matching. In *Proceedings of the IEEE Conference on Computer Vision and Pattern Recognition*, held in Boston, Mass.

Balntas, V., E. Riba, D. Ponsa and K. Mikolajczyk. 2016. Learning local feature descriptors with triplets and shallow convolutional neural networks. In *Proceeding of the British Machine Vision Conference*, held in York, England.

Benediktsson, J. A. and J. R. Sveinsson. 1997. Feature extraction for multisource data classification with artificial neural networks. *International Journal of Remote Sensing* 18 (4):727–740.

Bentoutou, Y., N. Taleb, K. Kpalma and J. Ronsin. 2005. An automatic image registration for applications in remote sensing. *IEEE Transactions on Geoscience and Remote Sensing* 43 (9):2127–2137.

Brown, L. G. 1992. A survey of image registration techniques. *ACM Computing Surveys* 24 (4):325–376.

Coulter, L., D. Stow and S. Baer. 2003. A frame center matching technique for precise registration of multitemporal airborne frame imagery. *IEEE Transactions on Geoscience and Remote Sensing* 41 (11):2436–2444.

Coulter, L., D. Stow, C. Lippitt and G. Fraley. 2015. Repeat station imaging for rapid airborne change detection. In *Time-Sensitive Remote Sensing*, edited by C. Lippitt, D. Stow and L. Coulter, 29–43. New York: Springer Publishers.

Cox, I. J., S. Roy and S. L. Hingorani. 1995. Dynamic histogram warping of image pairs for constant image brightness. Pages 366–369 in *IEEE Proceedings of the International Conference on Image Processing Volume 2*, held in Washington, DC, 23–26 October 1995.

Dai, X. and S. Khorram. 1998. The effects of image misregistration on the accuracy of remotely sensed change detection. *IEEE Transactions on Geoscience and Remote Sensing* 36 (5):1566–1577.

Dare, P. M. 2005. Shadow analysis in high-resolution satellite imagery of urban areas. *Photogrammetric Engineering and Remote Sensing* 71 (2):169–177.

Fischer, P., A. Dosovitskiy and T. Brox. 2014. Descriptor matching with convolutional neural networks: A comparison to SIFT. arXiv: 1405.5769 [cs.CV].

Fischler, M. and R. Bolles. 1981. Random sample consensus: A paradigm for model fitting with applications to image analysis and automated cartography. *Communications of the ACM* 24 (6):381–395.

Han, Y., J. Choi, Y. Byun and Y. Kim. 2014. Parameter optimization for the extraction of matching points between high-resolution multisensor images in urban areas. *IEEE Transactions on Geoscience and Remote Sensing* 52 (9):5612–5621.

Helmer, E. H. and B. Ruefenacht. 2005. Cloud-free satellite image mosaics with regression trees and histogram matching. *Photogrammetric Engineering and Remote Sensing* 71 (9):1079–1089.

Huang, W. and M. Bu. 2015. Detecting shadows in high-resolution remote-sensing images of urban areas using spectral and spatial features. *International Journal of Remote Sensing* 36 (24):6224–6244.

Jain, V. and A. Khunteta. 2017. Shadow removal for umbrageous information recovery in aerial images. Pages 536–540 in *IEEE International Conference on Computer, Communications and Electronics (Comptelix)*, held in Jaipur, India, 1–2 July 2017.

Juan, L. and O. Gwun. 2009. A comparison of SIFT, PCA-SIFT and SURF. *International Journal of Image Processing* 3 (4):143–152.

Irvin, B. and J. R. McKeown. 1989. Methods for exploiting the relationship between buildings and their shadows in aerial imagery. *IEEE Transactions on System, Man and Cybernetics* 19 (6):1564–1575.

Laliberte, A. S., D. M. Browning and A. Rango. 2012. A comparison of three feature selection methods for object-based classification of sub-decimeter resolution UltraCam-L imagery. *International Journal of Applied Earth Observation and Geoinformation* 15:70–78.

Li, H., L. Zhang and H. Shen. 2014. An adaptive nonlocal regularized shadow removal method for aerial remote sensing images. *IEEE Transactions on Geoscience and Remote Sensing* 52 (1):106–120.

Lingua, A., D. Marenchino and F. Nex. 2009. Performance analysis of the SIFT operator for automatic feature extraction and matching in photogrammetric applications. *Sensors* 9 (5):3745–3766.

Lippitt, C. D. and D. Stow. 2015. Remote sensing theory and time-sensitive information. In *Time Sensitive Remote Sensing*, edited by C. Lippitt, D. Stow and L. Coulter, 1–10. New York: Springer Publishers.

Liu, W. and F. Yamazaki. 2012. Object-based shadow extraction and correction of high-resolution optical satellite images. *IEEE Journal of Selected Topics in Applied Earth Observations and Remote Sensing* 5 (4):1296–1302.

Lorenzi, L., F. Melgani and G. Mercier. 2012. A complete processing chain for shadow detection and reconstruction in VHR images. *IEEE Transactions on Geoscience and Remote Sensing* 50 (9):3440–3452.

Lowe, D. G. 2004. Distinctive image features from scale-invariant keypoints. *International Journal of Computer Vision* 60 (2):91–110.

Ma, H., Q. Qin and X. Shen. 2008. Shadow segmentation and compensation in high resolution satellite images. Pages 1036–1039 in *IEEE International Geoscience and Remote Sensing Symposium Vol. 2 (IGARSS)*, held in Boston, Mass., 7–11 July 2008.

Mikolajczyk, K. and C. Schmid. 2005. A performance evaluation of local descriptors. *IEEE Transactions on Pattern Analysis and Machine Intelligence* 27 (10):1615–1630.

Mitra, R., J. Zhang, S. Narayan, S. Ahmed, S. Chandran and A. Jain. 2017. Improved descriptors for patch matching and reconstruction. In *Proceedings of the IEEE International Conference on Computer Vision (ICCV) Workshop*, held in Venice, Italy.

Otsu, N. 1979. A threshold selection method from gray-level histograms. *IEEE Transactions on System, Man and Cybernetics* 9 (1):62–66.

Sarabandi, P., F. Yamazaki, M. Matsuoka and A. Kiremidjian. 2004. Shadow detection and radiometric restoration in satellite high resolution images. Pages 3744–3747 in *IEEE International Geoscience and Remote Sensing Symposium Vol. 6 (IGARSS)*, held in Anchorage, Alaska, 20–24 September 2004.

Storey, E. A. D., A. Stow, L. L. Coulter and C. Chen. 2017. Detecting shadows in multi-temporal aerial imagery to support near-real-time change detection. *GIScience and Remote Sensing* 54 (4):453–470.

Shu, J. S. P. and H. Freeman. 1990. Cloud shadow removal from aerial photographs. *Pattern Recognition* 23 (6):647–656.

Stow, D., A. Hope, A. T. Nguyen, S. Phinn and C. A. Benkelman. 1996. Monitoring detailed land surface changes using an airborne multispectral digital camera system. *IEEE Transactions on Geoscience and Remote Sensing* 34 (5):1191–1203.

Stow, D. 1999. Reducing the effects of misregistration on pixel-level change detection. *International Journal of Remote Sensing* 20 (12):2477–2483.

Stow, D., L. Coulter and S. Baer. 2003. A frame centre matching approach to registration for change detection with fine spatial resolution multi-temporal imagery. *International Journal of Remote Sensing* 24 (19):3873–3879.

Stow, D. A., L. C. Coulter, G. MacDonald, C. D. Lippitt, R. McCreight and N. Zamora. 2016. Evaluation of geometric elements of repeat station imaging and registration. *Photogrammetric Engineering and Remote Sensing* 82 (10):775–788.

Stow, D. A., C. D. Lippitt, L. L. Coulter and A. D. Loerch. 2018. Towards an end-to-end airborne remote sensing system for post-hazard assessment of damage to hyper-critical infrastructure: Research progress and needs. *International Journal of Remote Sensing* 39 (5):1441–1458.

Sundaresan, A., P. K. Varshney and M. K. Arora. 2007. Robustness of change detection algorithms in the presence of registration errors. *Photogrammetric Engineering and Remote Sensing* 73 (4):375–383.

Suri, S. and P. Reinartz. 2010. Mutual-information-based registration of TerraSAR-X and Ikonos imagery in urban areas. *IEEE Transactions on Geoscience and Remote Sensing* 48 (2):939–949.

Townshend, J. R. G., C. Gurney, J. McManus and C. O. Justice. 1992. The impact of misregistration on change detection. *IEEE Transactions on Geoscience and Remote Sensing* 30 (5):1054–1060.

Tsai, V. J. D. 2006. A comparative study on shadow compensation of color aerial images in invariant color models. *IEEE Transactions on Geoscience and Remote Sensing* 44 (6):1661–1671.

Wan, C. Y., B. A. King and Z. Li. 2012. An assessment of shadow enhanced urban remote sensing imagery of a complex city—Hong Kong. *International Archives of the Photogrammetry, Remote Sensing and Spatial Information Sciences* (*ISPRS)* 39 (B6):177–182.

Wang, B., A. Ono, K. Muramatsu and N. Fujiwara. 1999. Automated detection and removal of clouds and their shadows from Landsat TM images. *IEICE Transactions on Information and Systems* 82 (2):453–460.

Wei, X., Y. Zhang, Y. Gong and N. Zheng. 2018. Kernelized subspace pooling for deep local descriptors. In *Proceedings of the IEEE Conference on Computer Vision and Pattern Recognition*, held in Salt Lake City, Utah.

Wong, A. and D. A. Clausi. 2007. ARRSI: Automatic registration of remote-sensing images. *IEEE Transactions on Geoscience and Remote Sensing* 45 (5):1483–1492.

Zitová, B. and J. Flusser. 2003. Image registration methods: A survey. *Image and Vision Computing* 21 (11):977–1000.

APPLICATIONS PAPER

Assessment of Salt Marsh Change on Assateague Island National Seashore Between 1962 and 2016

Anthony Campbell and Yeqiao Wang

Abstract

Salt marshes provide extensive ecosystem services, including high biodiversity, denitrification, and wave attenuation. In the mid-Atlantic, sea level rise is predicted to affect salt marsh ecosystems severely. This study mapped the entirety of Assateague Island with Very High Resolution satellite imagery and object-based methods to determine an accurate salt marsh baseline for change analysis. Topobathymetric light detection and ranging was used to map the salt marsh and model expected tidal effects. The satellite imagery, collected in 2016 and classified at two hierarchical thematic schemes, were compared to determine appropriate thematic richness. Change analysis between this 2016 map and both a manually delineated 1962 salt marsh extent and image classification of the island from 1994 determined rates off change. The study found that from 1962 to 1994, salt marsh expanded by 4.01 ha/year, and from 1994 to 2016 salt marsh was lost at a rate of -3.4 ha/year. The study found that salt marsh composition, (percent vegetated salt marsh) was significantly influenced by elevation, the length of mosquito ditches, and starting salt marsh composition. The study illustrates the importance of remote sensing monitoring for understanding site-specific changes to salt marsh environments and the barrier island system.

Introduction

Salt marshes are essential ecosystems that have displayed high rates of loss historically due to land reclamation. Recently, salt marshes have continued to decline due to sea level rise (SLR) (Watson *et al.* 2016), eutrophication (Wigand *et al.* 2014), herbivory (Altieri *et al.* 2012), and anthropogenic disturbances (Gedan, Silliman, Bertness 2009). Salt marshes provide a large number of vital ecosystem services, including carbon sequestration, coastal resilience, and biodiversity (Zedler and Kercher 2005; Barbier *et al.* 2011). The long-term prognosis for salt marshes depends on accretion, migration, and SLR (Roman 2017). There is some disagreement about if extensive losses will occur due to biological feedbacks of salt marsh vegetation to SLR (Kirwan *et al.* 2016). However, there are reports of losses tied to SLR (Watson *et al.* 2016). Satellite remote sensing and change detection of salt marsh vegetation are critical to determining the efffect of SLR and other stressors.

The back bay of barrier island systems facilitates salt marsh formation with small tidal ranges and low wave energy. Storm events cause overwash and create inlets critical processes for barrier island systems and salt marsh establishment (Schupp *et al.* 2013). Overwash supplies sediment to the bayside salt marsh in areas with low sediment supply and high SLR (Walters *et al.* 2014). In Florida, SLR is predicted to alter the barrier island vegetation composition and elevation ranges (Foster *et al.* 2017). Hog Island, a barrier island, off the coast of Virginia, has experienced documented shifts in vegetation from grassland to woody vegetation (Zinnert *et al.* 2011); this increase in woody vegetation alters the surrounding vegetation composition and site characteristics (Thompson, Zinnert, Young 2017).

Previous remote sensing mapping of Assateague Island has excluded salt marsh environments (Nayegandhi, Brock, Wright 2005) or mapped the entire island across multiple years (Sneddon *et al.* 2017). Due to the spatial intricacy and temporal variability of salt marshes, high spatial resolution sensors should be used to map these systems (Klemas 2013). The spatial resolution has a more significant effect on the classification accuracy of salt marsh environments than spectral resolution (Belluco *et al.* 2006). Worldview-2 imagery has been shown to improve wetland mapping over Quickbird-2 imagery (Lane *et al.* 2014; Campbell *et al.* 2017). The tidal stage is another consideration when mapping salt marsh. Satellite imagery collected above mean low water (MLW) is expected to have some effect on the spectral signature of salt marsh vegetation and potentially the classification. Areas of likely inundation will be determined using topobathymetric light detection and ranging (lidar) and bathtub models (Campbell and Wang 2018).

Salt marshes are at risk of loss from SLR; however, the most recent rates of salt marsh change (2005–2009) suggest stability (Dahl and Stedman 2013). Barrier islands are predicted to follow a runaway transgression model in which SLR leads to salt marsh drowning increasing the back bay tidal prism and resulting in less sediment reaching the beach causing additional erosion (Deaton, Hein, Kirwan 2017; FitzGerald *et al.* 2008). Three salt marsh loss frameworks have been proposed drowning, pond collapse, and pond recovery, these regimes depend on accretion rates or pond bottoms keeping pace with SLR (Mariotti 2016). This study proposes geospatial metrics for differentiating between salt marsh drowning and pond collapse. Losses of salt marsh in a pond collapse regime are erosional processes driven by wind (Mariotti 2016). The salt marsh edge erosion was compared with pond and panne expansion to determine the similarity between a known erosional process and pond and panne expansion. The hypothesis that pond's experiencing collapse would expand at a similar rate to edge erosion as opposed to areas of salt marsh drowning, which should develop significantly faster.

This study mapped Assateague Island National Seashore (ASIS) with a focus on salt marsh vegetation. The very high

Anthony Campbell and Yeqiao Wang are with the Department of Natural Resources Science, University of Rhode Island, Kingston, RI 02881 (yqwang@uri.edu; anthony.d.campbell@yale.edu).

Anthony Campbell is currently with the School of Forestry & Environmental Studies, Yale University, New Haven, CT 06511.

Photogrammetric Engineering & Remote Sensing
Vol. 86, No. 3, March 2020, pp. 187–194.
0099-1112/20/187–194

doi: 10.14358/PERS.86.3.187

-resolution (VHR) satellite classification serves as a baseline for salt marsh change analysis to determine how the salt marsh changed over the last 50 years. The objectives of this study were to 1) classify the salt marsh at two thematic scales, 2) quantify salt marsh extent for the Maryland section of the island for 1962, 1994, and 2016, 3) quantify interior die off and edge erosion in relation to salt marsh extent and mosquito ditches, 4) compare interior die-off and pool development rates from 1994 to 2016 with the rates from 1962–1994, and 5) compare interior salt marsh loss with pond expansion and edge erosion.

Methodology

Study Area

Assateague Island is a 59.5-km barrier island spanning the border of Virginia, U.S. and Maryland, U.S. (38°4′N, 75°12′W) (Figure 1). Three conservation areas encompass the island Assateague Island National Seashore, Chincoteague National Wildlife Refuge, and Assateague State Park managed by the National Park Service, United States Fish and Wildlife, and the Maryland Department of Natural Resources, respectively. The National Park was created in 1965 by an act of the United States Congress after the destruction of the Ash Wednesday storm in1962 raised development concerns (Mackintosh 1982). The island is an important nesting ground for piping plover in Maryland and Virginia (Patterson, Fraser, Roggenbuck 1991). The island vegetation communities are determined by overwash regimes which have been altered by the stabilization of the Ocean City inlet and artificial dune construction (Roman and Nordstrom 1988). These altered processes were the impetus to remove sections of the foredune to increase overwash, resulting in reductions of sparse vegetation and increased piping plover productivity (Schupp *et al.* 2013). Feral horse herds are present in the Maryland and Virginia sides of the park. Horse grazing can negatively affect both dune vegetation and elevation (De Stoppelaire *et al.* 2004). The horses frequently graze in salt marsh environments with a preference for *Spartina alterniflora* over *Distichlis spicata* (Furbish and Albano 1993).

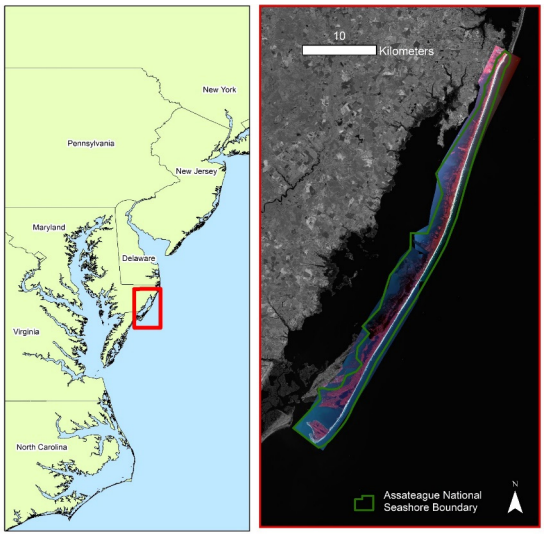

Figure 1. The map of the entire island was visualized using Worldview-2 satellite imagery collected 11 and 16 October 2016 used for the study and background imagery surrounding ASIS is Sentinel-2 MSI (RGB = Band 8) acquired 15 October 2016.

Data

Satellite imagery for this study was sourced from a variety of satellite and ancillary data including the Worldview-2 satellite that has VHR (0.5 m panchromatic) with eight spectral bands including coastal blue, blue, yellow, green, red, red edge, near-infrared (NIR) 1, and NIR 2. The data were acquired at 3:54 P.M. Universal Time Coordinated (UTC) 11 October 2016, and 4:09 P.M. (UTC) 16 October 2016. The tidal stages at the time of imagery acquisition were 49.4 cm and 49.7 cm above MLW, respectively (NOAA-COOPS 2017). The areas of expected inundation were assessed using inundation models derived from topobathymetric lidar (Campbell and Wang 2018). The topobathymetric lidar was used in the classification and analysis of expected tidal effects (NOAA 2014). The Sentinel-2 imagery was collected on 15 October 2016, from 3:42–3:45 P.M. (UTC) with a tidal stage of 0.268 m above MLW (NOAA-COOPS 2017).

Aerial imagery data acquired in 1962 (Maryland State Roads Commission 1964) were georeferenced with a combination of structure control points and hard landscape features. The data were acquired by the Maryland Department of Transportation and represent a preconservation state of the island. Salt marsh was delineated from the georeferenced images to determine the approximate extent of salt marsh on Assateague Island in 1962. Aerial imagery data acquired in 1962 were georeferenced with a combination of structure control points and hard landscape features. The data were acquired by the Maryland Department of Transportation and represent a preconservation state of the island. Salt marsh was delineated from the georeferenced images to determine the approximate extent of salt marsh on Assateague Island in 1962. Many studies have relied on the delineation of salt marsh from black and white aerial imagery to determine long-term change rates (Rafferty 2010; Watson *et al.* 2017; Schepers *et al.* 2017). The images are prone to some radial distortion; however, the island has limited topographic change. The imagery only covers the Maryland side of Assateague Island.

The 1994 image classification of ASIS had a 75% overall accuracy considering secondary associations (Sneddon *et al.* 2017). The study used aerial photography and photointerpretation to classify the barrier island to an Alliance level vegetation classification (Sneddon, Anderson, Metzler 1994). This study recoded the classification into two categories salt marsh and nonsalt marsh. The 1994 classes recoded as salt marsh were high salt marsh, low salt marsh, *Phragmites* wetland, needlerush marsh, and tidal salt scrub.

Segmentation

Object-based classification relies on the preclassification step of segmentation providing additional geospatial context about the patches that will be classified. There is rarely a single scale that is appropriate for an entire scene, especially the diverse ecological communities of a barrier island. Segmentation scale was analyzed with a mixture of methods from a previous statistically based exploration of segmentation scale (Espindola *et al.* 2006; Johnson and Xie 2011). Multiscale mean shift segmentation was used in this study. A single segmentation scale under-segments the salt marsh land cover; to counteract this, all objects with Worldview View Water Index > 0 were segmented at a spatial radius 10, spectral radius 8, and minimum object size of 10. The segmentation uses a larger neighborhood and less spectral range in the feature space resulting in increased differentiation between mudflat, water, and salt marsh vegetation types without further segmenting the upland areas. Upland and nonwater areas were segmented at a spatial radius of 5, spectral radius of 13, and minimum object size of 40 pixels.

Data and ancillary data layers were used to derive classification parameters for the image. Object parameters included

the mean, standard deviation, and range of each of the eight Worldview-2 spectral bands. Topobathymetric lidar-derived digital elevation model (DEM), digital surface model, and lidar intensity had their means, standard deviations, and ranges calculated. The DEM was created using minimum bin gridding; i.e., a pixel is assigned the minimum value of all lidar returns, which has been shown to reduce error in salt marsh elevation estimates (Schmid, Hadley, Wijekoon 2011). Geospatial characteristics such as area, perimeter, ratio perimeter to area, max distance between two nodes, and shape index were calculated for each object. Grey level co-occurrence matrix textures were calculated for a 3 × 3 pixel moving window, including inverse distance moment, contrast, difference entropy, and correlation.

Classification

The vegetation found on Assateague Island can be divided into three communities: Forested upland, dune and swale, and salt marsh (Stalter and Lamont 1990). This study explored the available training data to classify the dominant species level in the salt marsh environment. Two hierarchical thematic classifications were developed, species, and a community level classification. The community classes were *S. alterniflora*, patchy *S. alterniflora*, high marsh, sand, wrack, dune vegetation, mudflat, water, developed, and upland. The species classification divided upland into degraded loblolly pine, shrub, dune vegetation, and loblolly pine, and the high marsh category into *Iva frutescens*, *Spartina patens*, *Juncus gerardii*, and *D. spicata* classes. Remote sensing monitoring of upland vegetation change on the Barrier Islands is one component of understanding these interconnected biogeomorphic ecosystems (Zinnert *et al.* 2016). The two classification types were created to evaluate the methodology and data for the classification of dominant species in salt marsh environments (Campbell *et al.* 2017).

Vegetation plot data gathered across the island was used to create training and testing data sets. The Random Forest classifier was trained and classified objects within the R statistical environment using the Caret and randomForest packages. Random Forest is a nonparametric machine learning classification technique that creates many decision trees and then uses majority votes to determine a final class (Breiman 2001). Random Forest is an efficient and high performing algorithm for a variety of data (Fernández-Delgado *et al.* 2014), and particularly for land use and land cover (LULC) classification (Rodriguez-Galiano *et al.* 2012; Dronova *et al.* 2012). The vegetation data were collected for 1-m^2 vegetation plots. Percent cover was calculated with the Braun-Blanquet method (Braun-Blanquet 1964). Objects of the upland, developed, and water classes were visually interpreted from the imagery and knowledge from field visits. The training data were divided 60/40 between training and testing, and confusion matrices were computed with 1044 objects. The kappa, overall, user's, and producer's accuracy were all calculated to understand classification accuracy for both classifications.

Change Analysis

Change analysis was conducted for salt marsh change across the three mapping periods of 1962, 1994, and 2016. Salt marsh losses have been divided into four broad categories channel widening, interior die-off, shoreline erosion, and erosion of areas near the tidal connection of barrier islands and lagoon systems (Watson *et al.* 2017). In bay side environments such as the study site, the prevalent types of change are channel widening, shoreline erosion, interior die-off, and overwash. It has been suggested that channel widening, shoreline erosion, and pond collapse of salt marshes are associated with wave and tidal energy (Mariotti 2016). Salt marsh changes between 1994 and 2016 were explored with a comparison of shoreline length normalized loss between four landscape types: salt marsh edge, ponds, interior loss, and overwash areas. If drowning is the cause, then loss should be significantly greater in the salt marsh interior than in the salt marsh ponds.

The digitized salt marsh extent from the historic 1962 aerial imagery was used for change analysis of the Maryland side of ASIS. The uncertainty is large in this type of analysis due to data quality, georeferencing, and limited spectral information. Only areas imaged in the 1962 aerial imagery were included in the analysis. The change analysis included 1) 1962 digitized vegetation; 2) 2016 classes: *Phragmites* spp., patchy *S. alterniflora*, *S. alterniflora*, and high marsh; and 3) 1994 classes: high salt marsh, low salt marsh, *Phragmites* wetland, needlerush marsh, and tidal salt scrub.

Statistical Analysis

Contiguous salt marsh areas >¼ hectare within the 1962 extent were compared between 1962, 1994, and 2016 salt marsh areas with a one way ANOVA to understand salt marsh fragmentation across this time. The ¼-hectare cutoff was used to adhere to the 1994 data's minimum mapping unit (MMU).

Four landscape categories, bay edge, panne, pond, and overwash, were compared. Ponds were defined as nonvegetated pannes in the 1994 classification; these locations related to relatively permanent salt marsh ponds. Bay edge included those areas hydrologically connected to the back bay. Pannes were areas of interior die-off larger than ¼ hectare. The overwash areas were land, which became upland or sand in 2016—these locations related to areas that had been lost due to barrier island geomorphological processes such as overwash. The interior regions had no previous perimeter because they were vegetated in 1994. However, in 2016 the area had 10 558 nonvegetated pannes <¼ hectare. The mean and standard deviation of the perimeter of these patches were used to generate a set of random normally distributed baseline perimeters for interior areas for which data were lacking. The Kruskal-Wallis rank sum test was used to test for significant differences between the four classes. Post hoc Dunn's Kruskal-Wallis multiple comparisons were computed when applicable. Kruskal-Wallis rank sum test and the post hoc Dunn's Kruskal-Wallis were also used to compare 2014 topobathymetric elevations of the four landscape categories.

The coinciding extent of the salt marsh for 1962, 1994, and 2016 was divided into 70 520-m sections. The marsh extent for each period, mosquito ditch length, and change from 1994 to 2016 were calculated for each section. A multiple linear regression looked at the effect of distance from the Ocean City Inlet, 1994 extent, and length of mosquito ditches on salt marsh change.

Results

The image classifications of ASIS were successful in both thematic approaches, which achieved greater than 85% overall accuracy. The tidal effect was analyzed using the community classification. This classification was used for all other analyses due to the focus on changes to salt marsh extent.

Tidal Effect

The assessment of the extent of salt marsh inundation at the time of the Worldview-2 image used topobathymetric lidar and bathtub models to determine areas of potential inundation (Campbell and Wang 2018). The method used VDatum, however for this study site, the Ocean Inlet tidal datum was used, which likely overestimates the tidal effect given the smaller tidal range of the study areas. The tidal model used was 0.50 m above North American Vertical Datum (NAVD) 1988, which was a slightly higher tidal stage than the time of Worldview-2 data acquisitions. The inundated extent of *S. alterniflora* and high marsh at 0.50 m above NAVD 1988 was evaluated (Figure 2) and how many training locations were

inundated. To be considered, inundated pixels had to be connected to an area classified as water in the 2016 image classification. Of all *S. alterniflora* training points, 13.7% were inundated; of those with >25% vegetation cover, only 7.5% were inundated. In total, 11.1% of patchy *S. alterniflora,* 3.5% of *S. alterniflora*, and 0.34% of high marsh were inundated. Previous studies have suggested salt marsh mapping be conducted within 0–60 cm of MLW (Jensen *et al.* 1993).

Classification

The image classifications of ASIS were successful in both thematic approaches, which achieved greater than 85% overall accuracy. The community classification achieved an overall accuracy of 91.6% and a visually appealing result (see Table 1 and Figure 3). The species classification achieved 87.5% overall accuracy. *D. spicata* did not have adequate separation from *S. alterniflora,* which had more testing patches classified as *S. alterniflora* than as *D. spicata*, resulting in a 19% producer's accuracy. The classes were merged for the final species classification resulting in an overall accuracy of 89.8% (Table 2). The inclusion of several upland classes in the species classification had little effect on the accuracy while giving a more visually appealing result (Figure 4).

Change Analysis

The three-time periods had salt marsh extents of 1414.88 ha, 1543.23 ha, and 1466 ha in 1962, 1994, and 2016, respectively. These corresponded with change rates of 4.01 ha/year from 1962 to 1994 and –3.5 ha/year from 1994 to 2016. Significant increases in salt marsh area were prevalent from 1962 to 1994, though declines were found between 1994 to 2016 due to interior loss and edge erosion (Figure 5).

From 1994–2016, extensive change was found over the 22 years. This analysis considered a larger area of salt marsh. Salt marsh extent was reduced, and the upland areas were converted to salt marsh. From 1994–2016 the net loss of salt marsh area was 77.23 ha. Salt marsh losses were separated into four categories, interior die-off, edge erosion, pond collapse, and overwash, depending on location and change categories. The rectified 1962 images achieved a root mean square error of 2.65. These images were used to map salt marsh extent from the Ocean City inlet to approximately 38.8 km south. The resulting salt marsh extent was 1414.88 ha in 1962. Interior ponds and mudflat were digitized finding 738 pannes or ponds with a total area of 43.56 ha.

Unvegetated pannes mapped in the 1994 data were analyzed to determine pannes trajectory. Did pannes persist, expand, or become vegetated in 2016? The 383 pannes had an average 1994 extent of 2736.87 m². Of the 383 1994 pannes, 216 coincided with 2016 pannes. From 1994 to 2016, 49

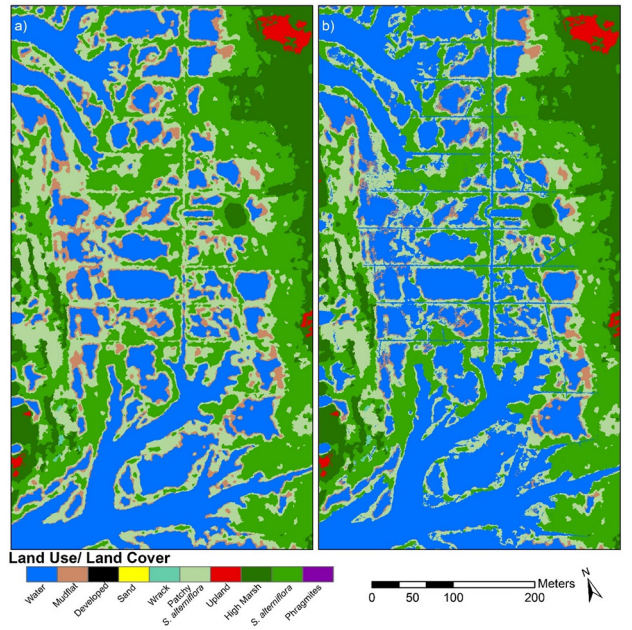

Figure 2. The classified salt marsh south of the Verrazano Bridge. (a) The community classification of ASIS. (b) The community classification with areas inundated at a tidal stage of 0.50 m above NAVD 1988 as determined with bathtub models.

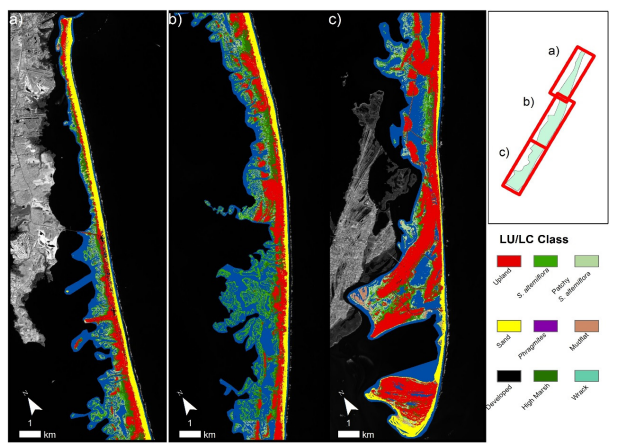

Figure 3. The map shows the community classification for the entirety of ASIS with Sentinel-2 NIR band.

Table 1. Accuracy assessment of the community classification of ASIS, confusion matrix of the classification of ASIS, and verification data in the columns and classified data in the rows.

Class	Developed	High marsh	Mudflat	Phragmites	Sand	Patchy *S. alterniflora*	*S. alterniflora*	Upland	Water	Wrack	User's Accuracy
Developed	40	0	0	0	0	0	0	0	0	0	100
High marsh	0	103	0	0	0	0	14	8	0	0	82.4
Mudflat	0	0	40	0	0	6	0	0	3	0	81.6
Phragmites	0	0	0	8	0	0	0	0	0	0	100
Sand	0	0	0	0	119	0	0	0	0	1	99.2
Patchy *S. alterniflora*	0	5	18	0	0	144	0	0	0	1	85.7
S .alterniflora	0	12	0	0	0	0	216	0	0	0	94.7
Upland	1	12	0	5	1	0	1	210	0	1	91.0
Water	0	0	2	0	0	0	0	0	116	0	98.3
Wrack	0	0	0	0	1	1	0	0	0	17	89.5
Producer's Accuracy	97.6	78.0	57.1	61.5	98.3	95.4	93.5	96.3	97.4	85.0	OA = 91.6% / KAPPA = 0.90

decreased in area and 147 pannes developed surficial connections with the Bay. The average rate of change was 121.35 m^2/year increase in panne extent. There was no significant difference between the rates of panne expansion for those with surficial links to the Bay and without ($F_{(1,328)} = 1.926$, $p = 0.166$).

The Kruskal-Wallis sum rank test comparing edge erosion and other types of loss found significant differences between landscape types, salt marsh edge, ponds, interior loss, and overwash areas (H(3) = 690.25, $p < 0.001$). When post hoc Dunn's test of multiple comparisons was conducted, all locations were significantly different except for interior loss compared with overwash ($p = 0.89$). The mean elevation of each landscape type was found to be significantly different from all the others (H(3) = 2578.1, $p < 0.001$).

The analysis of the Maryland section from 1994–2016 by division into sections of coastline demonstrates a complex

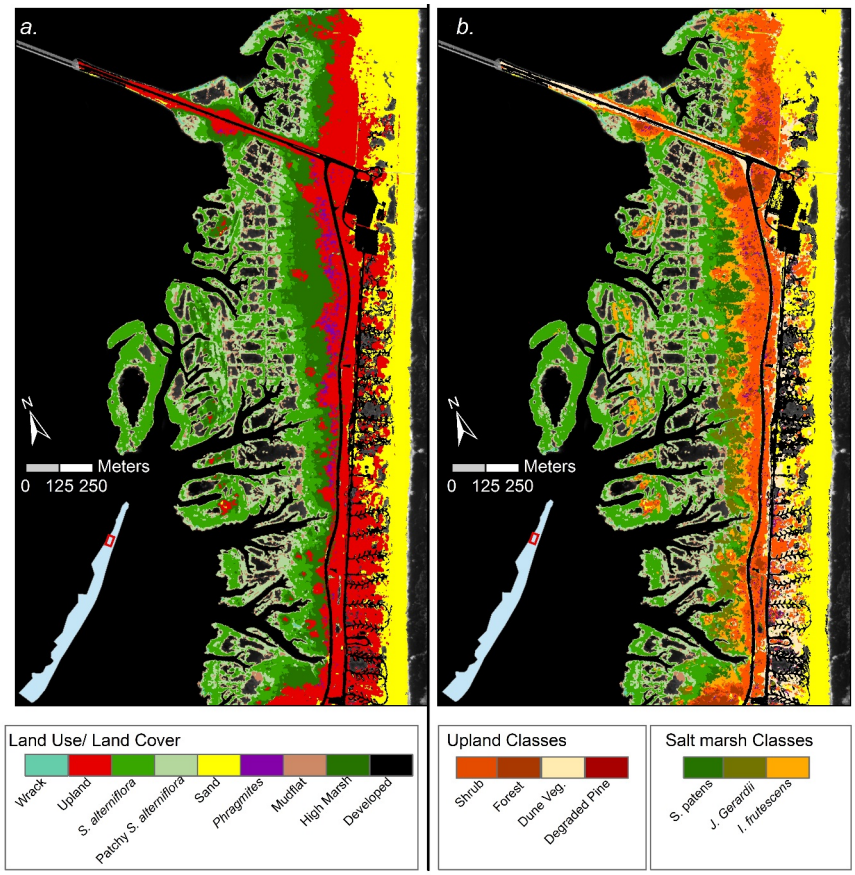

Figure 4. (a) The community classification in a section of the Maryland side of ASIS south of the Verrazano Bridge. (b) The species classifications for the same area below the Verrazano Bridge. The shared legend resides under the community map. Additional classes for the species classification are below the species map.

Table 2. Confusion matrix of the species classification.

Class	De	D	DU	IVA	JG	M	SP	PH	Pine	Sand	SH	PSA	SA	W	WR	User's Accuracy
DeP	42	0	0	0	0	0	0	0	2	0	0	0	0	0	0	0.95
D	0	42	0	0	0	0	0	0	0	1	0	0	0	0	0	0.98
DU	0	0	36	0	0	0	0	1	0	0	0	0	0	0	0	0.97
IVA	0	0	0	26	0	0	7	0	0	0	6	0	0	0	0	0.67
JG	0	0	0	0	24	0	0	0	0	0	0	0	1	0	0	0.96
M	0	0	0	0	0	41	0	0	0	0	0	8	0	0	0	0.84
SP	0	0	0	3	0	0	52	0	0	0	7	0	2	0	0	0.81
PH	0	0	0	0	0	0	0	9	0	0	2	0	0	0	0	0.82
Pine	0	0	0	0	0	0	0	0	114	0	2	0	0	0	0	0.98
Sand	0	1	2	0	0	0	0	0	0	119	0	0	0	0	0	0.98
SH	0	0	1	2	0	0	4	4	2	0	17	0	0	0	0	0.57
PSA	0	0	0	0	0	18	4	0	0	0	0	135	4	0	0	0.84
SA	0	0	0	4	5	0	12	0	0	0	0	4	211	0	0	0.89
W	0	0	0	0	0	3	0	0	0	0	0	0	0	120	0	0.98
WR	0	0	0	0	0	0	0	0	0	1	0	2	0	0	21	0.87
Producer's Accuracy	1.00	0.98	0.74	0.74	0.83	0.66	0.80	0.64	0.97	0.98	0.50	0.91	0.96	1.00	1.00	OA: 89.8% Kappa: 0.88

Abbreviations used are *SA* = *S. alterniflora*, PSA = Patchy *S. alterniflora*, IVA = *Iva frutescens,* PH = *Phragmites,* De = die-off pine forest, D = developed, M = mudflat, SP = *Spartina patens*, SH = shrub, DU = dune vegetation, JG= *Juncus gerardii,* WR = Wrack, W = Water.

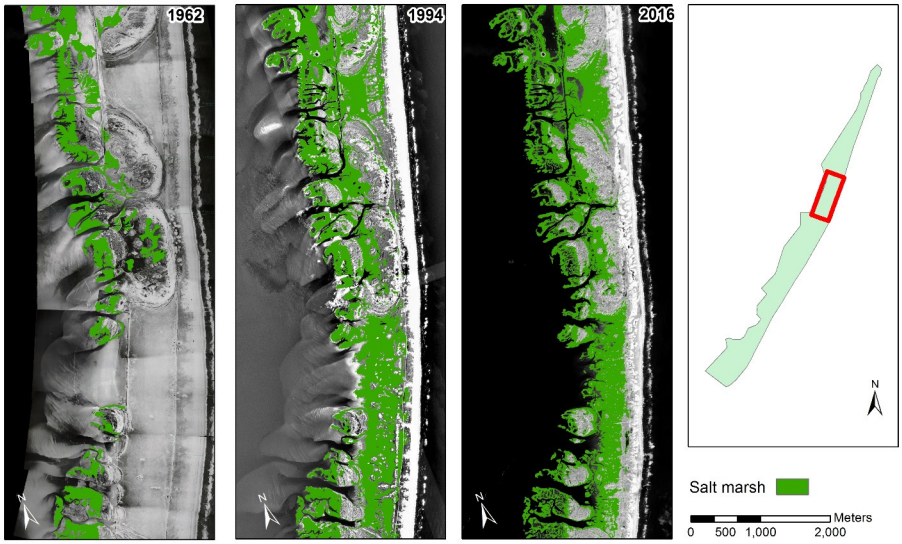

Figure 5. The maps show the salt marsh extent in 1962, 1994, and 2016. The cleared area around the Ocean Beach development is evident in the 1962 imagery as well as Baltimore Blvd. a paved road parallel to the shoreline. The 1994 extent background imagery is a 1989 digital orthophoto quadrangle.

pattern of change (Figure 6). The multiple linear regression found a significant influence of the initial salt marsh extent, distance from the inlet, and mosquito ditch length on salt marsh change ($F_{(3,67)} = 39.84$, $p > 0.001$) and R^2 of 0.64. The further from Ocean City inlet, the more likely an increase to marsh extent was observed, ($p > 0.05$), larger 1994 area corresponded to a greater loss ($p > 0.001$), and more length of mosquito ditches ($p < 0.05$).

Discussion

Assateague Island will likely experience greater SLR than the global average (Sweet *et al.* 2017), has a low sediment budget and microtidal range. Salt marshes with these characteristics are expected to be those at the most risk of loss from SLR (Roman 2017). Establishing a reasonable baseline and using available historic imagery and classifications are integral steps to understanding local salt marsh change in context.

Tidal Effect

The inclusion of inundated pixels in the training data may have resulted in overestimating the extent of patchy *S. alterniflora.* The classification of inundated pixels as vegetated classes suggested a minimal effect of tidal inundation on the image classification due to the use of object-based image analysis, which considers entire objects, not individual pixels. However, it illustrates that tidal flooding occurred within the 0–60 cm tidal stage. Mosquito ditches that were not wide enough to be classified otherwise were evident with the modeled inundation maps. The map with the inundation model offered a refined delineation of mosquito ditches. This map was not used in the change analysis because these features were not delineated in either the 1994 or 1962 map.

Change Detection

The 1962 imagery represents a pre-National Seashore environment, the Ocean Beach development project had cleared land, paved a road, and sold 5850 lots (Mackintosh 1982). The increase in salt marsh extent from 1962 to 1994 demonstrates the recovery of the reclaimed salt marsh area and a dramatic shift in the management of the island. Salt marsh expansion from 1962–1994 was most prominent in the regions that had been cleared for development in the 1950s (Figure 6), suggesting that at least some of these areas were salt marshes

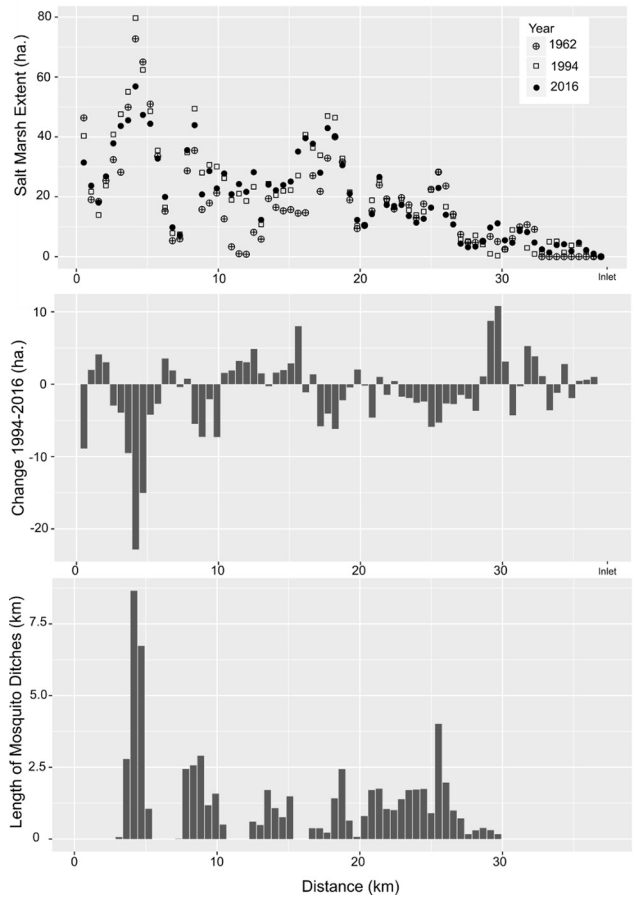

Figure 6. The three insets show for 70 shore parallel sections of the MD side of ASIS. (a) salt marsh extent in 1962, 1994, and 2016, (b) the change in salt marsh extent from 1994 to 2016 and (c) the length of mosquito ditches within each section.

before being cleared and divided into plots. The salt marsh expansion from 1962 to 1994 reflects the successful creation and management of the National Seashore to conserve natural resources. Uncertainty accompanies historical image digitization and georeferencing of natural environments. However, these methods are one of the few options for understanding geospatial changes in salt marsh extent over the last century.

Thematic and MMU differences between the two classification schemes contribute to the uncertainty in this estimate. Conservation areas such as ASIS are useful for understanding salt marsh migration unimpeded by hardened shorelines and coastal development. The relationships explored in this study explained little of the variability evident in panne expansions and mudflat salt marsh composition, perhaps due in part, to unquantified drivers of change from sources such as herbivory, eutrophication, edaphic conditions, variation in tidal range, and issues with scale and data accuracy.

Conclusions

This study used both the contiguous natural areas of salt marsh and cross-sections of the island to determine the influence of various parameters on salt marsh change. The two approaches demonstrated agreement. Salt marsh location and landform are important determinates for selecting an appropriate change analysis approach. The Assateague Island salt marshes were influenced by distance to the inlet, mosquito ditches, elevation, and starting salt marsh extent. These attributes were explored in this study, and additional *in situ* studies could reveal other sources of change, such as herbivory from both wild horses and marsh snails.

Change analysis using VHR satellite remote sensing data are an essential component of understanding decadal salt marsh variation. The uncertainty of the changes measured in this study includes the differences in classification approach, data, and sparse temporal phases. An increase in salt marsh area was observed between 1962 and 1994. However, without additional temporal resolution, the dynamics of these changes are unknown. The frequency of VHR imagery acquisition must balance the cost with the salt marshes temporal scale of change. Processes such as wind-driven edge erosion and drowning by SLR are evident over long periods. While salt marsh drowning is a gradual change, processes such as wrack deposition, overwash, and herbivory can change areas rapidly. To balance these scales, it is often best to monitor at approximately a five-year interval for this study area. Future studies of the site could examine the use of other types of data to understand the salt marsh change with higher temporal resolution.

Acknowledgments

This project was funded by the Northeast Coastal and Barrier Network (NCBN) of the National Park Service (NPS)'s Inventory and Monitoring Program under the Task Agreement Number P14AC00230. We appreciate the guidance and support of Sara Stevens, Dennis Skidds, Bill Thompson, and Charles Roman of the NPS NCBN and North Atlantic Coast CESU. Mark Christiano provided reference data and field support for this project. The authors appreciate the assistance by administrators and professionals from Assateague Island National Seashore (ASIS), particularly Neil Winn for his expertise, insights, field guidance and logistic support.

References

Altieri, A. H., M. D. Bertness, T. C. Coverdale, N. C. Herrmann and C. Angelini. 2012. A trophic cascade triggers collapse of a salt-marsh ecosystem with intensive recreational fishing. *Ecology* 93:1402–1410.

Barbier, E. B., S. D. Hacker, C. Kennedy, E. W. Koch, A. C. Stier and B. R. Silliman. 2011. The value of estuarine and coastal ecosystem services. *Ecological Monographs* 81:169–193.

Belluco, E., M. Camuffo, S. Ferrari, L. Modenese, S. Silvestri, A. Marani and M. Marani. 2006. Mapping salt-marsh vegetation by multispectral and hyperspectral remote sensing. *Remote Sensing of Environment* 105 (1):54–67.

Bertness, M. D., K. Wikler and T. Chatkupt. 1992. Flood tolerance and the distribution of *Iva frutescens* across New England salt marshes. *Oecologia* 91 (2):171–178.

Breiman, L. 2001. Random forests. *Machine Learning* 45:5–32.

Cameron Engineering and Associates. 2015. Long Island tidal wetlands trends analysis. New England Interstate Water Pollution Control Commission 1:207.

Campbell, A. and Y. Wang. 2018. Examining the influence of tidal stage on salt marsh mapping using high-spatial-resolution satellite remote sensing and topobathymetric LiDAR. *IEEE Transactions on Geoscience and Remote Sensing.*

Campbell, A., Y. Wang, M. Christiano and S. Stevens. 2017. Salt marsh monitoring in Jamaica Bay, New York from 2003 to 2013: A decade of change from restoration to Hurricane Sandy. *Remote Sensing* 9 (2):131.

Craft, C. B., E. D. Seneca and S. W. Broome. 1993. Vertical accretion in microtidal regularly and irregularly flooded estuarine marshes. *Estuarine, Coastal and Shelf Science* 37 (4):371–386.

Dahl, T. E. 2011. Status and trends of wetlands in the conterminous United States 2004 to 2009. U.S. Department of the Interior; Fish and Wildlife Service, Washington, D.C.: 108.

De Stoppelaire, G. H., T. W. Gillespie, J. C. Brock and G. A. Tobin. 2004. Use of remote sensing techniques to determine the effects of grazing on vegetation cover and dune elevation at Assateague Island National Seashore: Impact of horses. *Environmental Management* 34:642–649.

Deaton, C. D., C. J. Hein and M. L. Kirwan. 2017. Barrier island migration dominates ecogeomorphic feedbacks and drives salt marsh loss along the Virginia Atlantic Coast, USA. *Geology* 45:123–126.

Dronova, I., P. Gong, N. E. Clinton, L. Wang, W. Fu, S. Qi and Y. Liu. 2012. Landscape analysis of wetland plant functional types: The effects of image segmentation scale, vegetation classes and classification methods. *Remote Sensing of Environment* 127 (0):357–369.

Espindola, G. M., G. Câmara, I. A. Reis, L. S. Bins and A. M. Monteiro. 2006. Parameter selection for region-growing image segmentation algorithms using spatial autocorrelation. *International Journal of Remote Sensing* 27 (14):3035–3040.

Fernández-Delgado, M., E. Cernadas, S. Barro and D. Amorim. 2014. Do we need hundreds of classifiers to solve real world classification problems. *Journal of Machine Learning Research* 15:3133–3181.

FitzGerald, D. M., M. S. Fenster, B. A. Argow and I. V. Buynevich. 2008. Coastal impacts due to sea-level rise. *Annual Review of Earth and Planetary Science* 36:601–647.

Foster, T. E., E. D. Stolen, C. R. Hall, R. Schaub, B. W. Duncan, D. K. Hunt, *et al.* 2017. Modeling vegetation community responses to sea-level rise on Barrier Island systems: A case study on the Cape Canaveral Barrier Island complex, Florida, USA. *PLoS One* 12:e0182605.

Furbish, C. E. and M. Albano. 1994. Selective herbivory and plant community structure in a mid-Atlantic salt marsh. *Ecology* 75:1015–1022.

Gedan, K. B., B. R. Silliman and M. D. Bertness. 2009. Centuries of human-driven change in salt marsh ecosystems. Annual Review of Marine Science. 1:117–41.

Jensen, J. R., D. J. Cowen, J. D. Althausen, S. Narumalani and O. Weatherbee. 1993. An evaluation of the CoastWatch change detection protocol in South Carolina. *Photogrammetric Engineering and Remote Sensing* 59 (6):1039–1044.

Johnson, B. and Z. Xie. 2011. Unsupervised image segmentation evaluation and refinement using a multi-scale approach. *ISPRS Journal of Photogrammetry and Remote Sensing* 66 (4):473–483.

Klemas, V. 2013. Remote sensing of emergent and submerged wetlands: an overview. *International Journal of Remote Sensing* 34:6286–6320

Kirwan, M. L., S. Temmerman, E. E. Skeehan, G. R. Guntenspergen and S. Fagherazzi. 2016. Overestimation of marsh vulnerability to sea level rise. *Nature Climate Change* 6:253–260.

Lane, C. R., H. Liu, B. C. Autrey, O. A. Anenkhonov, V. V. Chepinoga and Q. Wu. 2014. Improved wetland classification using eight-band high resolution satellite imagery and a hybrid approach. *Remote Sensing* 6:12187–12216.

Mackintosh, B. 1982. Assateague Island national seashore : An administrative history. Washington, D.C., National Park Service, History Division.

Mariotti, G. 2016. Revisiting salt marsh resilience to sea level rise: Are ponds responsible for permanent land loss? *Journal of Geophysical Research: Earth Surface* 121:1391–1407.

Maryland State Roads Commission. 1964. Aerial Photography—Ocean City (1952–1964). <https://jscholarship.library.jhu.edu/handle/1774.2/36062>.

Nayegandhi, A., J. C. Brock and C. W. Wright. 2005. Classifying vegetation using NASA's Experimental Advanced Airborne Research Lidar (EAARL) at Assateague Island National Seashore.

NOAA-COOPS. 2017. Ocean City Inlet, MD—Station ID: 8450283. <https://tidesandcurrents.noaa.gov/stationhome.html?id=8570283> Accessed 10 November 2017.

NOAA 2014. NOAA post Hurricane Sandy topobathymetric LiDAR mapping for shoreline mapping. Silver Spring, Md.: National Oceanic and Atmospheric Administration, National Ocean Service, National Geodetic Survey, Remote Sensing Division. <https://coast.noaa.gov/htdata/lidar1_z/geoid12b/data/4800/>.

Patterson, M. E., J. D. Fraser and J. W. Roggenbuck. 1991. Factors affecting piping plover productivity on Assateague Island. *The Journal of Wildlife Management* 525–531.

Rafferty, P., J. Castagna and D. Adamo. 2010. Building partnerships to restore an urban marsh ecosystem at Gateway National Recreation Area. *Park Science* 27:34–41.

Redfield, A. C. 1972. Development of a New England salt marsh. *Ecological Monographs* 42:201–237.

Roman, C. T. and K. F. Nordstrom. 1988. The effect of erosion rate on vegetation patterns of an east coast barrier island. *Estuarine, Coastal and Shelf Science* 26:233–242.

Roman, C. T., J. W. King, D. R. Cahoon, J. C. Lynch and P. G. Appleby. 2007. Evaluation of marsh development processes at Fire Island National Seashore (New York): Recent and historic perspectives. Boston, Mass.: Technical Report NPS/NER/NRTR—2007/089, National Park Service.

Roman, C. T. 2017. Salt marsh sustainability: Challenges during an uncertain future. *Estuaries and Coasts* 40:711–716.

Schepers, L., M. Kirwan, G. Guntenspergen and S. Temmerman. 2017. Spatio-temporal development of vegetation die-off in a submerging coastal marsh. *Limnology and Oceanography* 62:137–150.

Schmid, K. A., B. C. Hadley and N. Wijekoon. 2011. Vertical accuracy and use of topographic LIDAR data in coastal marshes. *Journal of Coastal Research* 27:116–132.

Schupp, C. A., N. T. Winn, T. L. Pearl, J. P. Kumer, T. J. Carruthers and C. S. Zimmerman. 2013. Restoration of overwash processes creates piping plover (Charadrius melodus) habitat on a barrier island (Assateague Island, Maryland). *Estuarine, Coastal and Shelf Science* 116:11–20.

Sneddon, L., J. Menke, A. Berdine, E. Largay and S. Gawler. 2017. Vegetation classification and mapping of Assateague Island National Seashore. Fort Collins, Colo.: Natural Resource Report NPS/ASIS/NRR—2017/1422, National Park Service.

Sneddon, L., M. Anderson and K. Metzler. 1994. A classification and description of terrestrial community alliances in The Nature Conservancy's Eastern Region: First approximation. Boston, Mass.: Unpublished report to USDI Fish & Wildlife Service, Gap Analysis Program, The Nature Conservancy, Eastern Heritage Task Force: 116.

Stalter, R. and E. E. Lamont. 1990. The vascular flora of Assateague Island, Virginia. *Bulletin of the Torrey Botanical Club* 117:48–56.

Sweet, W., R. E. Kopp, C. P. Weaver, J. Obeysekera, R. M. Horton, E. R. Thieler and C. Zervas. 2017. Global and regional sea level rise scenarios for the United States. NOAA Technical Report NOS CO-OPS 083.

Rodriguez-Galiano, V. F., B. Ghimire, J. Rogan, M. Chica-Olmo and J. P. Rigol-Sanchez. 2012. An assessment of the effectiveness of a random forest classifier for land-cover classification. *ISPRS Journal of Photogrammetry and Remote Sensing* 67:93–104.

Thompson, J. A., J. C. Zinnert and D. R. Young. 2017. Immediate effects of microclimate modification enhance native shrub encroachment. *Ecosphere:* 8.

Walters, D., L. J. Moore, O. Duran Vinent, S. Fagherazzi and G. Mariotti. 2014. Interactions between barrier islands and backbarrier marshes affect island system response to sea level rise: Insights from a coupled model. *Journal of Geophysical Research: Earth Surface* 119:2013–2031.

Watson, E. B., K. B. Raposa, J. C. Carey, C. Wigand and R. S. Warren. 2016. Anthropocene survival of southern New England's salt marshes. *Estuaries and Coasts*: 1–9.

Watson, E. B., C. Wigand, E. W. Davey, H. M. Andrews, J. Bishop and K. B. Raposa. 2017. Wetland loss patterns and inundation-productivity relationships prognosticate widespread salt marsh loss for southern New England. *Estuaries and Coasts* 40:662–681.

Wigand, C., C. T. Roman, E. Davey, M. Stolt, R. Johnson, A. Hanson, *et al.* 2014. Below the disappearing marshes of an urban estuary: Historic nitrogen trends and soil structure. *Ecological Applications* 24:633–649.

Zedler, J. B. and S. Kercher. 2005. Wetland resources: Status, trends, ecosystem services, and restorability. *Annual Review of Environmental and Resources* 30:39–74.

Zinnert, J. C., S. A. Shiflett, J. K. Vick and D. R. Young. 2011. Woody vegetative cover dynamics in response to recent climate change on an Atlantic coast barrier island: A remote sensing approach. *Geocarto International* 26:595–61.

Zinnert, J. C., S. A. Shiflett, S. Via, S. Bissett, B. Dows, P. Manley, *et al.* 2016. Spatial-temporal dynamics in barrier island upland vegetation: The overlooked coastal landscape. *Ecosystems* 19:685–697.

Digital Elevation Model Technologies and Applications: The DEM Users Manual, 3rd Edition

Edited by David F. Maune, PhD, CP
and Amar Nayegandhi, CP, CMS

To order, visit https://www.asprs.org/dem

The 3rd edition of the DEM Users Manual includes 15 chapters and three appendices. References in the eBook version are hyperlinked. Chapter and appendix titles include:

1. Introduction to DEMs
   David F. Maune, Hans Karl Heidemann, Stephen M. Kopp, and Clayton A. Crawford
2. Vertical Datums
   Dru Smith
3. Standards, Guidelines & Specifications
   David F. Maune
4. The National Elevation Dataset (NED)
   Dean B. Gesch, Gayla A. Evans, Michael J. Oimoen, and Samantha T. Arundel
5. The 3D Elevation Program (3DEP)
   Jason M. Stoker, Vicki Lukas, Allyson L. Jason, Diane F. Eldridge, and Larry J. Sugarbaker
6. Photogrammetry
   J. Chris McGlone and Scott Arko
7. IfSAR
   Scott Hensley and Lorraine Tighe
8. Airborne Topographic Lidar
   Amar Nayegandhi and Joshua Nimetz
9. Lidar Data Processing
   Joshua M. Novac
10. Airborne Lidar Bathymetry
    Jennifer Wozencraft and Amar Nayegandhi
11. Sonar
    Guy T. Noll and Douglas Lockhart
12. Enabling Technologies
    Bruno M. Scherzinger, Joseph J. Hutton, and Mohamed M.R. Mostafa
13. DEM User Applications
    David F. Maune
14. DEM User Requirements & Benefits
    David F. Maune
15. Quality Assessment of Elevation Data
    Jennifer Novac

Appendix A. Acronyms

Appendix B. Definitions

Appendix C. Sample Datasets

This book is your guide to 3D elevation technologies, products and applications. It will guide you through the inception and implementation of the U.S. Geological Survey's (USGS) 3D Elevation Program (3DEP) to provide not just bare earth DEMs, but a full suite of 3D elevation products using Quality Levels (QLs) that are standardized and consistent across the U.S. and territories. The 3DEP is based on the National Enhanced Elevation Assessment (NEEA) which evaluated 602 different mission-critical requirements for and benefits from enhanced elevation data of various QLs for 34 Federal agencies, all 50 states (with local and Tribal input), and 13 non-governmental organizations.

The NEEA documented the highest Return on Investment from QL2 lidar for the conterminous states, Hawaii and U.S. territories, and QL5 IfSAR for Alaska.

Chapters 3, 5, 8, 9, 13, 14, and 15 are "must-read" chapters for users and providers of topographic lidar data. Chapter 8 addresses linear mode, single photon and Geiger mode lidar technologies, and Chapter 10 addresses the latest in topobathymetric lidar. The remaining chapters are either relevant to all DEM technologies or address alternative technologies including photogrammetry, IfSAR, and sonar.

As demonstrated by the figures selected for the front cover of this manual, readers will recognize the editors' vision for the future – a 3D Nation that seamlessly merges topographic and bathymetric data from the tops of the mountains, beneath rivers and lakes, to the depths of the sea.

Co-Editors

David F. Maune, PhD, CP and
Amar Nayegandhi, CP, CMS

PRICING

Student (must submit copy of Student ID)	$50 +S&H
ASPRS Member	$80 +S&H
Non-member	$100 +S&H
E-Book (only available in the Amazon Kindle store)	$85

PE&RS

PE&RS 2020 Advertising Rates

PHOTOGRAMMETRIC ENGINEERING & REMOTE SENSING

The official journal for imaging and geospatial information science and technology

Advertise in the #1 publication in the imaging and geospatial information industry!

asprs THE IMAGING & GEOSPATIAL INFORMATION SOCIETY

Impact Factor (2018): 3.15

PE&RS (Photogrammetric Engineering & Remote Sensing) is the official journal of the American Society for Photogrammetry and Remote Sensing—the Imaging and Geospatial Information Society (ASPRS). This highly respected publication is the #1 publication in the industry by a wide margin. Advertisers with a desire to reach this market can do no better than PE&RS. It delivers the right audience of professionals who are loyal and engaged readers, and who have the purchasing power to do business with you.

***PE&RS* Readership Highlights**

Circulation:	Total audience:
3,000	6,400*

Founded in 1934, the American Society for Photogrammetry and Remote Sensing (ASPRS) is a scientific association serving professional members throughout the world. Our mission is to advance knowledge and improve understanding of mapping sciences to promote the responsible applications of photogrammetry, remote sensing, geographic information systems (GIS), and supporting technologies.

Our members are analysts/specialists, educators, engineers, managers/administrators, manufacturers/ product developers, operators, technicians, trainees, marketers, and scientists/researchers. Employed in the disciplines of the mapping sciences, they work in the fields of Agriculture/Soils, Archeology, Biology, Cartography, Ecology, Environment, Forestry/Range, Geodesy, Geography, Geology, Hydrology/Water Resources, Land Appraisal/ Real Estate, Medicine, Transportation, and Urban Planning/Development.

RESERVE YOUR SPACE TODAY!

Bill Spilman, ASPRS Advertising, Exhibit Sales & Sponsorships
(877) 878-3260 toll-free
(309) 483-6467 direct
(309) 483-2371 fax
bill@innovativemediasolutions.com

	Corporate Member Exhibiting at a 2019 ASPRS Conference	Corporate Member	Exhibitor	Non Member
All rates below are for four-color advertisments				
Cover 1	$1,850	$2,000	$2,350	$2,500
In addition to the cover image, the cover sponsor receives a half-page area to include a description of the cover (maximum 500 words). The cover sponsor also has the opportunity to write a highlight article for the journal. Highlight articles are scientific articles designed to appeal to a broad audience and are subject to editorial review before publishing. The cover sponsor fee includes 50 copies of the journal for distribution to their clients. More copies can be ordered at cost.				
Cover 2	$1,500	$1,850	$2,000	$2,350
Cover 3	$1,500	$1,850	$2,000	$2,350
Cover 4	$1,850	$2,000	$2,350	$2,500
Advertorial	1 Complimentary Per Year	1 Complimentary Per Year	$2,150	$2,500
Full Page	$1,000	$1,175	$2,000	$2,350
2 page spread	$1,500	$1,800	$3,200	$3,600
2/3 Page	$1,100	$1,160	$1,450	$1,450
1/2 Page	$900	$960	$1,200	$1,200
1/3 Page	$800	$800	$1,000	$1,000
1/4 Page	$600	$600	$750	$750
1/6 Page	$400	$400	$500	$500
1/8 Page	$200	$200	$250	$250
Other Advertising Opportunities				
Wednesday Member Newsletter Email Blast	1 Complimentary Per Year	1 Complimentary Per Year	$600	$600

A 15% commission is allowed to recognized advertising agencies

THE MORE YOU ADVERTISE THE MORE YOU SAVE! *PE&RS* offers frequency discounts. Invest in a three-times per year advertising package and receive a 5% discount, six-times per year and receive a 10% discount, 12-times per year and receive a 15% discount off the cost of the package.

*Based on 2 readers per copy as well as online views| Source: *PE&RS* Readership Survey, Fall 2012

ASPRS BOOKSTORE

visit **asprs.org**

available at **amazon**

Digital Elevation Model Technologies & Applications, 3rd Ed
Co-Editors: David F. Maune, PhD, CP, CFM, PSM, PS, GS, SP and Amar Nayegandhi, CP, CMS-Remote Sensing
List Price: $100 | **ASPRS Members:** $80
ASPRS Student Members: $50†
Also available for Amazon Kindle
Amazon Kindle Price:** $85

Landsat's Enduring Legacy: Pioneering Global Land Observations From Space
Landsat Legacy Project Team
ISBN: ISBN 1-57083-101-7 · Hardcover · 586 pages · 2017 · Stock #4958
List Price: $95 | **ASPRS Members:** $65
Student Members: $60
Amazon Price*: $100

Manual of Airborne Topographic Lidar
Editor: Michael S. Renslow
ISBN: 1-57083-097-5 · Hardcover · 528 pages · 2012 · Stock #4587
List Price: $150 | **ASPRS Members:** $95
Student Members: $75
Amazon Price (hardcover)*: $135
Also available for Amazon Kindle
AmazonKindle Price:** $110

Manual of Photogrammetry, Sixth Edition
Editor: J. Chris McGlone
ISBN: 1-57083-099-1 · Hardcover · 1372 pages · 2013 · Stock #4737
List Price: $175 | **ASPRS Members:** $125
Student Members: $98
Amazon Price*: $175

Glossary of the Mapping Sciences
Co-published by ASPRS, ACSM and ASCE
ISBN: 1-57083-011-8
563 pp · Paperback · 1994 · Stock #5021
List Price: $50 | **ASPRS Members:** $35
Student Members: $25 | **Amazon Price*:** $50

Hyperspectral Remote Sensing for Forestry
Paul Treitz, Valerie Thomas, Pablo J. Zarco-Tejada, Peng Gong, and Paul J. Curran
ISBN: 1-57083-093-2
107 pp · Softcover · 2010 · Stock #4584
List Price: $26 | **ASPRS Members:** $21
Student Member: $21 | **Amazon Price*:** $26

Manual of Geographic Information Systems
Editor: Marguerite Madden, PhD
Foreword: Jack Dangermond, Esri
ISBN: 1-57083-086-X · Hardcover · 1352 pages + DVD · July 2009 · Stock #4650
List Price: $53 | **ASPRS Members:** $40
Student Members: $40
Amazon Price*: $55

Meeting Environmental Challenges with Remote Sensing Imagery
Editors: Rebecca Dodge & Russ Congalton
Published by American Geosciences Institute; Publishing Partners: AmericaView, USGS Land Remote Sensing Program, ASPRS
ISBN: 978-0-922152-94-0 · 82 pp · Softcover · 2013 · Stock #4589
List Price: $7.50 | **ASPRS Members:** $6
Bulk Orders (3 or more copies): $4.50 each
Amazon Price*: $9.95

MANUAL OF REMOTE SENSING, 3RD EDITION (A SERIES)

Earth Observing Platforms & Sensors
Volume 1.1
Volume Editor: Mark Jackson
ISBN: 1-57083-089-4
550 pp · Hardcover · 2009 · Stock #4582
List Price: $95 | **ASPRS Members:** $75
Student Members: $55 | **Amazon Price*:** $95

Remote Sensing of Human Settlements
Volume 5
Editor-in-Chief: Andrew B. Rencz
Volume Editors: Merrill K. Ridd & James D. Hipple
ISBN: 1-57083-077-0
747+ pp · Hardcover · 2005 · Stock # 4576
List Price: $99 | **ASPRS Members:** $80
Student Members: $60
Amazon Price*: $69.99

Remote Sensing of the Marine Environment
Volume 6
Editor-in-Chief: Andrew B. Rencz
Volume Editor: James F.R. Gower
ISBN: 1-57083-080-0 · 360 pp · Hardcover · 2006 · Stock # 4578
List Price: $95 | **ASPRS Members:** $75
Student Members: $50 | **Amazon Price*:** $95

*Member discounts are not available when ordering directly from Amazon.

**Member discounts are not available on Amazon Kindle e-books,

†Students must order via the ASPRS Bookstore & a copy of your valid student ID must be submitted to be eligible for student pricing.

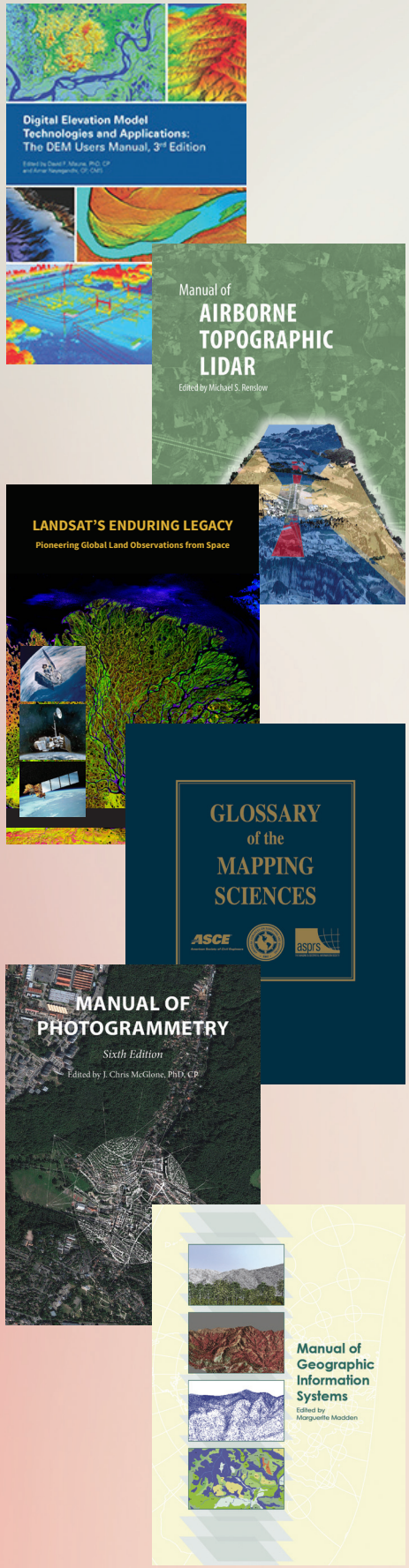

Landsat's Enduring Legacy

Pioneering Global Land Observations from Space

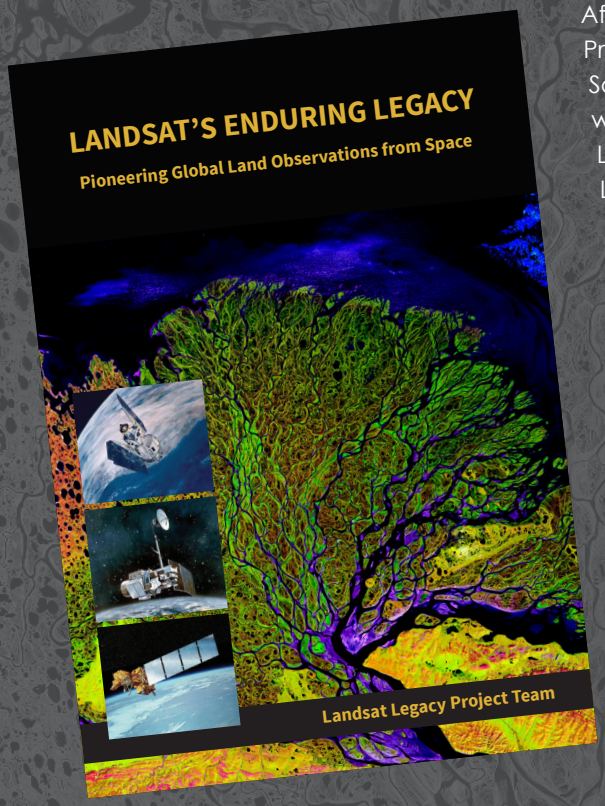

After more than 15 years of research and writing, the Landsat Legacy Project Team is about to publish, in collaboration with the American Society for Photogrammetry and Remote Sensing (ASPRS), a seminal work on the nearly half-century of monitoring the Earth's lands with Landsat. Born of technologies that evolved from the Second World War, Landsat not only pioneered global land monitoring but in the process drove innovation in digital imaging technologies and encouraged development of global imagery archives. Access to this imagery led to early breakthroughs in natural resources assessments, particularly for agriculture, forestry, and geology. The technical Landsat remote sensing revolution was not simple or straightforward. Early conflicts between civilian and defense satellite remote sensing users gave way to disagreements over whether the Landsat system should be a public service or a private enterprise. The failed attempts to privatize Landsat nearly led to its demise. Only the combined engagement of civilian and defense organizations ultimately saved this pioneer satellite land monitoring program. With the emergence of 21st century Earth system science research, the full value of the Landsat concept and its continuous 45-year global archive has been recognized and embraced. Discussion of Landsat's future continues but its heritage will not be forgotten.

The pioneering satellite system's vital history is captured in this notable volume on Landsat's Enduring Legacy.

Landsat Legacy Project Team

Samuel N. Goward
Darrel L. Williams
Terry Arvidson
Laura E. P. Rocchio
James R. Irons
Carol A. Russell
Shaida S. Johnston

Landsat's Enduring Legacy

Hardback. 2017, ISBN 1-57083-101-7

Student	$60*
Member	$80*
Non-member	$100*

* Plus shipping

Order online at

www.asprs.org/landsat

asprs THE IMAGING & GEOSPATIAL INFORMATION SOCIETY